Development of Mechanochemically Active Polymers

for

Early Damage Detection

by

Jin Zou

A Dissertation Presented in Partial Fulfillment
of the Requirements for the Degree
Doctor of Philosophy

Approved November 2014 by the
Graduate Supervisory Committee:

Lenore L. Dai, Co-Chair
Aditi Chattopadhyay, Co-Chair
Mary Laura Lind
Bin Mu
Hongyu Yu

ARIZONA STATE UNIVERSITY

December 2014

ABSTRACT

Identification of early damage in polymer composite materials is of significant importance so that preventative measures can be taken before the materials reach catastrophic failure. Scientists have been developing damage detection technologies over many years and recently, mechanophore-based polymers, in which mechanical energy is translated to activate a chemical transformation, have received increasing attention. More specifically, the damage can be made detectable by mechanochromic polymers, which provide a visible color change upon the scission of covalent bonds under stress. This dissertation focuses on the study of a novel self-sensing framework for identifying early and in-situ damage by employing unique stress-sensing mechanophores. Two types of mechanophores, cyclobutane and cyclooctane, were utilized, and the former formed from cinnamoyl moeities and the latter formed from anthracene upon photodimerization. The effects on the thermal and mechanical properties with the addition of the cyclobutane-based polymers into epoxy matrices were investigated. The emergence of cracks was detected by fluorescent signals at a strain level right after the yield point of the polymer blends, and the fluorescence intensified with the accumulation of strain. Similar to the mechanism of fluorescence emission from the cleavage of cyclobutane, the cyclooctane moiety generated fluorescent emission with a higher quantum yield upon cleavage. The experimental results also demonstrated the success of employing the cyclooctane type mechanophore as a potential force sensor, as the fluorescence intensification was correlated with the strain increase.

ACKNOWLEDGMENTS

At the end of this journey of pursuing my PhD, I have the pleasure to look back and express my deepest gratitude to all the people who have supported me and contributed in various ways in making the journey unforgettable in my life. First and foremost, I owe my deepest gratitude to my advisor Professor Lenore L. Dai. My PhD journey would not have been possible without her guidance, support and encouragement. She always gives me constant guidelines and support on the research, bears my mistakes and instructs me frequently with patience. Furthermore, she teaches me countless things, not only in the academic research, but also in the attitudes towards life. I always feel fortunate to work in Professor Dai's group. I am also extremely indebted to my co-advisor Professor Aditi Chattopadhyay for her kindness and providing necessary resources to accomplish my research work. In addition, I am grateful to the members of my thesis committee, Professor Mary L. Lind, Professor Bin Mu, and Professor Hongyu Yu for their encouragement and insightful suggestions about my research.

It is my pleasure to acknowledge my past and present group colleagues, Dr. Huan Ma, Dr. Yanmei Song, and Dr. Sriya Sanyal for training of instruments, Dr. Denzil Frost for collaboration on the ionic liquid gelation publication, Mingmeng Zhang, Haobo Chen and Prithwish Chatterjee for their tremendous help in the lab, Elizebeth Nofen for her hard work and dedications on the Air Force project, Bohan Shan for his assistance on DSC and DMA experiments. I am also pleased to work with the two newest PhD members, Stella Nickerson and Wei Gao. Many thanks go in particular to several collaborators from Professor Aditi Chattopadhyay's group, Dr. Yingtao Liu, Jinjun

Zhang and Bonsung Koo for effective and enjoyable collaboration on the Air Force project.

I also would like to thank the friends whom I have met at Arizona State University for their encouragement. Furthermore, I tremendously appreciate the support from my husband and my parents. They are always there to support and motivate me during my difficult moments to overcome through frustration.

Finally, I take this opportunity to sincerely acknowledge the Air Force Office of Scientific Research Office (AFOSR), grant number FA9550-12-1-0331 and the Program Director Dr. David Stargel for the generous financial support.

TABLE OF CONTENTS

Page

LIST OF TABLES vi

LIST OF FIGURES vii

CHAPTER

1 INTRODUCTION……...…..1

2 BACKGROUND AND MOTIVATION……..……..4

2.1 “Smart” Materials 4

2.1.1 Temperature Responsive Polymers 4

2.1.2 pH Responsive Polymers 7

2.1.3 Other Stimuli Responsive Polymers 8

2.2 Mechanically Responsive Polymeric Materials 10

2.3 Motivation of This Work……...23

3 METHODOLOGY…..……..…..38

3.1 Preparation of Cyclobutane-based Polymers……....36

3.1.1 Materials 36

3.1.2 Synthesis and Sample Preparation 36

3.1.3 Characterization 39

3.1.4 Molecular Dynamics Simulation 47

3.2 Preparation of Cyclooctane-Based Polymers 48

3.2.1 Materials 48

3.2.2 Synthesis and Sample Preparation 48

CHAPTER Page

3.2.3 Characterization 50

4 RESULTS AND DISCUSSION……..…….52

4.1 Cyclobutane-Based Polymers and Composites 52

4.1.1 Synthesis and Reaction Mechanisms 52

4.1.2 Glass Transition Temperature and Cross-link Density Analysis..... 68

4.1.3 Fluorescence Response by Mechanically Activation..... 96

4.2 Cyclooctane-Based Polymers 107

4.2.1 Synthesis and Reaction Mechanisms 107

4.2.2 Fluorescence Responses by Mechanical Activation 112

5 SUMMARY AND FUTURE DIRECTIONS……..…….……..115

5.1 SUMMARY 115

5.2 FUTURE DIRECTIONS.....116

REFERENCES……..124

APPENDIX

A EFFECTS OF GELATOR 12-HYDROXYSTEARIC ACID (12-HSA) ON IONIC LIQUID BASED PICKERING EMULSIONS……140

LIST OF TABLES

Table Page

4. 1 NMR Data of TCE. 57

4. 2 Kinetic Parameters of the Photoreactive Molecules. 68

4. 3 T_g of Polymer Blends with Various Contents of Cross-Linked TCE or PVCi Polymers. 75

4. 4 Comparison of T_g of Samples Cured at Different Temperatures. 78

4. 5 Comparison of T_g Determined by DSC and DMA 89

4. 6 Young's Modulus for Neat Epoxy and Polymer Blends 94

LIST OF FIGURES

Figure Page

2. 1 Representation of the Potential Energy of a Reaction in the Absence of a Coupled Force (Blue) and in the Presence of a Coupled Force (Red)[95]..... 13

2. 2 MD Simulations Show Strain Energy Distribution in a Tightening Polyethylene Knot, which Experienced More Stress at the Entrance and Exit of a Knot[110]. 16

2. 3 a) Simulation of Truncated Model of Spiropyran Showing the Pulling Directions (Mechanophore Model, Red Arrows; Control Model, Blue Arrows); b) Steered Molecular Dynamics for the Truncated Mechanophore and Control[98]. 17

2. 4 Diagrams Illustrating the Various Types of Elongation Flow. The Direction of the Flow is Shown by the Arrows. a) Opposite Jet Flow Cell, with the Stagnation Point in the Center, Marked with an X. b) Constriction Flow Cell[117]. 19

2. 5 Mechanism for Polymer Chain Scission in Response to Acoustic Cavitation: Solvent Bubble Nucleation Growth and Collapse Occurs Overtime under Sonication[122]..... 20

2. 6 Ultrasonically Induced Cycloreversion of a Polymer Embedded with Perfluorocyclobutanes[132]..... 21

2. 7 Summary of Experimental Methods for Characterization of Mechanochemical Changes over a Range of Strain Rates and Size Scales, in Solution and Solid Polymers[96]. 22

2. 8 (top) Mechanically Induced Decomposition of a Polymeric Bis(adamantyl) dioxetane to Keto-Intermediates Resulting in Blue Ehemiluminescence. (Bottom) Optical Images Obtained during Stretching of the Polymeric Film with Various Acceptor 27

Figure Page

2. 9 (a) Cartoon Illustration of Poly(methyl acrylate) with Embedded Spiropyran-Based Mechanophores Structure and Stress Induced Reaction; (b) Optical Progressive Images of an Actual Dog-Bone Sample of a Mechanophore-Linked Elastomer during Tensile Loading[98]..... 28

2. 10 (a) The Location of Mechanophore Units in Thermoplastics; (b,c) Cross-Linked Polymers. The Mechanophore is Colored in Red. 31

2. 11 Schematic Approach by Blending the Mechanophore-Linked Polymer to Composite Matrix Applied as Stress-Sensitive Material which can Response to Force by Color Change. 31

2. 12 Depiction of the Blending Approach to Create a Stress-Sensitive Material. (Top) before Crack Formation; (Bottom) after Crack Formation. 33

2. 13 Depiction of the Mechanism of the Cyclooctane Applied as a Crack Sensor. 35

3. 1 Schematic Illustration of Preparation of GFRC Sheet……..……39

3. 2 Cubic Epoxy Sample Loaded on MTS Servo Hydraulic Test System For Compression Test. 43

3. 3 (Left) GFRC Sheet Loaded on the Test Machine TestResource 800L; (Right) GFRC Sheet with a Hole in the Center before Loaded. 46

3. 4 Cyclic Loading Parameter in Tensile Fatigue Test. 46

3. 5 Schematic of Smart Polymer Unit Cell. 47

4. 1 Synthesis of TCE in the Presence of DMAP……..……53

4. 2 (a) ^{1}H NMR and (b) ^{13}C NMR Spectra of TCE Dissolved in $CDCl_3$. 55

Mass Spectra for TCE and the Main Chemical Structures. 58

Figure Page

Mass Spectra for TCE and the Main Chemical Structures. 58

4. 4 Trans-Cis Photoisomerization of the Cinnamate Monomer. 59

4. 5 Dimerization Mechanism of the Cinnamate Monomer. 59

4. 6 The Change of UV Absorbance of TCE Solution as a Function of the UV Exposure Time. 61

4. 7 IR Spectra of TCE Film on a KBr Disk before and after Photoirradiation. 62

4. 8 Schematic Illustrations of Three-Dimensional Networks of TCE (top) and Cross-Linked Polymers of PVCi (bottom). Active Sites are in Red. 63

4. 9 Chemical structure of PVCi. 63

4. 10 The Change of UV Absorbance of TCE Solution as a Function of the UV Exposure Time. 64

4. 11 IR Spectra of TCE Film on a KBr Disk before and after Photoirradiation. 65

4. 12 The Change in the Conversion of (top) TCE and (bottom) PVCi as a Function of the UV Exposure Time. 66

4. 13 Comparisons of Conversion Rates between the Experimental and Theoretical as a Function of the Conversion of the Photoreactive Molecule: (top) TCE and (bottom) PVCi. 67

4. 14 Chemical Structure of Epoxy Resin (top) and Hardener (bottom) 70

4. 15 Epoxy Curing Mechanism[176]. 70

4. 16 Cured Epoxy Network[176]. 70

4. 17 Schematic Illustration of Preparation of Polymer Blends. 71

4. 18 DSC Curves for the (top) TCE Cross-Linked Polymer; (middle) PVCi Cross-Linked

Polymer; (bottom) Neat Epoxy and Epoxy/Polymer Blends. 73

4. 19 SEM Micrographs of (a) Neat Epoxy (b) Epoxy with 10 wt. % TCE Polymer (c) Epoxy with 10 wt.% PVCi Polymer. 74

4. 20 T_g of Epoxy with Various Contents of Cross-Linked TCE (Top) and PVCi (Bottom) Polymer between Theoretical Value and Experimental Data. 76

4. 21 DSC Curves for the Samples Cured at 60 ℃. 78

4. 22 Schematic of Molecular Structure before and after Covalent Bond Generation; Grey, Cyan, Blue and Red Sphere Represent Hydrogen, Carbon, Oxygen, and Nitrogen, Respectively. It Shows That Nitrogen Make Two Covalent Bonds with Two DGEBFs. . 80

4. 23 Schematic Illustration of Active Sites and Cross-Linking Degree. 81

4. 24 Most Likely Cross-Linking Degrees of Neat Epoxy (a) and Smart Polymer (b); Red Solid Lines are Fitted Normal Distributions. 81

4. 25 T_g of Cross-Linked Epoxy Estimated by Relation of Density and Temperature during Simulation (Smart Polymer Represented Epoxy w/ 10 wt. % TCE Polymer). 83

4. 26 Correlation between T_g and Cross-linking Degree Conducted from MD Simulation. 85

4. 27 DMA Curve for the Specimens of Neat Epoxy and Polymer Blends. 87

4. 28 Cross-Link Density for Neat Epoxy and Polymer Blends. 89

4. 29 TGA and DTG Curves of Cross-Linked TCE (Top) and PVCi (Bottom) Polymer. 91

4. 30 TGA (Top) and the DTG (Bottom) of the neat epoxy and polymer blends. 92

4. 31 Compressive Stress-Strain Curves for the Pure Epoxy and Epoxy w/ 10 wt.% Cross-Linked TCE and PVCi Polymers Dispersed in the Matrix..... 94

Figure Page

4. 31 Compressive Stress-Strain Curves for the Pure Epoxy and Epoxy w/ 10 wt.% Cross-Linked TCE and PVCi Polymers Dispersed in the Matrix..... 94

4. 32 Correlation between Young's Modulus and Cross-Linking Degree (%) Conducted by MD Simulation..... 95

4. 33 Microscopic Images of Cracks Generated by Hammer Hit on (a) a Clean Polystyrene Substrate, a Polystyrene Substrate Coated with Cross-Linked (b)TCE and (c) PVCi Polymer under a UV Light. The Insets were the Corresponding Images under a White Light. 97

4. 34 Microscopic Images of Fluorescence Emission along Cracks Generated by Hammer Hit on Polymer Blends (a) without (b) with 10 wt.% (c) 30 wt. % (d) 50 wt.% Cross-Linked TCE Polymer. The Insets were the Corresponding Images under White Light. 99

4. 35 Microscopic Images of Fluorescence Emission in Response to Different Strains of Epoxy w/ 10 wt.% Cross-Linked TCE (Top) and PVCi (Bottom) Polymer Blends..... 100

4. 36 Integrated Density of Fluorescence Emission in Response to Different Strains of Epoxy w/ 10 wt. % Cross-Linked TCE (Top) and PVCi (Bottom) Polymer Blends..... 101

4. 37 (Left) Fluorescence Density of Fiberglass Epoxy Composite with 10% TCE before and after Damage was Applied. (Right) GFRC Specimen under White Light. 103

4. 38 SEM Micrographs of Glass Fiber Reinforced Epoxy Composite with 10% TCE at Different Fatigue Cycle Stages. Insets are the Images under White Light. 105

4. 39 Microscopic Images of Fluorescence Emission on GFRC in Response to Different Fatigue Cycle Stages. 106

Figure Page

4. 39 Microscopic Images of Fluorescence Emission on GFRC in Response to Different Fatigue Cycle Stages. 106

4. 40 Corresponding Fluorescence Density of Glass Epoxy Composite with 10% TCE at Different Fatigue Cycle Stages. 106

4. 41 Synthesis Route for Poly-AC.(Top) Dimerization of Anthracene; (Bottom) Fischer Esterification under the Catalyst of p-TSA. 109

4. 42 Mechanism for p-TSA Catalyzed Fischer Esterification between Acids and Alcohols. 109

4. 43 The Change of UV Absorbance of Anthrance Solution as a Function of the UV Exposure Time. 111

4. 44 IR Spectra of a Mixture of Reactants before Reaction and after Reaction. 112

4.45 Enhanced Fluorescent Intensity Generation from Cracked Poly-Anthracene Compared to Cracked Poly-TCE. 113

4. 46 Tensile Test of Poly-AC Film. Inset is the Test Conducted on the Texture Analyzer Machine (TA.XT Plus Texture Analyzer). 113

4. 47 Corresponding Integrated Fluorescent Density of Poly-AC in Tensile Test with Corresponding Images. 114

5. 1 Schematic Illustration of Moving from the Blending System to the Proposed Integrated System. The Epoxy Network is presented in Red and the Mechanophores are presented in Green……...117

5. 2 Synthesis Routes for Incorporation of Cinnamoyl Mechanophore Functional Groups. Route 1: Incorporation into Epoxy Hardener for Use with Unmodified Resin. Route 2:

Figure Page

Incorporation into Both Epoxy Hardener and Resin.....119

5. 3 UV Activated Epoxy Curing of Mechanophore-Functionalized Resin and Hardener Units, in Blue and Red, Respectively..... 120

5. 4 Three Primary Approaches for Self-Healing. 121

5. 5 Reversible Photodimerization and Photocleavage under UV Light Irradiation for (Top) Cinnamoyl and (Bottom) Anthracene. 123

CHAPTER 1
INTRODUCTION

Environmentally responsive materials, often referred to as "smart" materials, have the ability to change their properties in response to external physical or chemical stimuli. "Smart" materials that are responsive to temperature and pH have been well-studied and are widely used in a variety of applications [1, 2]. However, there are limited materials that respond to stress, even though all materials deform under external stress and eventually exhibit fracture and failure. Mechanochemistry, in which a chemical reaction is induced by the input of mechanical energy, has received increasing interest in recent years and promote the application of "smart" stress-sensitive materials [3, 4].

Identification of early damage in polymer composites is of great importance. Damage and cracking within materials can result in poor performance, shortened lifetime, and even catastrophic failure. If the initiation of cracks can be easily detected, the cracked part can be healed or replaced before a complete destruction. Thus, stress-sensitive materials are anticipated to have tremendous applications in structural materials to extend their service life and reinforce their safety significantly. This thesis focuses on the development of mechanochemically active polymers (mechanophore-based polymers) for identifying localized damage precursors in polymer composites.

Chapter 2 is divided into two sections which provide the background information and the motivation of this study. The first section reviews "smart" materials, including pH-sensitive and temperature-sensitive materials with more focus on stress-

sensitive materials. The second section addresses the motivations and objectives of this study.

Chapter 3 describes the experimental methods for the synthesis of 1,1,1-tris(cinnamoyloxymethyl) ethane (TCE), the photo dimerization of TCE and poly vinyl cinnamate (PVCi), the preparation of the polymer blends specimen (epoxy with cross-linked TCE and PVCi polymers, the fabrication of glass fiber reinforced composite (GFRC) sheets, and the synthesis of poly-anthracene. The characterization of physical properties using a variety of techniques is also summarized in Chapter 3. Chapter 4 focuses on the experimental results and discussion. It started with the confirmation of synthesized chemicals by NMR and mass spectroscopy. The ultraviolet–visible spectroscopy (UV-Vis) and Fourier transform infrared spectroscopy (FTIR) experiments confirmed the cyclobutane formation of TCE and PVCi upon photoirradiation. The effect of the addition of the cyclobutane-based polymer (cross-linked TCE or PVCi polymer) on the thermal and mechanical properties of epoxy systems was then studied by differential scanning calorimetry (DSC), dynamic mechanical analyzer (DMA), and Instron. The glass transition temperature for neat epoxy was much higher than the two polymer blends. From the compressive stress-strain curves, the polymer blends showed lowered yield points. The thermal and mechanical properties were also used to validate molecular dynamics (MD) simulations and reasonable agreement was achieved. More importantly, the addition of cyclobutane-based polymers into a polymeric matrix demonstrated the capability to identify damage through stress induced fluorescent emission. The emergence of cracks was detected by fluorescence at a strain level right after the yield point of the polymer blends and the fluorescence intensified with accumulation of strain.

Further, we applied the TCE polymers to the systems level by preparing GFRC specimen. The fatigue tensile test was performed and then the crack initiation and propagation was observed by the induced fluorescence under the microscope. It is demonstrated that besides cyclobutane-based polymers, cyclooctane-based polymers was also successfully used to detect in-situ damage by the observation of fluorescent generation. Chapter 5 provides a summary of this study and proposes future directions of the work. The future work includes direct incorporation of mechanophores into a thermoset polymer network and self-healing of mechanophores for strength recovery. This dissertation ends with the sections of Reference and Appendix.

CHAPTER 2
BACKGROUND AND MOTIVATION

2.1 “Smart” Materials

The dynamic nature of biological systems makes them incredible in their ability to sense and adapt to changing environments. For example, sunflowers can track the sun’s path across the sky, turning towards sun slowly and our skin can repair and regenerate itself after being damaged. However, common synthetic structural materials are limited in their ability to sense changes under external stimuli or repair themselves. Inspired by biological systems, many efforts are being deployed to design “smart” materials which can self-sense in response to external stimuli due to their great potential for application in both science and technology [1, 5-8]. Typical stimuli studied are temperature, pH, light, electric field and magnetic field. Some “smart” materials are available commercially [9, 10].

2.1.1 Temperature Responsive Polymers

Temperature is the most widely used stimulus in environmentally responsive polymer systems because it is easily controlled and applicable [11-14]. One of the unique properties of temperature-responsive polymers is the presence of a critical solution temperature, which is the temperature at which the phase behavior of polymer and solution undergo abrupt changes in solubility according to their composition [15, 16]. If the polymer and solution are completely miscible below a specific temperature, and immiscible above this temperature, that temperature point is a lower critical solution temperature (LCST) [17, 18]. In the opposite condition, it is called an upper critical solution temperature (UCST) [17]. There are many applications for LCST based

polymers in the biomedical fields [11, 19-22]. The polymer transforms from the extended coil state to a compact globule state immediately at its LCST. This smart transition behavior is related to the hydrogen-bonding capabilities which are controlled by a fine hydrophobic-hydrophilic balance in the structure [13]. When the temperature is above the LCST, the hydrophobic interactions dominate, making polymer chains aggregate. Conversely, when the temperature is below the LCST, the polymer chains are hydrated and swollen. The temperature-responsive material poly(N-isopropylacrylamide) (PNIPAAm) is the most studied because LCST of PNIPAAm in an aqueous solution is 32 ℃ which is very close to physiological condition of human body [1, 23]. Polymer chains can be prepared with a combination of functional groups that respond to pH, temperature, ionic strength, UV irradiation, magnetic fields and electric fields, producing multifunctional materials [17]. Fu et al. prepared magnetic thermoresponsive polymeric microspheres based on PNIPAAm. These dual-responsive polymeric microspheres can responde to magnetic field and temperature simultaneously, offering an attractive application in targeted drug delivery[24].

Besides PNIPAAm, poly(N, N'-diethylacrylamide) (PDEAAm) is another commonly used temperature responsive polymer, because it has a LCST ranging from 25 ℃ to 35 ℃ [1, 25]. Also, some biopolymers such as gelatin have been reported to exhibit temperature responsive behavior [20]. However, the physical properties of gelatins are not stable when applied in biomedical applications, making it necessary to introduce chemical cross-linking to improve their stability at physiological temperature [26].

Temperature-responsive polymers can be modified to increase their sensitivity by using a macro porous structure or phase-separated structures due to the increase of the surface area [1, 27-29]. This improvement has been used as biomimetic actuators. The combination of hydrophilic and hydrophobic groups with different ratios in polymer chain can adjust the LCST and therefore mimic biological entities with temperature switching [17]. For example, by variation in hydrophilic or hydrophobic co-monomer content, the LCST of PNIPAm can be tuned below or above 37 ℃ which is suitable for biomedical applications [20]. In general, a small ratio of hydrophilic monomers increases the LCST of temperature responsive polymer [30]. In contrast, a small ratio of hydrophobic constituent decreases the LCST [20, 30, 31]. However, some applications warrant the use of a polymer with a LCST above body temperature. For example, gene carrier systems are designed to have their LCST between body temperature and 42 ℃, because hyperthermic cancer treatments are generally performed in that range of temperature [1]. Because of these specific advantages, temperature-responsive polymers have also been extensively investigated to develop temperature-modulated "smart" membranes and in chromatography. For example, PNIPAAm-grafted porous membranes have shown positive control of solute through open gates at higher temperature, while a PNIPAAm-grafted nylon capsule shows negative control of solute diffusion by blocking the solute from passing through the surface of the membrane at temperatures above the LCST [32, 33]. Okano et al. reported that the use of PNIPAAm and its derivatives as surface modifiers for novel chromatography in which an aqueous mobile phase was utilized [6]. This technique effectively controlled the permeation and diffusion of the bioactive compounds and allowed them to be separated.

2.1.2 pH Responsive Polymers

pH responsive materials are also mainly used in biomedical applications, such as in drug delivery systems or gene carriers [34-36]. In the human body, remarkable variations in pH are naturally observed on different tissues and organisms, which provide pH-sensitive material an opportunity for specific delivery of therapeutic agents in an effective and reliable way. pH-sensitive polymers are polyelectrolytes that have weak acidic or weak basic groups in their structure to accept or release protons in response to pH changes in the surrounding environment [1]. Carboxyl and pyridine moeties are the most commonly used side groups in pH-responsive materials [17]. Carboxyl groups, under acidic environmental conditions, are protonated and hydrophobic interactions dominate, leading to shrinkage of the polymer. At high pH values, carboxyl groups dissociate into carboxylate ions, resulting in a high charge density in the polymer. The electrostatic repulsion of generated charges causes the polymer to swell dramatically. In general, this reversible swelling–shrinking behavior is caused by the transformation between the ionized form and the deionized form. It is well known that polyacrylic acid (PAAc) and polymethacrylic acid (PMAA) are the most common pH responsive polyacids, bearing carboxylic pendant groups [37, 38]. PAAc has a relatively continuous phase transition, while PMAAc shows an abrupt transition because of the stronger hydrophobic interaction from the methyl groups [39]. Conversely, pyridine is an acid-swellable group [17].

The critical pH at which the reversible conformational changes of the polymer chains occur can be adjusted by choosing an ionizable moiety with a pKa matching the desired pH range, or incorporating a hydrophobic moiety into the polymer backbone [25,

40]. The swelling and collapsing behavior in response to pH change has been successfully used to induce controlled release of drugs [1]. Shchukin et al. prepared a novel capsules by applying inorganic particles as building blocks glued together by a pH-sensitive polyelectrolyte, demonstrating controlled release/uptake properties combined with mechanical strength [41].

In the application of polypeptides and proteins for the treatment of disease, pH responsive polymers have been applied to drug delivery systems as protecting agents to avoid the degradation of polypeptide drugs in the acidic environment of the stomach [42, 43]. Kim et al. has synthesized a PNIPAAm-based copolymer for the intestinal delivery of insulin by combining butylmethacrylate and acrylic acid to provide protection of various drugs from the acidic stomach and releasing drugs in the neutral intestine [44]. For a targeted drug delivery to the stomach, weak polybase hydrogels are used, because polybase hydrogels are protonated and swollen at acidic condition to release drugs [45-48].

2.1.3 Other Stimuli Responsive Polymers

The temperature and pH responsive mechanisms have been greatly investigated and widely used in many applications. Other stimuli responsive polymers have also been studied as well. Light-sensitive hydrogels can undergo reversible photomechanical changes [49]. Visible light-sensitive hydrogels bearing copper chlorophyll bound to PNIPAAm will contract in the presence of visible light and swell when the light source is removed [50]. This property can be used in photo responsive artificial muscles, photo-switches, and photo-memory devices [50]. Photo responsive polymer can also be used in

microcapsule shells allowing remote control of the drug release by light [51]. Electric or magnetic field responsive polymers can also swell or shrink in response to an external field, and have been applied as drug delivery systems or biomimetic actuators [52-55].

Magneto-responsive materials consist of magnetic nanoparticles embedded within a polymeric matrix [56, 57]. The magnetic particles can be aligned in the presence of an externally applied magnetic field, influencing the mechanical properties of these materials. Polymer fluids composed of magnetic nanoparticles are becoming increasingly important for applications in catalysis, separation sciences, and biosciences [56, 57]. Farshad et al. discovered that in a compression test, the compression modulus or stresses of their magneto-responsive polymer composite were higher in the presence of the magnetic field compared with those in the absence of the magnetic field [58]. These new class of composite materials have already been applied in the field of sensing, magnetic separation, catalysis and magnetic drug delivery [56, 59-62].

Glucose responsive polymer systems have also gained much attention recently, especially in the controlled delivery of insulin due to a huge biomedical market potential in the treatment for diabetic patients [63-66]. When the concentration of glucose in the blood becomes high, the glucose responsive hydrogel system can provide a self-regulating release of insulin in order to keep the blood glucose levels within a normal range.

Given that mechanical loading is inevitable in everyday applications, “smart” stress-sensitive materials, such as a force sensor, become an attractive class of self-sensing materials due to their potential applications. Detecting the response to mechanical

stress applied on various materials is useful for predicting their behavior and determining their performance in specific applications. However, there are limited "smart" materials that are responsive to stress, even though all materials deform under external stress and eventually exhibit fracture and failure. Piezoelectric materials are materials that produce an electric field in response to an application of mechanical force; and conversely, an applied electric field will produce a mechanical stress, leading to a change in dimension [62, 67]. During the last several decades, the development of piezoelectric materials has brought about a huge market of products used as actuators as well as sensors [68-70]. Piezoelectric stack actuators, for instance, typically generate large forces up to several kN with only a displacement of microns. An everyday life example would be the airbag sensors in automobiles in which the mechanical stress caused by crash generates the electricity necessary to trigger the airbag inflation. Hess et al. reported the success of developing stress-responsive polymer nanocomposites which were comprised of a cellulose nanofiber network embedded in a polyvinyl acetate matrix [71]. This nanocomposite material displayed reversible and switchable stiffness with a significant decrease in Young's modulus when it transitioned from dry to wet.

2.2 Mechanically Responsive Polymeric Materials

A mechanochemically active polymer, as the name implies, is a polymer which can exhibit a chemical response to a mechanical force. It is a typical type of stress-sensitive material that has been developed at the intersection of mechanics and chemistry. The chemistry can be subdivided according to what type of energy is input to initiate and stimulate chemical reaction system [72]. Thermal energy is a relatively straightforward energy source. The application of heat is concentrated in the bonds involved and provides

the molecules sufficient kinetic energy to pass through an energy barrier separating the desired products from their starting materials. Photons, in the form of electromagnetic radiation, deliver energy to target atoms or molecules and bring the atoms or molecules to the necessary activation energy with the absorption of light. Similar to photons, electrons can also deliver energy. In this case, the chemical reaction is driven by the passage of an electric current. Correspondingly, regarding the activation type of the chemical reactions above, chemists can classify the chemistry in terms of thermochemistry, photochemistry and electrochemistry [72].

The term "mechanochemistry," introduced as one sub-discipline of chemistry by Wilhelm Ostwald at the end of 19th century, is arguably the least well understood of the disciplines [73]. As the name itself implies, mechanochemistry involves mechanical work as the activation energy to modulate chemical transformation. This process differs from conventional forms of energy input such as heat or light for chemical reaction. In the history of mankind, the ancient people already started to make advantage of mechanical work on the course of chemical reactions. The utilization of friction for making fire is a well-known example, which is the most commonly used primitive method and still frequently used in human activity today. Even though the effect of mechanical action on chemical reactions has been observed and utilized since prehistorical times, the understanding of mechanochemical transformation is still not complete.

It is only in the last several decades that mechanochemistry was developed into an exact science. More fundamental concepts of mechanochemistry and the effects of force on the molecules have been investigated. The field of applications ranges from medical

and personal care to semiconductors and batteries, some of which are already going into the production scale [74-77]. Chemical reactions that can be conducted by mechanical manipulation including grinding, ball milling, sonication, mastication or stretching where macroscopic force can be applied to small molecules [78-80]. The macroscopic mechanical force can be concentrated and accumulated on a certain area of a subject and finally result in the breakage of the bonds of that area at the molecular scale. The first written document involving a mechanochemical reaction was as early as 300 B.C. from Theophrastus of Ephesus, a student of Aristotle [73]. Metallic mercury was obtained by grinding cinnabar (HgS) with a brass mortar and pestle in the presence of vinegar [73]. For most traditional chemical reactions in both the laboratory and industry, even though they are successful, they are also wasteful, consuming a large amount of hazardous organic solvent or expensive catalyst needed to speed up the chemical reactions to make the products. To meet the large industry need, the increasing demand for solvents or catalysts has made our current conventional solution-based chemical batch process unsustainable with regard to a growing and costly energy demand for solvent production, catalyst recycling and product separation and purification. Mechanochemical reactions, on the other hand, can be solvent-free (or with minimal solvent) with the application of a green physical catalyst – mechanical force to initiate the reactions [75, 81-85]. Mechanochemistry, with its simple and environmentally friendly synthetic method, is rapidly becoming popular as a sustainable alternative to conventional chemical batch processes, because mechanical force can modify the rate, the outcome and a yield of chemical reactions [80-82]. A large number of experiments have been reported to demonstrate that mechanical force can promote these chemical reactions [86-88].

It is well known that H_2 is generated by the reaction between water molecules and the surface mechanoradicals created during wet grinding of ceramics [89, 90]. Kameda et al reported dry grinding treatment of kaolinite can generate H_2 between surface water molecules and mechanoradicals created by the rupture of Si–O or Al–O–Si bonds [91]. Streletskii et al. investigated the processes of methane and ethane formation in the mechanical treatment of Zr and Ni containing system in the presence of CO + H_2 or CO atmosphere and graphite [92, 93]. It was found that 100% of the hydride may be converted into methane in the mixture of hydrides with carbon [92]. In another example, coal can be activated by milling or grinding to generate the radicals to react with oxygen or water to basic or acidic groups, as reported by Turcaniova et al [94]. It is obvious that significant advances have been made in the field of mechanochemistry recently.

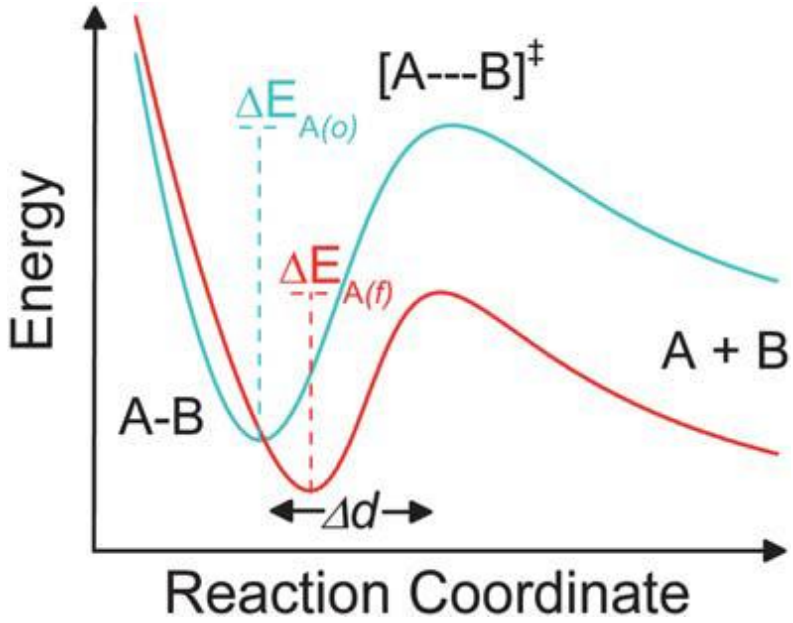

Figure 2. 1 Representation of the Potential Energy of a Reaction in the Absence of a Coupled Force (Blue) and in the Presence of a Coupled Force (Red)[95].

Mechanical work can also generate heat to induce thermochemical reactions. As temperature increases, molecules obtain energy to overcome activation energy. For a long time, mechanical induced chemical reactions were attributed to this "heat." However, mechanochemical processes are different form simple thermal processes. Experiments have proven that the reaction can still occur even if there is no temperature increase. The physical basis for mechanically induced changes in these reactions is related to the chemical and mechanical potential energy, as shown in Figure 2.1. When the bond is elongated under stress, the mechanical potential energy decreases with the increase on chemical potential energy, leading to activation energy reduction which can be expressed in the equation of $\Delta(\Delta E_{act}) = F \cdot \Delta d$, where F is the force and Δd is the geometry change along the force direction [95].

In the area of mechanochemistry, "smart" stress-sensitive polymeric materials currently focus on solution-based and solid-state polymeric materials which both employ mechanophores as the mechanoresponsive trigger [96]. Mechanophores are used for targeted cleavage or rearrangement of bonds. The term "mechanophore," which was first introduced by Moore et al., is a stress or strain activated molecular unit that is inserted into a polymeric material to provide a molecular-scale reading of the local mechanical state or to transform materials properties in response to the local mechanical environment [97].

When it comes to a single molecule, it is possible to break single bonds using the advanced techniques, which were originally designed to precisely measure the force of the bond. These techniques include atomic force microscopy (AFM), optical and

magnetic tweezers, biomembrane force probes, and glass needles [98, 99]. These tools can provide a force ranging from 0.01-1000 pN [100-102]. AFM is one of the most precise techniques for force control and has specifically been used to study single molecule mechanochemistry by attaching a macromolecule between a functionalized substrate and an AFM tip [98, 103, 104]. The force to retract the AFM tip is measured and increased to lift the molecule from the surface and stretch. The force gradually increases until chemical bond rupture occurs. The force at rupture point is measured as the force of the bond [105]. It is known that knotted macroscopic ropes break right at the knot and experiments have shown that knotted polymers behaved similarly [105, 106]. Aria et al. applied optical tweezers to tie individual DNA and actin filaments into a knot [106]. The actin filament was found to be broken at a force of 1 pN which was much smaller than the force on a straight filament. Efforts have been taken to study bond scission at the molecular level under stress in the field of computer simulation. Molecular dynamics (MD) simulations have been used to map the force distributions on polymer chains [106-108]. In the simulation of strain energy on a knotted polyethylene (Figure 2.2), it was shown that the strain energy mostly localized on the bonds at the end of the knot compared to the unknotted segments when the polymer was stretched out [109]. Saitta et al. also studied the influence of a knot on the strength of a polymer strand by conducting quantum molecular dynamics simulations and found that the polymer underwent a homolytic C-C bond cleavage at the entrance to the knot under tension [109].

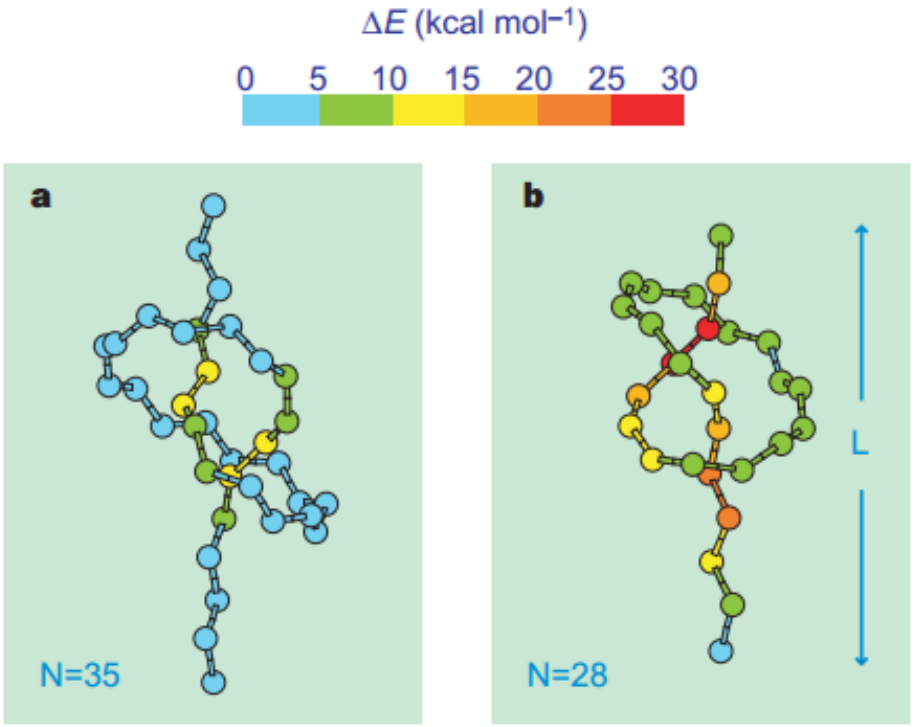

Figure 2. 2 MD Simulations Show Strain Energy Distribution in a Tightening Polyethylene Knot, which Experienced More Stress at the Entrance and Exit of a Knot[110].

In the constrained optimization approach, the molecular geometry can be optimized by modeling a distance constraint between two atoms under stress. Moore et al. applied first principles steered MD simulations and density functional theory to study the effect of an external force breaking a covalent bond on a known mechanophore model, specifically the molecule spiropyran, and the difunctional control model [97]. The C-O bond on spiropyran molecule was found to be the critical point in control of the induced color change. There were many possible links across the spiropyran junction that varied in transfer force, making it quite necessary to optimize the polymer attachment points on the mechanophore molecule. The results (Figure 2.3) were plotted as C–O bond distance versus time under different forces at 2, 2.5 and 3 nN. It was showing that scission

occurred at the C-O bond on mechanophore model, while no C-O bond rupture was observed on the difunctional control model during the indicated timescale which indicated this placement precluded the transfer of any substantial force into the spiropyran. Further study of relationship between the elongation and potential energy showed that bond rupture occurred at spiropyran C–O and N–H bonds for mechanophore model and control model, respectively. In the case of the extended models, the result also showed that spiropyran C–O bond rupture occurred only on the mechanophore model. The simulation analysis on truncated and extended models agreed with the experiment result and validated the use of dynamics simulations to explore and optimize the polymer linking through the mechanophore to transmit the force effectively [98].

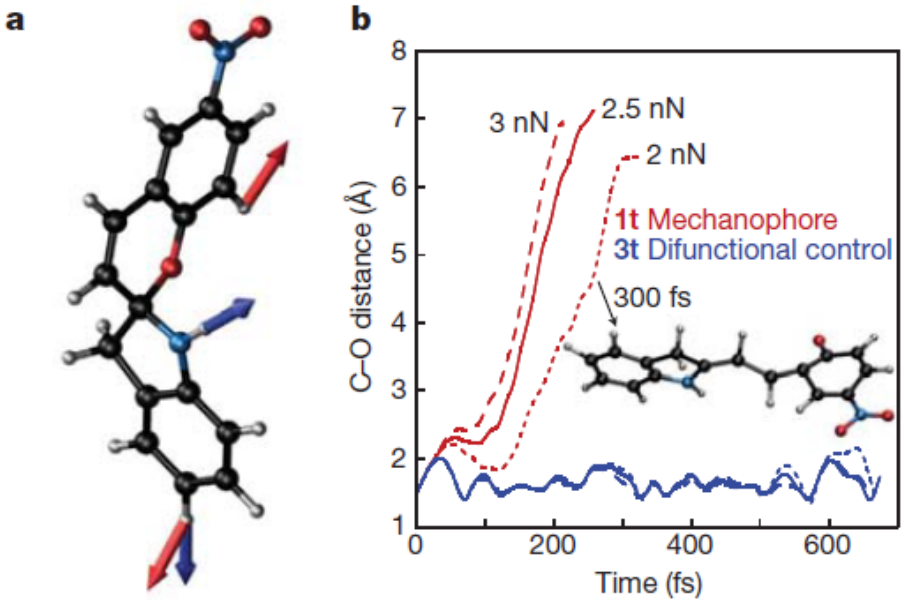

Figure 2. 3 a) Simulation of Truncated Model of Spiropyran Showing the Pulling Directions (Mechanophore Model, Red Arrows; Control Model, Blue Arrows); b) Steered Molecular Dynamics for the Truncated Mechanophore and Control[98].

For the polymer chains, the application of a mechanical force results in the bond cleavage being random. Less random cleavage showing a Gaussian distribution centered

on the middle of the polymer chains has been observed in dissolved polymer solutions where mechanical force applied through turbulent, elongational flow or sonication [110, 111]. The study of solution-based mechanoresponsive polymers was investigated firstly in flow fields by Staudinger et al. in 1930 [112]. Their initial investigation was to study the polymer degradation by examination of reduction in polymer molecular weight. Flow fields such as turbulent flow or elongation field apply strong hydrodynamic forces on solvated polymer chains, causing polymer extension in the direction of the flow field. Once the rate of chain stretching exceeds the rate of chain relaxation, the chain scission occurs ultimately. Turbulent flow was typically performed in single-gas pressure driven flow devices to generate shearing force to cause scission on polymer chain [113-115]. Turbulent flow is most effective on a dilute solution of polymer with high molecular weight in the range of 10^6 Da [113, 114]. Elongation fields are generated by two common methods: opposed jets and transient elongation, which are described in Figure 2.4 [116]**.** Opposed jets generate a region of zero velocity by two opposite jet flows to trap the flowing polymer, causing elongation on each end of the trapped polymer chain in opposite directions [117].

A simple constriction flow cell can also generate elongation force by the sudden decrease on the reactor volume near the entrance of the contraction [118]. This method is termed transient elongation, since it has no stagnant area. Activation under flow fields depends on the polymer molecular weight, solvent composition, polymer concentration, flow rate and so on [116, 119]. Since transient flow does not allow for the full extension of polymer chain, more random chain scission will occur. The partially extended polymer can form a distinct conformation, such as folded, kinked and dumbbell [120]. Polymers

with a high molecular weight enhance the chain scission. 10^5 Da in molecular weight is generally the limiting threshold for activation [121, 122].

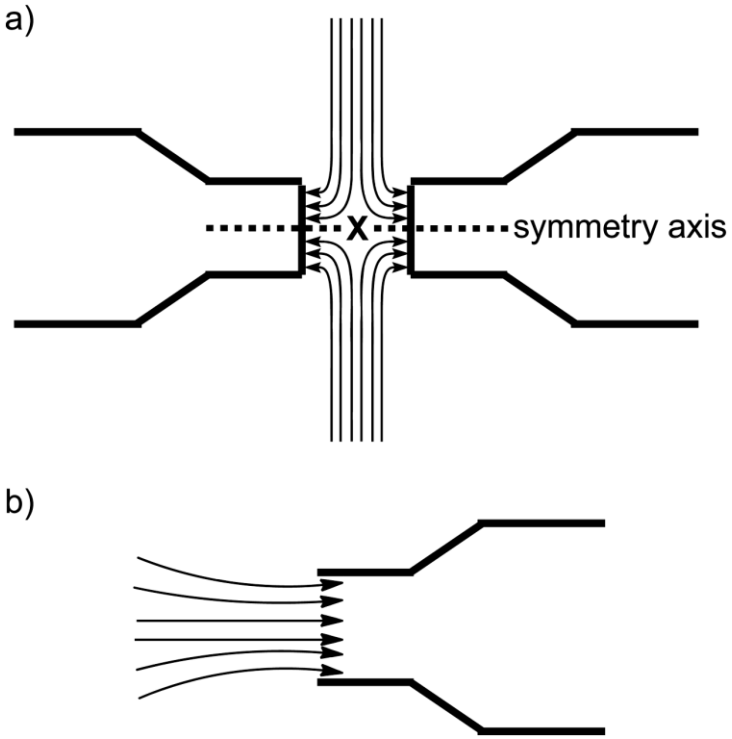

Figure 2. 4 Diagrams Illustrating the Various Types of Elongation Flow. The Direction of the Flow is Shown by the Arrows. a) Opposite Jet Flow Cell, with the Stagnation Point in the Center, Marked with an X. b) Constriction Flow Cell[117].

Ultrasound has proven to be an effective, simple method for applying mechanical force for the examination of well-defined polymers, because of its high strain rates and force generation [121, 122]. Different from flow fields, ultrasound generates mechanical force through solvodynamic shear, of which the mechanism is described in Figure 2.5 [121]. Formed solvent cavitation microbubbles induced by high frequency ultrasonic waves finally collapse violently and cause void space after experiencing rapid nucleation or growth. Solvent molecules and polymer chains in the vicinity of a collapsing bubble are then pulled into the void space. The polymer chain ends closer to the void space move

at higher velocities than the ones which are farther away, resulting in velocity gradients and stress along the polymer chain. Tensile forces created by nonequivalent force contributions at different polymer chain segments are finally cause the polymer to elongate and induce the activation. Besides the site-specific bond activation, the ultrasound technique can also facilitate some kinetically inaccessible cycloreversions and bond rotations with high efficiency, such as homolytic or heterolytic cleavage [123-126]. Like flow fields, polymer scission under ultrasound is also affected by various factors, such as ultrasonic frequency, solvent concentration and polymer concentration [121, 127-129].

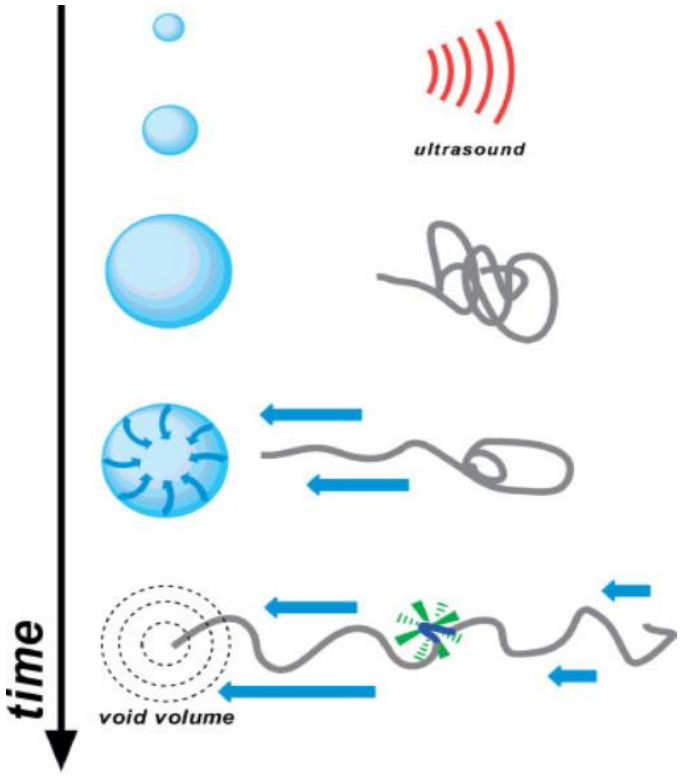

Figure 2. 5 Mechanism for Polymer Chain Scission in Response to Acoustic Cavitation: Solvent Bubble Nucleation Growth and Collapse Occurs Overtime under Sonication[122].

The mechanically facilitated electrocyclic ring opening reaction was firstly studied by Moore et al. [130] In their experiment, the trans and cis isomers of a 1,2-disubstituted benzocyclobutene underwent an ultrasound-induced electrocyclic ring opening and produced identical ortho-quinodimethides treated with 13C-labeled maleimides for characterization of sonochemical products. In force-induced cycloreversion reaction, Klukovich et al. reported mechanical activation of the perfluorocyclobutane-based mechanophores would result in a stepwise cycloreversion (Figure 2.6) [131]. In this polymer system, perfluorocyclobutane unit was repeated and dispersed throughout each polymer chain. The molecular weight was found to be reduced upon the sonication. More mechanically facilitated ring opening and cycloreversion using ultrasound have been reported in recent years [132, 133].

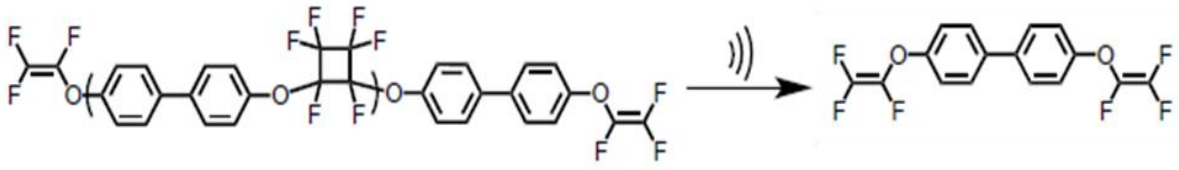

Figure 2. 6 Ultrasonically Induced Cycloreversion of a Polymer Embedded with Perfluorocyclobutanes[132].

Solution-based responsiveness demands the involvement of water, which makes it limited to certain practical applications. Many current efforts focus on the development of solid-state polymeric materials, as bulk materials have wide applications in the solid-state. Solid-state polymeric materials display a very wide range of mechanical responses, which depend on the chemical and physical structure of the polymer chains. At the macroscopic scale, the response of polymer to external force can be characterized by mechanical testing. When it comes to microscopic level, the response becomes more

complicated, which is related to polymer structure factors, including the degree of cross-linking and entanglements of polymer.

Force can be applied to polymers in the solid-state to induce selective chemical transformations at the atomic level through either elongation or compression [121]. Manually stretching the material is the simplest way to apply elongational forces to a polymer. Tensile testing devices and rheometers have also been used to study mechanically responsive materials. The instrument implementation is complicated compared to manually stretching, but they can precisely control and quantify the application of stress to materials. Conventional tensile testing devices stretch a dog bone shaped sample between two wedge grips [122]. Rheometers can be outfitted with an extensional fixture that uses two rotating drums, which allowed for the controlled elongation of a polymer film.

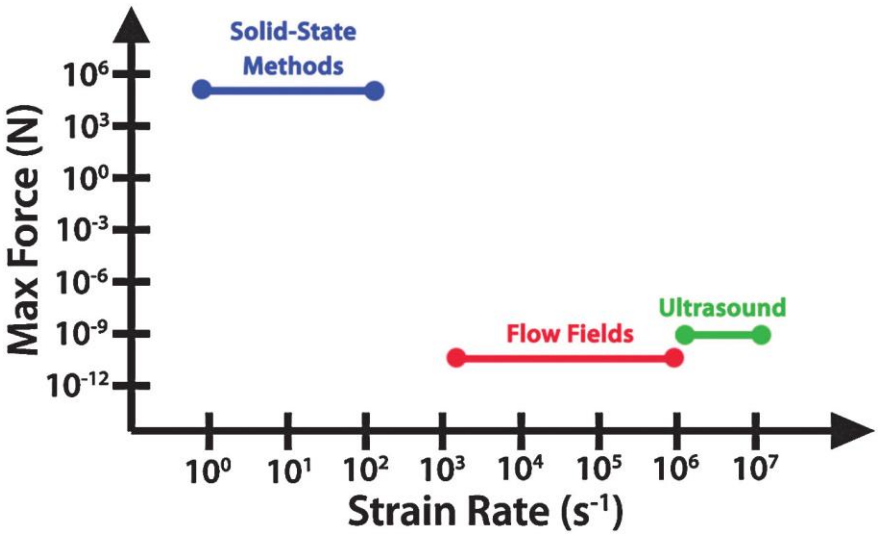

Figure 2. 7 Summary of Experimental Methods for Characterization of Mechanochemical Changes over a Range of Strain Rates and Size Scales, in Solution and Solid Polymers[96].

Current techniques for supplying a mechanical force are concerned with solution-based and solid-state methods. Figure 2.7 summarizes the range of strain rate and force of experimental methods used to characterize mechanochemical changes over a range of strain rates and applied force [96]. In general, solution-based methods provide faster strains rates, while solid-state methods offer a larger applied force. The strain rate is decided by molecular vibrations [122]. Molecular deformation must be faster than the molecular vibration of 10^4 s^{-1} to activate the scission [122]. The magnitude of necessary applied force is around 10^{-10} N which is related to the single bond strength [96]. Generally, bond cleavage is more likely to occur on weak covalent bonds than stronger bonds.

2.3 Motivation of This Work

Material degradation, caused by mechanical deformation, thermal expansion/contraction, radioactive contamination, or corrosion or electrical discharges, occurs inevitably in practical applications and reduces material performance greatly, especially in harsh environments [134-137]. For example, aerospace materials are exposed to large changes in pressure, temperature, speed and other elements. All these elements can cause large accumulations of stresses on the materials [138]. Beyond a certain threshold, microscopic cracks will begin to form and grow irreversibly, which eventually result in complete destruction of the materials and jeopardize public safety [139-141]. All aircraft is continuously subjected to cyclic loading/unloading and vibrational environments that initiate fatigue cracks and can propagate the cracks to failure in many components [139]. Current aircraft maintenance practice is costly to monitor and replace each component.

It is of great importance to monitor the health conditions of materials in service with regard to either potential life-safety or economic impact; therefore steps can be taken before materials reach failure. Besides aircrafts, damage detection in the products at the earliest possible time is quite desirable in industry. Scientists have been studying to develop damage detection technologies over the past few years. The process of implementing a damage identification method for engineering structures is referred to as structural health monitoring (SHM) which focuses on the study of damage identification in structural and mechanical systems. Vibration-based damage identification methods were developed by oil industry for offshore platforms during the 1970s and 1980s [139]. Because the damage location was unknown and the structure measurement was not accessible, this method was to simulate the candidate damage condition with numerical models, correlate these changes with those measured on a platform. This method was also applied in aircrafts of which component was inaccessible, like a control surface which was covered with a thermal protection system [146]. This was considered to be one of the most efficient damage detection methods in structural material assessment [142, 143]. Recent research has shown that the utilization of Electro-Mechanical (E/M) impedance methods allow for the direct identification of structural dynamics [144-146]. The mechanism is to couple small-size piezoelectric active sensors, like lead zirconate titanate, with the material structure. The measurements of the E/M impedance or admittance signatures are related to the mechanical impedance which is affected by the presence of damage. Lamb wave method is also suitable for suitable for structural health monitoring applications [147, 148].

Damage in a structure can be also by identified by a self-monitoring material, like crack sensors. Several types of crack sensors have been developed in the recent years. For example, piezoelectric films were developed to monitor crack initiation [149-151]. The output voltage signals from the sensors indicated a correlation with the applied stress intensity and the relationship with crack length. Employment of multi-walled carbon nanotubes (MWNTs) as filler in the epoxy matrix of a glass fiber reinforced composite enhanced electrical properties of the composite due to the high electrical conductivity of MWNTs [152]. This is a good method for monitoring the presence of impact damage by measurement of the electrical resistance, because the damage can be detected by significant increase in electrical resistance.

It is well known that the force distribution is not uniform throughout a material under stress. The force distribution is dependent on the coupling between the macroscopic forces and the molecular forces. The spectroscopic signal can be measured and imaged to quantify the force distribution. Also, it provides the advantage of easy detection. Therefore, many efforts have been devoted to develop methods of detecting damage precursors or force sensing in terms of visibility.

The stress applied can be made visible by a mechanochromic material in which the mechanical energy is translated to activate a chemical transformation with a visible color change indicating areas under stress or offering a warning signal before reaching mechanical failure. Testing devices can be coupled with optical spectroscopy to study these mechanochromic materials. Materials which depend on changes in physical molecular packing modes which respond to mechanical stimuli can be also used as

sensors [153-156]. Weder et al., as a pioneer in organic mechanofluorochromism, demonstrated that tensile deformation could facilitate substantial changes in the luminescent properties of linear low-density polyethylene (LLDPE)–dye blends by the destruction of dye aggregates [157]. The deformation color can be tuned by varying the electronics of the dye molecules. While the solubility of the organic dye in the polymer matrix limits the application of this system in some polymer materials.

Materials that respond to external stress with a color change are already known, but most of the color change processes are activated by the disruption or formation of non-covalent bonds. In recent years, mechanophore-containing solid-state polymers which give a visible color change upon the scission of covalent bonds have caused a great deal of interest, since this expands the scope of applications by allowing a variety of polymers to be accessed.

One type of optic activated mechanophore-linked polymer, which could mechanically induce luminescence emission, had been studied by Sijbesma et al. [158]. The smart polymer showed luminescence even at very low stress. Polymers incorporating the bis(adamantly)-1,2-dioxetanes unit enabled transduction of force into luminescence by opening of the four-membered dioxetane ring with subsequent ketone product relaxation from its excited state to the ground state. This mechanically activated a temporal visible luminescence color which could be tuned by suitable acceptors which harvest energy transfer (Figure 2.8) [158]. However, the time for monitoring the mechanically induced luminescence was very short, which restricted its use in practical applications.

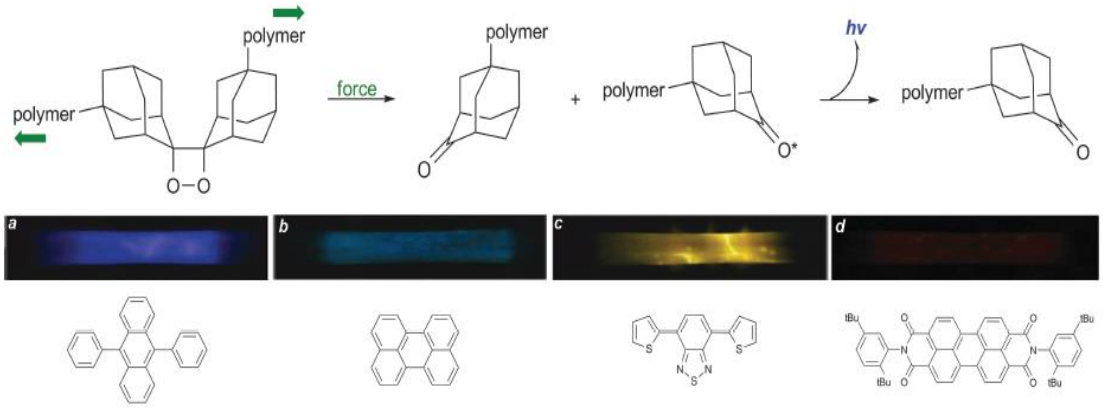

Figure 2. 8 (top) Mechanically Induced Decomposition of a Polymeric Bis(adamantyl) dioxetane to Keto-Intermediates Resulting in Blue Ehemiluminescence. (Bottom) Optical Images Obtained during Stretching of the Polymeric Film with Various Acceptor Molecules[135].

Pyran-based organic compounds, like spiropyrans, spirooxazines, naphthopyrans, are well known chromogenic materials of which structure changes occurs in company with a color change induced by temperature or light [159-162]. They exhibit photochromic and thermochromic transformations changing from a colorless to a colored form induced by a specific functional group cleavage, of which the process can always be recovered [160, 163]. However, color change induced by external force in pyran-based compounds is not well reported. Davis et al. made a very important breakthrough in this filed. They synthesized spiropyran-linked elastomeric polymers which could act as a force sensor in response to the stress loading [98]. They applied tensile testing and simultaneous optical spectroscopy to examine force-induced scissile transformation; this response was accompanied by a color change through a mechanically induced 6-electrocyclic ring-opening reaction from colorless spiropyran to colored merocyanine conformations, described in Figure 2.9. Because thousands of mechanophore units can be linked on the polymer, the force distribution can be detected by color change.

Here the goal is to apply a mechanophore as the color change trigger in solid-state materials. Mechanochemical activation would yield visible changes in the polymer matrix that could be directly detected with the naked eye, or it could be characterized precisely by fluorescence intensity changes with the help of a UV-Vis spectrometer. The design and synthesis of new optical signal mechanophores can open more opportunities in producing advanced "smart" materials which can be used in the applications of stress-sensing and crack/failure early detection. Combined with the modifications of the incorporated backbone polymers like elastomers or rigid polymers, the materials can be designed properly to respond and adapt to the mechanical environment differently as needed.

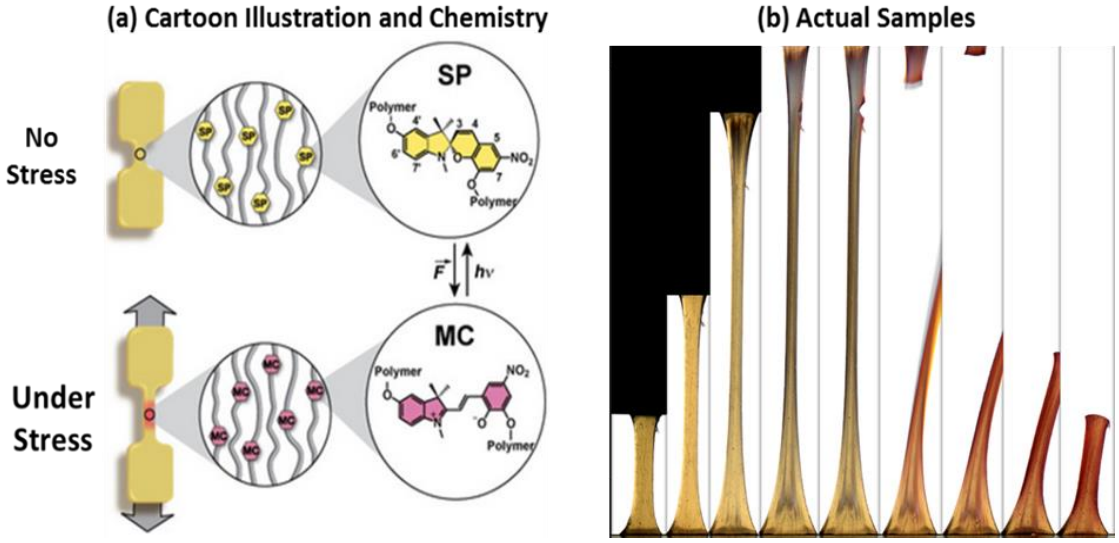

Figure 2. 9 (a) Cartoon Illustration of Poly(methyl acrylate) with Embedded Spiropyran-Based Mechanophores Structure and Stress Induced Reaction; (b) Optical Progressive Images of an Actual Dog-Bone Sample of a Mechanophore-Linked Elastomer during Tensile Loading[98].

As the demand for mechanophore-based functional composite materials or multi-functional composite materials has increased, our research is motivated by the following.

1. Compared to other “smart” materials, there are limited solid “smart” materials that are stress-sensitive. Solution-based polymers have been reported to have high selectivity of polymer chain scission under stress, but the demands for the involvement of water make them limited to certain practical applications. Stress-sensitive polymeric materials have found some useful applications in its solid-state, like in crack sensors. However, solid-state mechanophore-based polymers are not well understood.
2. The current study of mechanochemistry emphasizes more on pure and traditional polymers which solely relies on individual chemistry/reaction mechanisms which are often limited. To move into engineering applications and compete with conventional chemical synthesis, we designed a new type of mechanically responsive polymer blends system to identify the damage location through mechanically induced color change. This physical blending of the polymer matrix and the mechanophore-linked polymer provides a simple method for the fabrication of mechanophore.
3. Several studies incorporate spiropyran and other mechanophores into the backbone of linear, thermoplastic or elastomeric polymers such as poly(methyl acrylate), causing the mechanophore activation in these systems to require relatively large deformation [98]. The mechanophore incorporation can be very varied, thus the force transfer through polymer structure will be different. A mechanophore requires an appropriate position relative to the polymer backbone, because mechanophores can only be force-activated if the force can be effectively transferred through the bulk material to individual chains, then to the cleavable

bonds on the mechanophore units. The scheme in Figure 2. 10 (a) represents typical thermoplastic polymers, which during tensile deformation, the polymer chains first align before chain breakage, requiring a larger deformation than for the cross-linked schemes shown in Figure 2.10 (b, c).

4. Notably missing from the mechanochemistry literature is the incorporation of mechanophores into networked thermosets, such as epoxy. Rather than the traditional thermoplastics and elastomers, thermosets find ubiquitous use due to their excellent mechanical and physical properties. For example, epoxies are widely used in automobiles, aircraft, sports equipment and other areas due to their excellent mechanical performance, thermal stability and flame retardancy [164-167]. Our goal is to design multifunctional polymeric materials with vast performance improvements in selected properties enabling key Army capabilities. The systematic experimental study of incorporating cycloalkane-based mechanophores into thermosets such as epoxy will allow for early crack sensing and open new avenues compared to other mechanophores, including improving mechanical and thermal properties, increasing sustainability in severer environments, and overcoming previous limitations inherent to thermoplastics. For further application, glass fibers are will be embedded into epoxy matrix to enhance its mechanical and thermal properties. The schematic illustration is described in Figure 2.11. Glass fiber reinforced composite keep the properties of glass fiber and epoxy. Besides, the composite materials have a combination of properties that cannot be achieved by either glass fiber or polymeric matrix alone. Embedded glass fibers are the main load-carrying constituent, protected by the

polymeric matrix from chemical degradation and mechanical abrasion. Therefore, the glass fiber reinforced epoxy composites, due to their high specific strength and stiffness at the low cost, are widely used in various structural applications where they are subjected to constant and variable amplitude fatigue loads in service, like aeronautic, naval and construction [168-172].

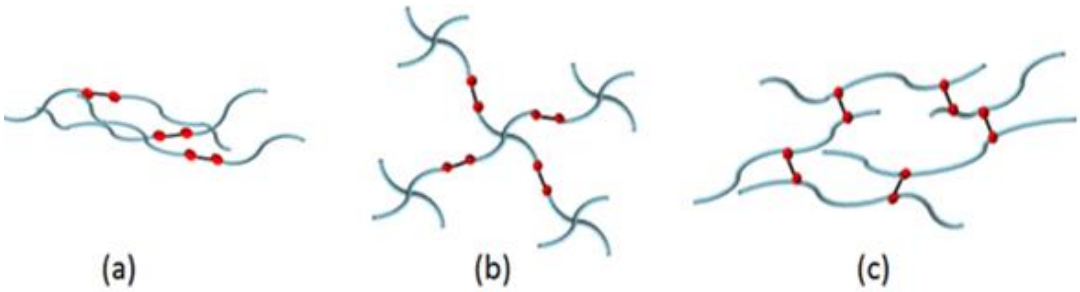

Figure 2. 10 (a) The Location of Mechanophore Units in Thermoplastics; (b,c) Cross-Linked Polymers. The Mechanophore is Colored in Red.

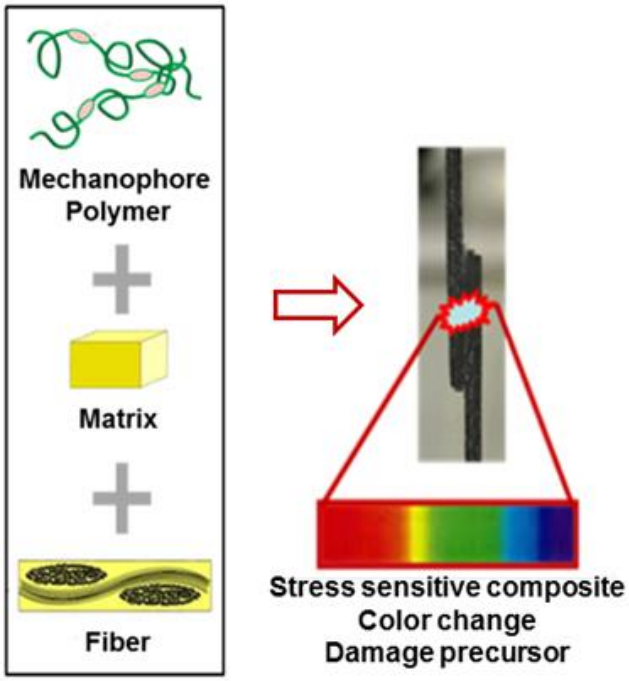

Figure 2. 11 Schematic Approach by Blending the Mechanophore-Linked Polymer to Composite Matrix Applied as Stress-Sensitive Material which can Response to Force by Color Change.

In this work, two types of mechanophores will be utilized, cyclobutane and cyclooctane, the former formed from cinnamoyl and the latter formed from anthracene upon photodimerization. In the study of cyclobutane as mechanophore functional group, we applied epoxy as the matrix. Epoxies find ubiquitous use due to their excellent mechanical performance. Cured epoxy resins are generally quite brittle, with a propensity to crack if exposed to sufficient stress and strain, leading to irreversible damage such as microcracking. A cyclobutane-based polymer was used as a crack sensor: 1,1,1-tris(cinnamoyloxymethyl) ethane (TCE) was dimerized into cyclobutane rings under photoirradiation. This cyclic product has been proved to efficiently generate fluorescence emission upon the cleavage of the cyclobutane ring [173]. The mechanical and thermal properties of polymers are significantly affected by the molecular structure. TCE has trifunctional mer units on each molecule. It forms the three-dimensional networks under UV photoirradiation. For comparison, a second polymer, poly (vinyl cinnamate) (PVCi) with the functional group as the side chain on the polymer to form a cross-linked polymer, was selected. PVCi is commercially available and very prominent in photochemistry with some attractive characteristics [174-176].

The cyclobutane-based polymer was produced by photodimerization of the C=C double bond from cinnamoyl function group of TCE and PVCi, respectively. Cyclobutane-based polymers were dispersed in epoxy as a self-sensing crack sensor. When the polymer blends undergo crack formation and propagation, the cyclobutane is mechanochemically cleaved to afford the chemicals that is capable of strong fluorescence emission, indicating the location of the crack in the epoxy (described in Figure 2.12). In this work, the effect of the functionalization of two different cyclobutane-based cross-

linked polymers on the thermal and mechanical properties of new epoxy matrix composites was investigated and the relationship of the stress-spectroscopic signals of the composites was also studied.

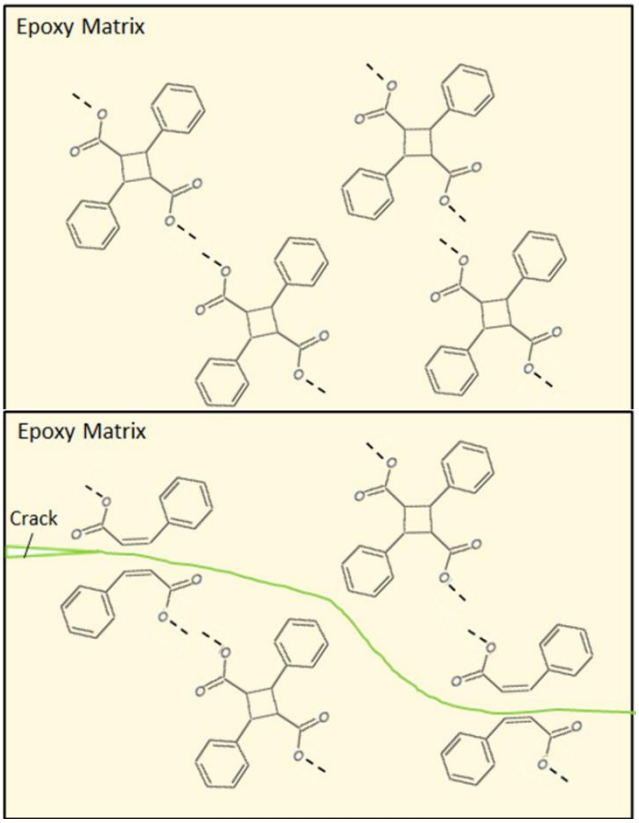

Figure 2. 12 Depiction of the Blending Approach to Create a Stress-Sensitive Material. (Top) before Crack Formation; (Bottom) after Crack Formation.

Similar to the mechanism of fluorescence emission from the cleavage of cyclobutane, the cyclooctane moiety generated fluorescent emission upon the cleavage of cyclooctane, as described in Figure 2.13. It can be explained by the regeneration of anthracene that exhibited fluorescence under UV light. Cyclooctane moiety can be synthesized through dimerization of anthracene moiety. The force-triggered generation of anthracene is expected to allow for early damage detection as the anthracenes exhibit

over 10 times the absolute fluorescence quantum yield compared to the cinnamates, due to the molecule containing three conjugated benzene rings [177]. Because of the superior quantum yield, an order of magnitude less individual mechanophore molecules are needed to break in cyclobutane to observe the same fluorescence that occurs with TCE or PVCi; thus, early damage when only few molecules are broken should be able to be observed. Also, the quantum yield corresponds to the amount of damage retained in the polymer, providing a function by which to predict damage in the overall material. This high quantum yield also provides the possibility of detecting damage deep in the polymer matrix as well as the early damage precursor functionality, making the anthracene moiety more desirable to be used as a fluorescent sensor in practical applications. Also, it is reported that the longer conjugated system will bring the excitation/emission to longer wavelengths, generating the possibility for naked eye observation [178]. Two cyclooctane-based polymers, dimerized from poly(9-anthraldehyde) and poly(9-anthracenecarboxylic acid), have been successfully utilized as crack-sensors in poly(vinyl alcohol) coatings [177]. Additionally, anthracene has been briefly studied as a mechanophore, operating under a quite different mechanism, by the use of a Diels-Alder adduct of anthracene and phenyltriazolinedione as a cross-linker in PDMS, which was activated by the release of a small molecule when a force was applied [179]. In our work, the functional polymer was prepared as a film, and then the relationship of the stress-spectroscopic signals was investigated through the tensile test.

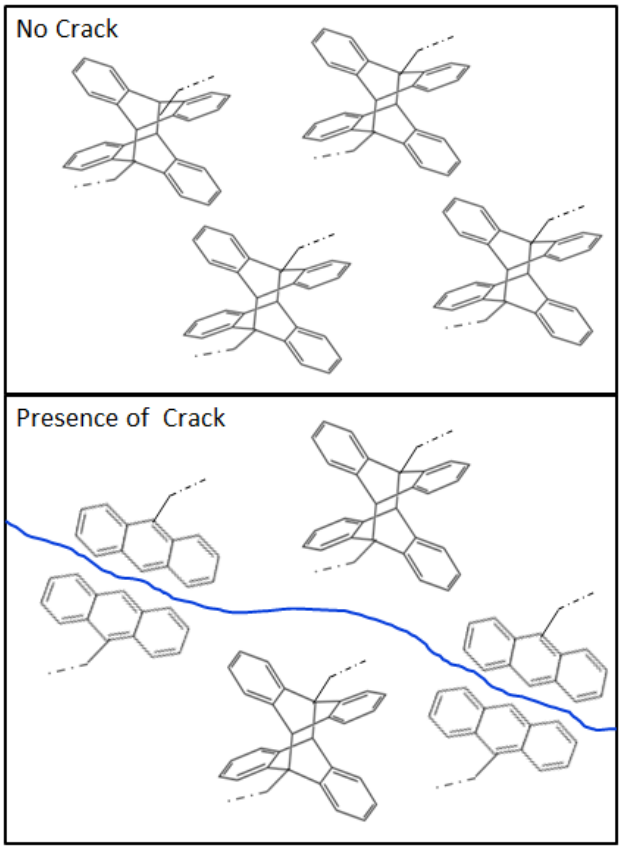

Figure 2. 13 Depiction of the Mechanism of the Cyclooctane Applied as a Crack Sensor.

CHAPTER 3
METHODOLOGY

3.1 Preparation of Cyclobutane-based Polymers

3.1.1 Materials

Unless otherwise stated, all the materials and reagents listed below were used as received. 1,1,1-tris(hydroxymethyl)ethane (99%), cinnamoyl chloride (98%), tetrahydrofuran (≥99.9%), 4-(dimethylamino)pyridine (≥99%),dichloromethane (≥99.8%), ethanol (≥99.5%) and poly(vinyl cinnamate) (PVCi, average Mn 45,000-55,000) were purchased from Sigma-Aldrich. Sodium chloride (≥99%) and water (HPLC) were purchase from Fisher Scientific. Epoxy resin FS-A23 (digycidylether of bisphenol F, DGEBPF) and epoxy hardener FS-B412 (diethylenetriamine, DETA) were purchased from Epoxy System Inc.

3.1.2 Synthesis and Sample Preparation

Synthesis of 1,1,1- tris(cinnamoyloxymethyl) ethane (TCE)

1,1,1-tris(hydroxymethyl)ethane (1.2 g, 10 mmol) and 4-(dimethylamino)pyridine (4.4 g, 36 mmol) were dissolved in 100 mL of tetrahydrofuran (THF) [180]. Cinnamoyl chloride (6.0g, 36 mmol) was dissolved in 30 mL of THF. Two solutions were mixed together and refluxed for 7 hours in a nitrogen atmosphere with medium stirring speed. The final mixture was dried with a rotary evaporator at reduced pressure in a water bath with temperature controlled at 40-50 ℃. After removing excess THF, beige colored solid powders were obtained. 30 mL of dichloromethane (CH_2Cl_2) were added to dissolve the impure solids. Next, the dissolved solution was washed three times with 15 mL of saturated aqueous sodium chloride. A crude product was obtained upon the evaporation

of the solvent from the organic layer. The insoluble solids were removed via dissolving in hot ethanol. The prepared mixture was covered and kept to cool over night at room temperature. Following cooling, a white crystalline product was precipitated from the prepared solution. The product was collected through filtration and washing with cold ethanol. Next, the final product was dried in the vacuum oven overnight at room temperature to obtain 3.5 g (68 % yield).

The chemical structure of TCE was confirmed by NMR. ^{1}H NMR and ^{13}C NMR spectra were recorded on a Bruker 400 MHz spectrometer in deuterated solvent $CDCl_3$. All chemical shifts are reported in parts per million (ppm) with the internal tetramethylsilane (TMS) signal at 0.0 ppm as a standard.

Mass spectra were recorded on a JEOL LCmate scanning the magnet from m/z 200 to m/z 600. Ionization mode was atmospheric pressure chemical ionization (APCI), which is a chemical-ionization technique which uses gas-phase ion-molecule reactions at atmospheric pressure. The sample was prepared in dichloromethane/methanol (DCM/MeOH, 2:1, v/v).

Preparation of Polymer Blends Containing Epoxy and Cross-Linked TCE and PVCi Polymer

To prepare cross-linked TCE or PVCi polymer, a small amount of TCE or PVCi solid was first dissolved in CH_2Cl_2. The solution was applied on a clean silicon mold to form a thin film and placed in vacuum to evaporate the excess CH_2Cl_2. All the silicon molds and glass slides used for sample preparation were used with pretreatment with

mold release agent. After the CH_2Cl_2 was evaporated, the thin film was photoirradiated at 302 nm for 4 hr.

To prepare polymer/epoxy polymer blends, the solution was added to DGEBPF and dispersed well using an ultrasonic probe sonicator (Sonics VibraCell, 500 W model). The mixture was placed in a vacuum chamber at 50 ℃ to evaporate the CH_2Cl_2 until the mass of the mixture remained unchanged for an extended period, indicating that the excess CH_2Cl_2 was evaporated. The resin mixture was cooled down to room temperature before DETA was added and mixed ($M_{TCE\ or\ PVCi}$: M_{Epoxy}=1:10; M_{DGEBPF} : M_{DETA}= 100:27). The mixture was sonicated in an ice bath to prevent any premature curing. After the mixture became homogenous, the mixture was poured into the silicon molds and moved into a vacuum chamber to degas for 30 minutes, followed by photoirradiation conducted by an UV lamp with 302 nm wavelength (UVP, UVM-28). According to the manufacturer's data, the light density is approximately 1300 $\mu W/cm^2$ at a distance of 3 cm. The sample was exposed to UV for 4 hr and cured overnight at room temperature. Neat epoxy sample followed the similar procedure. After simple machining, the sample was ready for test. The average dimension of cubic sample was 3×4×8 mm. For dynamic mechanical analysis (DMA), the mixture was poured onto the flat silicon surface with a glass cover placed on top. The curing procedure was the same for the cubic sample. To make polymer/epoxy thin film, the uncured epoxy was compressed between two glass slides.

Preparation of Glass Fiber Reinforced Composite (GFRC) Sheet

A weighed amount of polymer blends containing uncured epoxy and 10 wt.%

TCE were taken in a clean beaker and mixed thoroughly before the glass fiber mats were reinforced. The uncured composite sheet was cured under a load of 50 kg for 10 minutes and photoirradiation for 4 hours under UV light at 302 nm wavelength. In order to achieve further improved performance, the composite sheets were post-cured at 60 ℃ overnight in an oven and allowed to cool gradually. The sample size for characterization was $30 \times 80 \times 0.4 mm^3$.

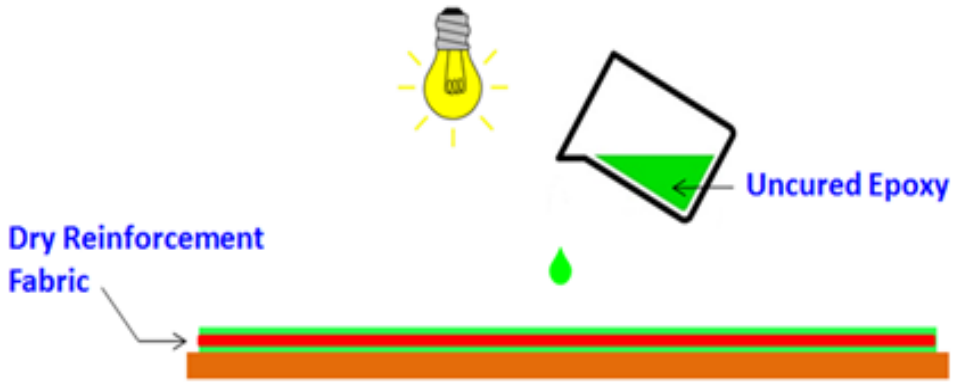

Figure 3. 1 Schematic Illustration of Preparation of GFRC Sheet.

3.1.3 Characterization

Photochemical Properties of Cross-Linked Polymers

UV-Vis spectrometer was used to confirm the dimerization of cinnamate functional groups and further studied the reaction kinetics. All UV spectroscopic analyses were performed on a UV-Vis spectrometer (Perkin Elmer Lambda 18) which was equipped with a UV light source by a deuterium lamp ($\lambda < 319.2$ nm) and visible light ($\lambda >$ 319.2 nm) by a tungsten halogen lamp to provide usable wavelength from 185-900 nm. The machine was turned on 30 minutes prior to experimental measurements in order to warm up and stabilize the halogen and deuterium lamps. 0.05 mg of TCE was dissolved

in 4 ml of CH_2Cl_2. 4 ml TCE solutions were transferred to a quartz cuvette of 1 cm path length. Neat CH_2Cl_2 solution was used as reference. The solution spectra of absorbance were measured ranging from 200 nm to 400 nm. The wavelength scan intervals are set up to 4 nm with scan speed of 120 nm/min. For the "Baseline" scan, one empty cuvette you used in the measurement was placed in a single holder labeled with "reference" and another empty cuvette of the same type in another holder labeled with "sample". After the "Baseline" scan, the empty "reference" cuvette was filled with the neat solvent and the "sample" cuvette was filled with the sample solution. And then the cuvettes were put back to the holder for the measurement. After the first absorbance measurement of the sample (before UV photoirradiation), the vial was taken out and exposed under the UV lamp for 15 minutes. The vial was put back into the holder and another absorbance measurement was taken. The spectra of the samples were recorded before exposure and after each exposure at selected intervals of time. For the measurement of PVCi solution, 0.09 mg of PVCi was dissolved in 4 ml of CH2Cl2 and transferred to a clean cuvette. Follow the same procedure to run the experiment. All measurements were performed using same parameters at room temperature.

The Fourier transform infrared spectroscopy (FT-IR) was used to further confirm the function groups of interest. All the spectra were analyzed on Bruker IFS 66V/S FTIR spectrometer with OPUS 4.0 software. Mid-IR KBr beamsplitter was used. Detector setting was set as "DLATGS" and scanner velocity as "7;20.0KHz". Infrared transmission spectroscopy (IR) was performed in a vacuum using an FTIR spectrophotometer in the spectra region from 600 to 4000 cm^{-1} at a resolution of 2 cm^{-1} with an average of 64 scans. A clean KBr disk was placed into a spectrometer disk holder

in the chamber. Evacuate the chamber to get rid of water vapor and CO_2. Check signal section and collect background until amplitude was read. A small amount of TCE was dissolved in CH_2Cl_2 to prepare a dilute solution. Place a small drop of the solution onto the KBr disk. The solution was spread out on KBr disk and left without any disturbance. Place the disk back to the hold and evacuate the chamber again. CH_2Cl_2 was then evaporated off in a vacuum at room temperature to form a very thin film. A spectrum of the sample was run. After the measurement was taken, vent the sample chamber. Take the KBr disk and exposed it under the UV lamp for half an hour. Then put it back to the holder and repeat the experiment. The spectra of the samples were recorded before and after exposure to UV photoirradiation at room temperature. All the parameters were kept constant through the FTIR analysis.

Thermal and Mechanical Properties of Polymer Blends

The effect of the addition of the cross-linked polymer to the epoxy on glass transition temperature (T_g) was studied. The measurements of T_g were carried out with differential scanning calorimeter thermal analysis (DSC). The experiments were performed in a nitrogen atmosphere using TA Instruments Q20. Throughout the DSC work, temperature and heat flow calibrations were performed following standardized procedures. After a heating and cooling cycle up to 70 ℃ with a heating ramp rate of 10 ℃ /min to eliminate the thermal history, Tg was analyzed from the data of the second heating scan from -20 to 120 ℃ at 10 ℃/min, with the TA Universal Analysis software. All samples were contained in tzero pans with lids. An empty pan with a lid was used as reference. Reference and sample pans were placed onto the holder, respectively. Each

holder was equipped with its own heater and temperature sensor. The masses of the samples were in the range of 6–9 mg on average.

Thermogravimetric analysis (TGA) monitors the amount and rate of change in the mass of a sample as a function of temperature or time as a sample is heated at a programmed rate in a controlled atmosphere. The measurements are used primarily to determine the thermal stabilities of materials. In our experiment, TGA was carried out using a TA Instruments (TGA Q500 machine). The sample masses were in the range of 15 to 20 mg and were placed in a tared platinum crucible. All the samples were heated from 30 to 600 ℃ at a heating rate of 10 ℃/min in nitrogen. The weight loss was monitored and recorded as a function of temperature.

Dynamic mechanical analyzer (DMA) was used to measure the glass transition temperature, storage modulus, loss modulus. Cross-link density of the neat epoxy, the epoxy blended with TCE polymer and the epoxy blended with PVCi polymer can be calculated through DMA. Experiments were performed in a tension mode using a TA Instruments Q800. Multi-Frequency/Strain was used. Thin films of polymeric blend were mounted onto the tension clamp and the temperature was ramped from 25 to 120 ℃ at a heating rate of 5 ℃/min. The frequency was 1Hz under amplitude control. The strain amplitude was set at 25 μm. The size of each sample was 0.2 - 0.5 mm in thickness, 4 - 7 mm in width, and 8 – 13 mm in length.

To verify the stress responsiveness of cyclobutane-based polymers by fluorescence generation, the polymers was first coated on a clean polyethylene substrate. The fluorescent images on the coating surface were taken before and after the substrate

was bent. In order to establish the relationship between the stress and fluorescent signal, compression test was conducted. In the compression test, the compressive stress-strain behavior of these systems was obtained by MTS servo hydraulic test system, as shown in Figure 3.2. All the tests were conducted at room temperature. The samples were lubed by silicone oil to minimize the friction between the compression plate and the samples. Tests were run in displacement control in the longitudinal direction at loading rate of 1 mm/min.



Figure 3. 2 Cubic Epoxy Sample Loaded on MTS Servo Hydraulic Test System For Compression Test.

Fluorescence Observation

A small amount of TCE or PVCi was dissolved in CH_2Cl_2. The solution was applied on polystyrene substrate to form a thin film and was placed into a vacuum oven in the dark to dry the solvent. The film was photoirradiated under an UV lamp with 302

nm wavelength for 4 hours. The substrate was gently bent to generate cracks on the uncoated side of the substrate. The cracked surfac was observed by an imaging system consisting of a phase contrast inverted microscope (Nikon Elipse TE300) outfitted with a Hamamatsu Orca 3CCD and a Olympus DP26 color camera that allows real-time digital image capture by exposure to 330-380 nm UV light. The emission filter was for the wavelength between 435 – 485 nm.

To study the stress responsiveness of epoxy blends, the neat epoxy and epoxy blend samples were punched by a hammer to generate cracks. Furthermore, the neat epoxy and epoxy blend cubic samples were compressed to different strains. The compression was conducted on a MTS servo hydraulic test system. Tests were run in displacement control in the longitudinal direction at loading rate of 1 mm/min. The surface of the samples was monitored under the UV microscope. To calculate the fluorescent intensity on each image, the fluorescent image with 8-bit was processed through ImageJ. After the image was open, select the area of interest using any of the drawing/selection tools. Under the "Analyze" menu select "set measurements". Select "Area" and "Integrated density". After select "Measure" under the "Analyze" menu, a popup box with a stack of values showed.

On the GFRC sheet, damages were applied with a metal tool. The fluorescence density changes were recorded and compared before and after damage through a fluorescent microscope. A uniaxial tensile fatigue test was performed on a GFRC sheet. A 4 mm wide notch in the center of the specimen was made firstly to create an initial damage to make the stress concentrate on the area around the hole. The specimen loaded

on the test frame of the machine TestResource 800L can be seen in Figure 3.3. The specimen was cycled in a load-controlled mode at stress ration (R), $\sigma_{min} / \sigma_{max}$=0.1 on a uniaxial fatigue frame operating with a sinusoidal waveform at a frequency of 2 Hz, as seen in Figure 3.4. Maximum stress (1000 N) and minimum stress (100 N) was constant for each cycle of a test. The number of fatigue cycles was recorded. After the application of a certain number of load cycles, the test was stopped. The specimen was dismounted and photographed under white light and UV microscope. Then the specimen was remounted and fatigue cycles continued. The fluorescent intensity at each fatigue cycle loading was calculated through ImageJ. The average data against cycles were plotted. The fatigue fracture surface of the specimen was sputter coated with a thin layer of gold to observe the fatigue crack growth under scanning electron microscope (SEM). The specimens for SEM were sputter coated with gold and viewed by SEM-XL30 (FEI). Specimens for SEM experiments were prepared by placing a piece of GFRC sheet onto newly cleaved mica substrate and applying Au coating of 10 – 15 nm thick using a sputter coater.

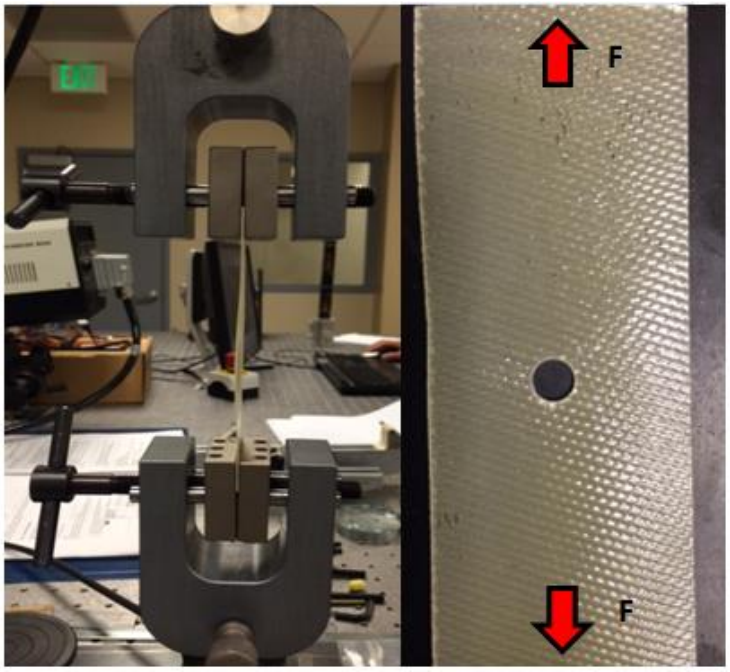

Figure 3. 3 (Left) GFRC Sheet Loaded on the Test Machine TestResource 800L; (Right) GFRC Sheet with a Hole in the Center before Loaded.

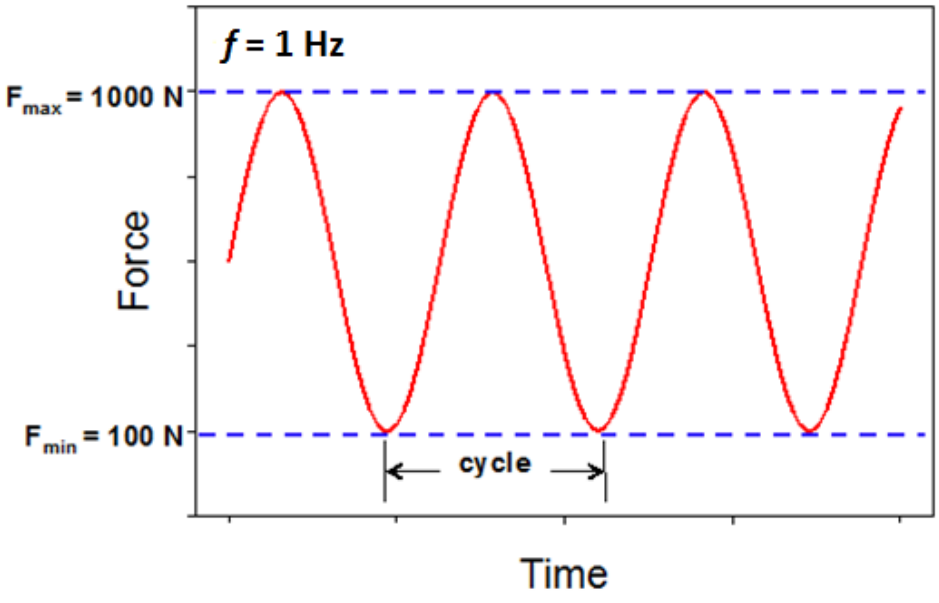

Figure 3. 4 Cyclic Loading Parameter in Tensile Fatigue Test.

3.1.4 Molecular Dynamics Simulation

To investigate the effect of epoxy cross-linking degree on thermal and mechanical properties and compare with experimental data, molecular dynamics simulations were conducted by Dr. A. Chattopadhyay's group [181]. Taking into account the chemical curing process of epoxy resin and hardener, the carbon-nitrogen covalent bond generation was implemented numerically. Based on the numerical method for covalent bond generation, the cross-linking degree estimations of epoxy-based system were conducted using a stochastic method, which made the MD simulation results more reliable. The MD simulation was also used to investigate the relationship between the cross-linking degree and T_gs.

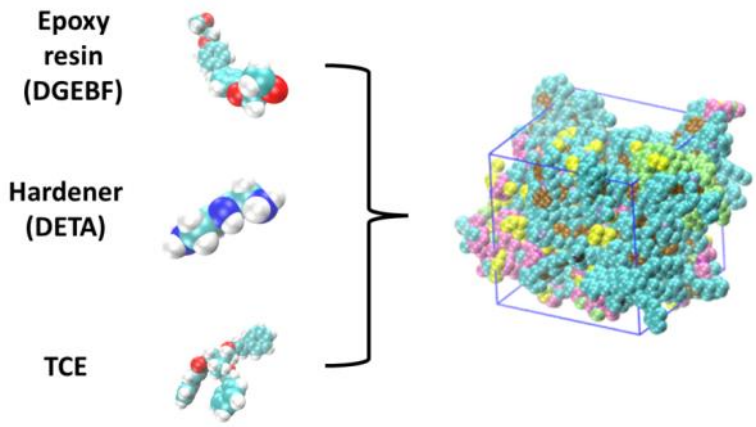

Figure 3. 5 Schematic of Smart Polymer Unit Cell.

Molecular structures of DGEBF and DETA were used to construct a neat epoxy unit cell for MD simulation. A well-mixed epoxy-based system was guaranteed through the distribution of all the molecules randomly in each unit cell without overlap. The number of molecules was determined by the weight ratio 100:27 (DGEBF:DETA) which was used for making experimental samples in this study. The epoxy unit cells were made

up of 65 molecules of digycidylether of bisphenol F (DGEBF) and 55 molecules of diethylenetriamine (DETA). The weight of TCE was 10% of the total weight of the neat epoxy unit cell. The smart polymer unit cells had the same number of DGEBF and DETA as neat epoxy with the addition of 5 molecules of TCE. Each system was cured at a different temperature, with temperature increasing in 10K from 250K to 450K at 1 atm. 500 MD simulations were performed to estimate cross-linking degree (defined as the ratio of the number of generated covalent bonds and the number of active site of epoxy resin) from the generated covalent bonds of each simulation. Thermal properties like T_g and mechanical properties like Young's modulus were calculated based on the corresponding cross-linking degree. All MD simulations were performed with Large-scale Atomic Molecular Massively Parallel Simulator (LAMMPS) in conjunction with MMFF.

3.2 Preparation of Cyclooctane-Based Polymers

3.2.1 Materials

Unless otherwise stated, all the materials and reagents listed below were used as received. Anthracenecarboxylic acid (99%), poly vinyl alcohol (PVA, Mw=31,000-50,000, 98-99% hydrolyzed), p-toluenesulfonic acid monohydrate (p-TSA, ≥98.5%), tetrahydrofuran (THF, ≥99.9%), N,N-dimethylformamide (DMF, anhydrous, 99.8%) and N-Methyl-2-pyrrolidone (NMP, anhydrous, 99.5%) were purchased from Sigma-Aldrich.

3.2.2 Synthesis and Sample Preparation

Synthesis of Poly-AC

Poly-AC was synthesized, following the reference [177]. It included two major

steps, dimerization and esterification. Dimeric anthracene was synthesized first through photo-dimerization. 2.00 g of AC was dissolved in 40 mL of THF under a nitrogen atmosphere. The solution was exposed to UV light with wavelength of 302 nm for 72 hr. During this time a white solid formed. The solid was filtered, washed with THF, and dried in the vacuum oven at room temperature. 0.20 g of Di-AC was dissolved in 30 ml of DMF. 0.40 g of PVA was dissolved in 8 g of NMP. The two solutions were mixed together with the addition of 0.184 g of p-TSA. The temperature of the reaction was controlled at 65 ℃ for 24 hr. The reaction mixture was dried in vacuum oven at 75 ℃ and washed with THF.

The dimerization of anthracenecarboxylic acid was confirmed through a UV-Vis spectrometer (Perkin Elmer Lambda 18) which was equipped with UV light source by a deuterium lamp ($\lambda <$ 319.2 nm) and visible light ($\lambda >$ 319.2 nm) by a tungsten halogen lamp to provide usable wavelength from 185-900 nm. An anthracenecarboxylic acid solution was prepared by dissolving a certain amount of AC in THF. 4 ml of dilute solution was transferred to a quartz cuvette of 1 cm path length. Neat THF solution was used as reference. The solution spectra of absorbance were measured ranging from 300 nm to 440 nm. The wavelength scan intervals were set up at 4 nm with scan speed of 120 nm/min. The spectra of the samples were recorded before exposure and after each exposure at selected intervals of time. All measurements were performed using the same parameters at room temperature.

The esterification process was confirmed through FT-IR spectra. The sample was analyzed on Thermo Nicolet 6700 FTIR with OMNIC software. The instrument integrates diamond ATR crystals which provide a very hard surface to withstand heavy

use. The solid mixture of reactants was placed on the center of the ATR accessory and pressed down on the optical crystal using the pressure controller. The spectrum was recorded at room temperature. The spectra were analyzed in the region from 600 to 4000 cm^{-1} at a resolution of 2 cm^{-1} with an average of 64 scans. The spectrum of final products was recorded using the same method. All the parameters were kept constant through the FTIR analysis.

Sample Preparation

The solution was first concentrated to one-half volume. Then the concentrated solution was poured to the silicon rubber mold and dried in the oven to form a thin film. The original film was trimmed to have the dimension of $20 \times 7 \times 1 mm^3$.

3.2.3 Characterization

To verify the A small amount of poly-AC was dissolved in NMP. The solution was applied on a black plastic substrate and dried in the vacuum oven in the dark. After the solution evaporated, a thin film was formed and coated on the substrate. To detect the stress sensitivity, The plastic substrate was bent slightly to generate cracks. the coated film was bent to generate micro-cracks. Images were taken to monitor the fluorescent change under the UV microscope.

To verify the stress responsiveness of cyclobutane-based polymers by fluorescence generation, the polymers was first coated on a clean polyethylene substrate. The plastic substrate was bent slightly to generate cracks. The fluorescent images on the surface of the coated substrate were taken before and after the substrate was bent. In order to establish the relationship between the stress and fluorescent signal, tensile test was conducted. Texture analyzer (TA.XT Plus Texture Analyzer) coupled with Texture

Exponent Software was used to measures the force involved in tension interaction of a probe with the polymer specimen. “Test Mode” was set as “Tension”; Pre-test speed and post-test speed were both 1 mm/sec. In tensile test, a rectangular poly-AC film was gripped at its two end and pulled to elongate. The film was extended to 20% and further 40% strain with a strain rate of 1% per second.

CHAPTER 4
RESULTS AND DISCUSSION

4.1 Cyclobutane-Based Polymers and Composites

4.1.1 Synthesis and Reaction Mechanisms

Synthesis of 1,1,1-tris(cinnamoyloxymethyl) ethane (TCE)

The synthesis of 1,1,1-tris(cinnamoyloxymethyl) ethane (TCE) followed a published method [173] described in Chapter 3. The TCE was obtained from 1,1,1-tris(hydroxymethyl)ethane and cinnamoyl chloride in the presence of 4-(dimethylamino)pyridine (4-DMAP), which is a derivative of pyridine. 4-DMAP is a useful nucleophilic catalyst for a variety of reactions. In the reaction of 1,1,1-tris(hydroxymethyl)ethane and cinnamoyl chloride, 4-DMAP serves as an esterification catalyst. The nitrogen center of 4-DMAP molecule features an electron-donating dimethylamino functional group, which makes it more nucleophilic than 1,1,1-tris(hydroxymethyl)ethane in attacking the carbonyl center of cinnamoyl chloride. This step produces acetylpyridinium ion which becomes more reactive than the original cinnamoyl chloride toward alcohol. In the following reaction, the oxygen from 1,1,1-tris(hydroxymethyl)ethane attacked the acetyl group of the acetylpyridinium ion to form the target product, TCE. The specific reactions involved are described in detail in Figure 4.1. Another purpose which 4-DMAP serves here is as a base. It neutralizes the protons generated in the reactions to prevent the high acid concentrations in the reaction.

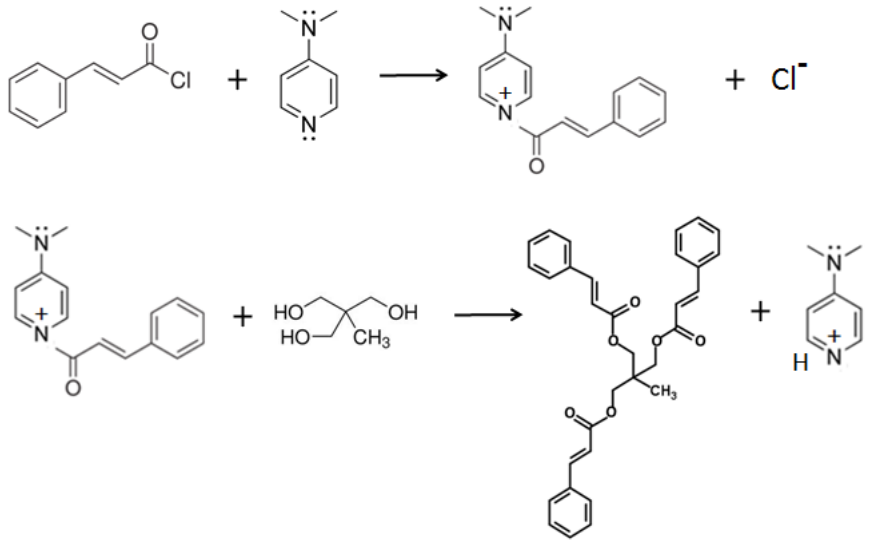

Figure 4. 1 Synthesis of TCE in the Presence of DMAP.

The synthesized product was dissolved in deuterated chloroform $CDCl_3$. ^{1}H NMR and ^{13}C NMR spectra were obtained using a Bruker 400 MHz spectrometer in a deuterated solvent $CDCl_3$. All chemical shifts were reported in parts per million (ppm). Tetramethylsilane (TMS) was used as a standard reference for calibrating chemical shift for ^{1}H and ^{13}C.The chemical shift of TMS was assigned as 0.0 ppm

(a)

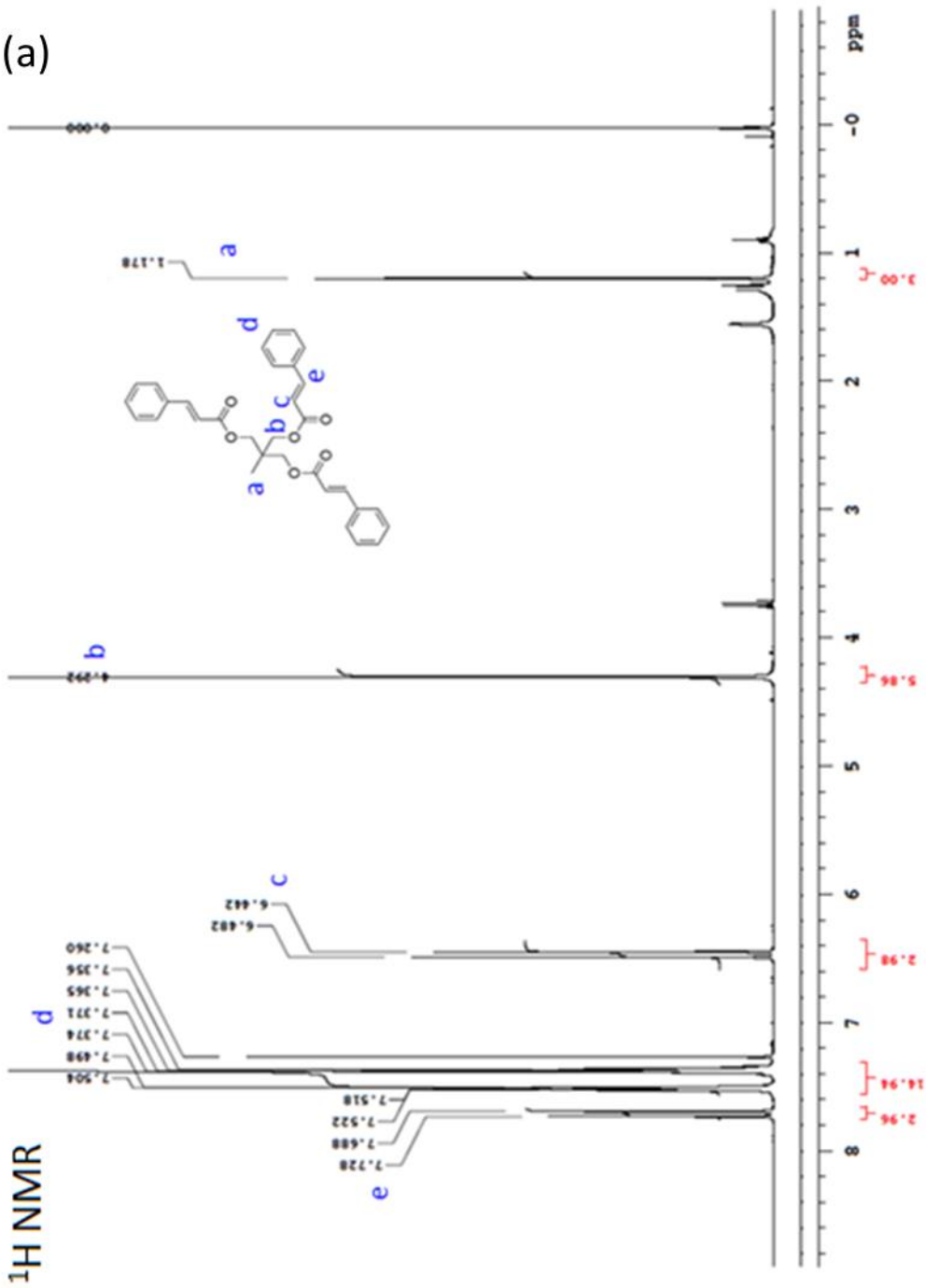

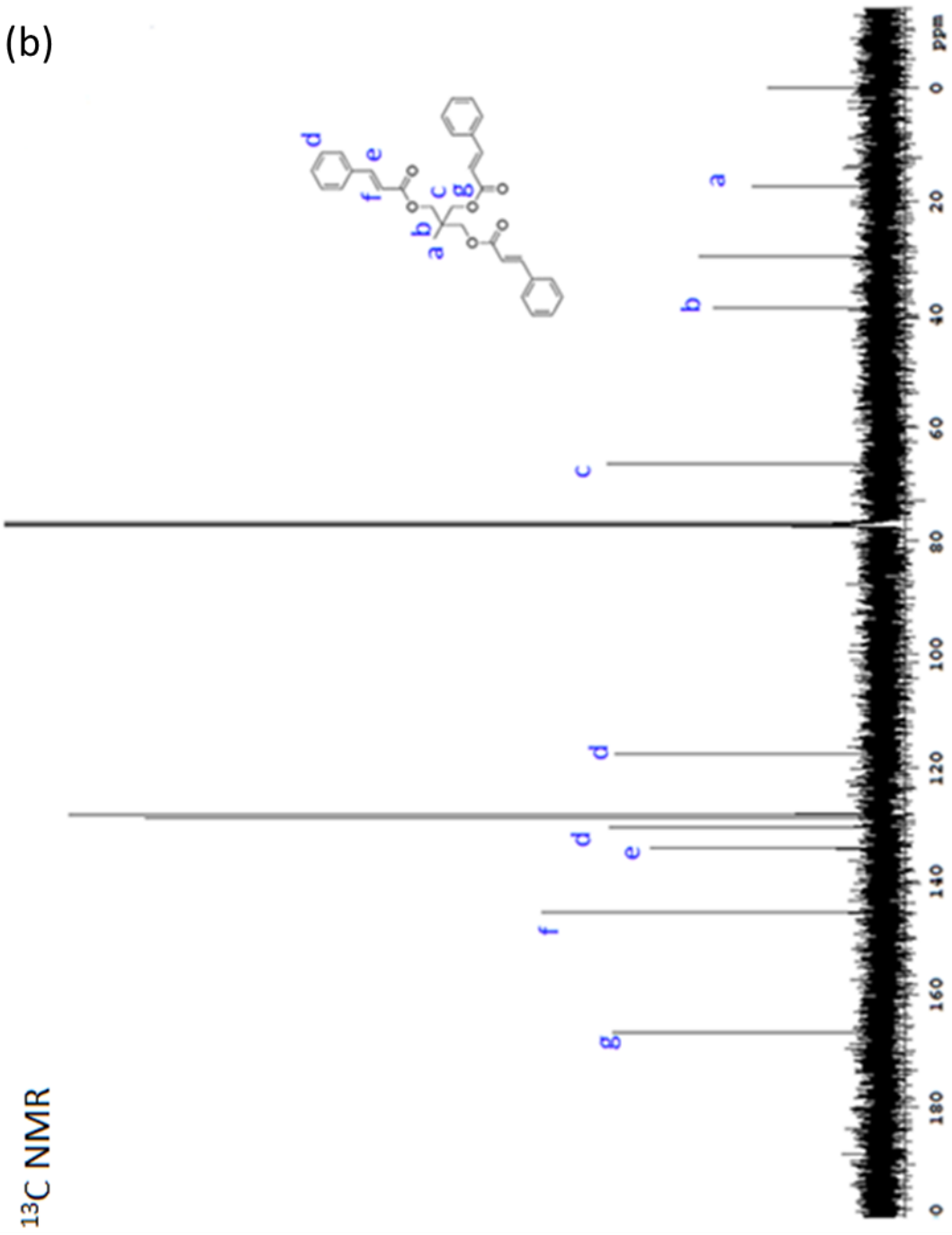

Figure 4. 2 (a) ^{1}H NMR and (b) ^{13}C NMR Spectra of TCE Dissolved in $CDCl_3$.

The ^{1}H NMR spectra, shown in Figure 4.2, provide information about the hydrogen. The singlet at 1.178 ppm corresponds to the hydrogen atoms at a primary carbon which is connected to a quaternary carbon. The singlet at 4.292 ppm corresponds to a secondary carbon. The doublet at 6.442 ppm and 7.688 ppm correspond to non-equivalent alkene hydrogens respectively. The multiplet within 7.260 and 7.504 ppm are the typical splitting pattern for benzene with one substituent. Three types of hydrogens all couple to each other to generate multiple separate peaks. ^{13}C NMR spectra, also shown in Figure 4.2, can further identify a carbon atom in a different environment within the molecule (Figure 4.2). Referring to the table of ^{13}C chemical shifts and the estimated corresponding integration numbers confirmed that the spectra matched the final molecule. The spectra are reported as (s = single, d = double, m = multiple, coupling constant(s) in Hz, integration), as summarized in Table 4.1.

Table 4. 1 NMR Data of TCE.

(a) ^{1}H NMR for TCE.

Label	Chemical Shift (δ, ppm)
a	1.178 (s, 3H, CH3)
b	4.292 (s, 6H, OCH2)
c	7.688 (d, 3H, phCH=CH)
d	7.260-7.522 (m, 15H, phenyl)
e	6.442 (d, 3H, phCH)

(b) ^{13}C NMR for TCE.

Label	Chemical Shift (δ, ppm)
a	17.402 (CH3)
b	38.839 (CCH3)
c	66.282 (OCH2)
d	117.544, 128.173, 128.895, 134,209 (phenyl)
e	130.436 (phCH)
f	145.411 (phCH=CH)
g	166.699 (carbonyl)

The information from the mass spectra provides fingerprints of the molecular formula. The sample for mass spectroscopy experiment was prepared in dichloromethane/methanol (DCM/MeOH, 2:1, v/v) and placed in a JEOL GCMate mass spectrometer. The molecular ion is observed at m/z = 511.2205 ($C_{32}H_{30}O_6$). Possible

ester exchange with MeOH gives a fragment peak seen at m/z=381.1709 ($C_{23}H_{25}O_5$) and 363.1596 ($C_{23}H_{23}O_4$) through rearrangement. The spectra and the speculated chemical structures are displayed in Figure 4.3.

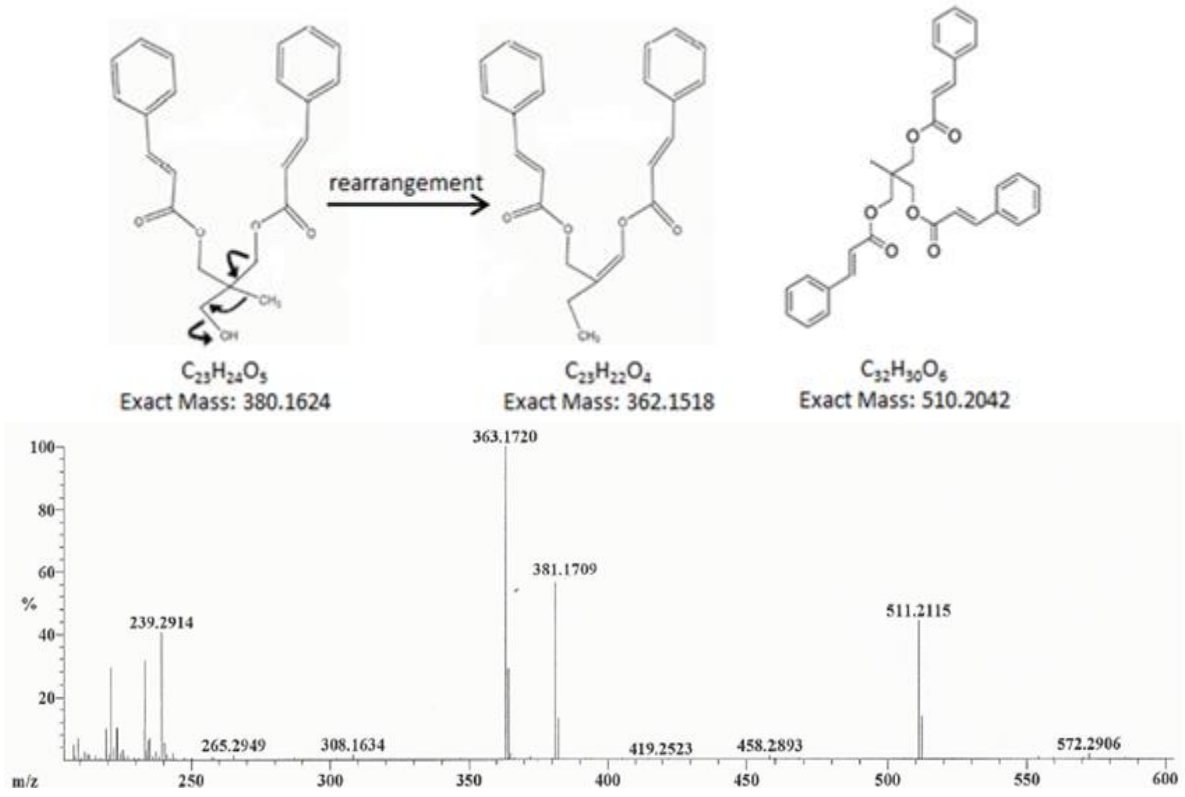

Figure 4. 3 Mass Spectra for TCE and the Main Chemical Structures.

Photosynthesis of Cyclobutane-Based Cross-Linked Polymer

It has been reported that the unsaturated chromophore cinnamoyl groups can undergo both trans-cis isomerization about the reactive double bond. The isomerization reaction is shown in Figure 4.4. More importantly, photocycloaddition of cinnamoyl derivatives can give cyclobutane-type dimers without addition of any photoinitiators [182, 183]. The light at specific wavelength is absorbed by one of the cinnamates and promotes one of the electrons from the highest occupied molecular orbital (HOMO) to the lowest

unoccupied molecular orbital (LUMO) to generate the electronically excited state. Some of the excited state decays back to the ground state or go to react with a ground state molecule. The photodimers can be formed from head to head and head to tail [2π+2π] cycloaddition between a UV excited cinnamoyl group of one molecule with an unexcited cinnamoyl group (ground state) of another molecule (Figure 4.5) [182]. Photodimerization is often believed to be the major reaction, while isomerization is minor and only favored in the early stages of UV irradiation [184]. In our experiment, each TCE has three cinnamoyl groups which can react with another TCE molecule to under UV light at 302 nm. A three-dimensional network will be formed based on the dimerization of TCE molecules with cyclobutane as the linkage.

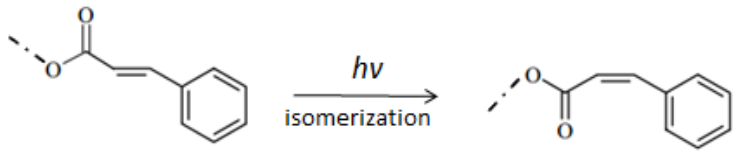

Figure 4. 4 Trans-Cis Photoisomerization of the Cinnamate Monomer.

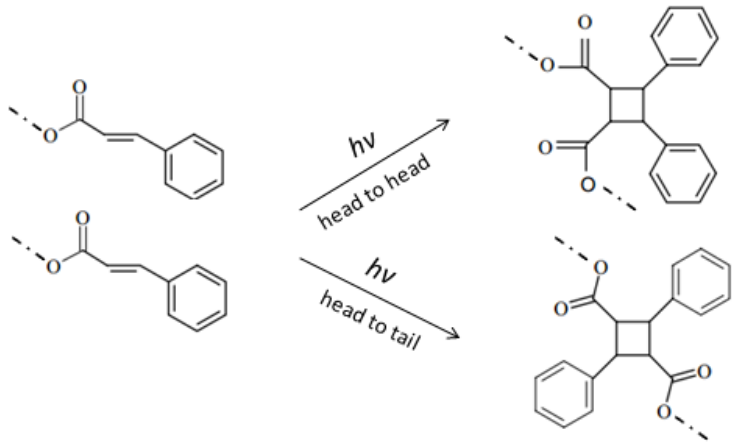

Figure 4. 5 Dimerization Mechanism of the Cinnamate Monomer.

The [2+2] photocycloadditon of the TCE was confirmed and analyzed using both UV-Vis and FTIR spectroscopy. Figure 4.6 displays the UV absorbance variation of TCE dilute solution as a function of time. It is well known that aside from cycloaddition, cinnamates also undergo isomerization during UV photoirradtion. Both the trans and cis cinnmates have absorption between 250 and 350 nm with a peak at around 280 nm, while the dimmer has no absorption in this range. If isomerization was the only photoprocess, an isosbestic point was observed at 250 nm [184]. From both spectra, it is seen that cycloaddition competes quite effectively with isomerization due to the disappearance of the isosbestic point. The spetra had a slight blue shift from 280 to 272 nm due to the change in chemical structure of cinnamate groups with irradiation. The strong UV absorbance ranging from 240 to 320 nm with the peak was centered at around 280 nm. This absorbance corresponds to the abundance of π-π^* transitions of the C=C double bond from cinnamoyl groups before photoirradiation [180, 184, 185]. The change in the absorbance value was monitored for continual irradiation, and it is facile to notice that the absorbance band decreases rapidly with exposure time and disappears almost completely within 30 minutes of photoirradiation, this implies that there is dimerization of C=C bond to cyclobutane.

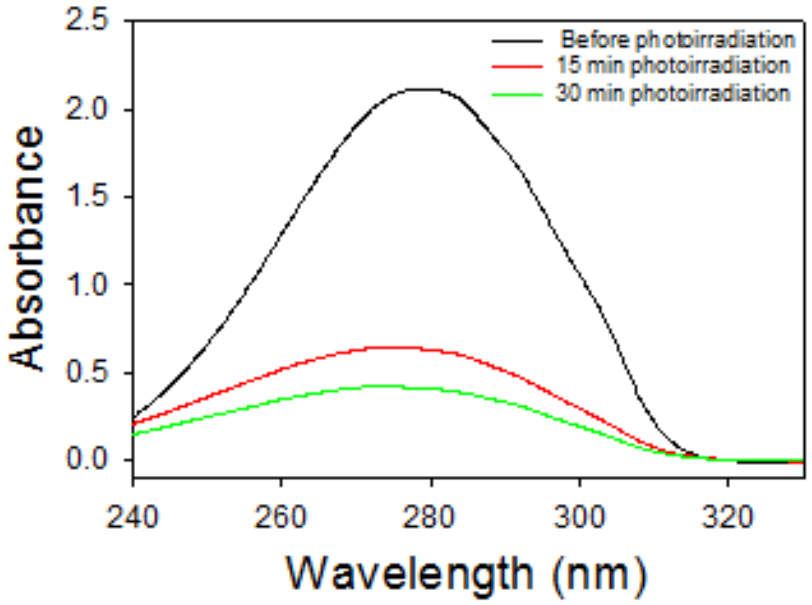

Figure 4. 6 The Change of UV Absorbance of TCE Solution as a Function of the UV Exposure Time.

Results from FTIR were also used to track the functional groups during photoirradiation. Figure 4.7 shows the FTIR spectra of TCE film before and after irradiation with UV light. Before UV irradiation, two peaks were observed at 1713 cm^{-1} and 1637 cm^{-1}. These two peaks corresponded to the conjugated C=O stretching vibration and vinylene C=C stretching vibration, respectively [185, 186]. After 0.5 hour of photoirradiation, the C=C peak disappeared. This disappearance can be explained by the consumption in forming cyclobutane through photodimerization, which destroyed the conjugation in the entire π electron system [180]. The C=O peak shifted to higher wavelength number with decreasing absorbance. That could be attributed to the loss of π–conjugation from C=C double bond [186, 187]. These observations were entirely consistent with the photo-cross-linking of cinnamoyl groups under UV photoirradiation

which was depicted in Figure 4.6 and the spectral assignments, which were depicted schematically on the right hand side of Figure 4.7.

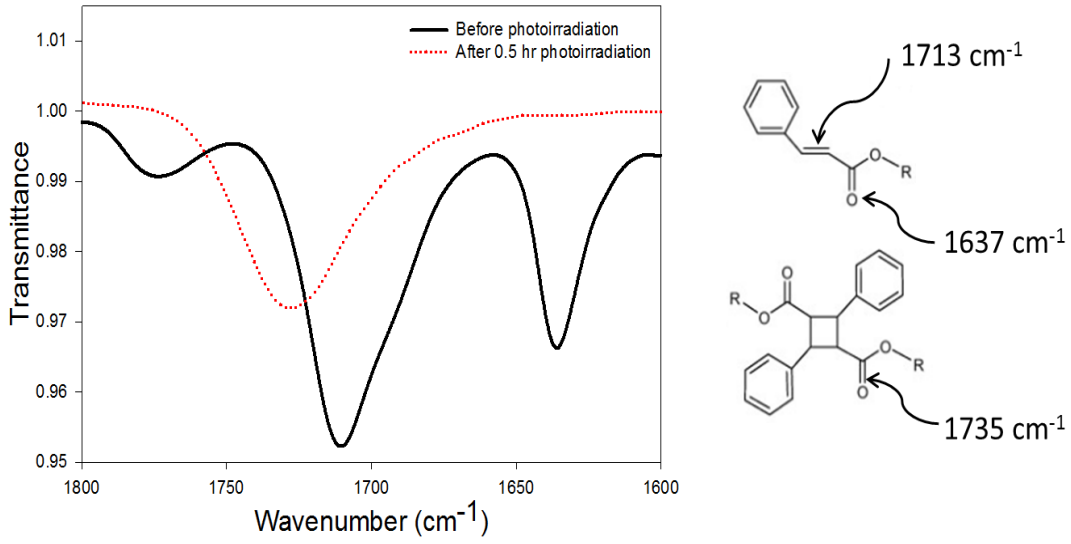

Figure 4. 7 IR Spectra of TCE Film on a KBr Disk before and after Photoirradiation.

Under UV photoirradiation at 302 nm, each TCE molecule has three active sites to react with another TCE molecule to form the three-dimensional networks with cyclobutane as linkage Therefore, the photosynthesis of TCE can generate the molecular structures as shown in Figure 4.8 (top). The covalent bonding is cyclobutane, produced from the [2+2] cycloaddition of two cinnamoyl groups. The mechanical and thermal properties of polymers are significantly affected by the molecular structure. For comparison, another type of cinnamoyl-based chemicals, poly(vinyl cinnamate) (PVCi), was selected. PVCi has very different molecular structure from TCE. Its structure is displayed in Figure 4.9. PVCi has relatively long and flexible polymer chain. The cinnamoyl functional groups are grafted as the side chain. The poly vinyl chains are

linked through active sites at various positions along their lengths, as shown in Figure 4.8 (bottom).

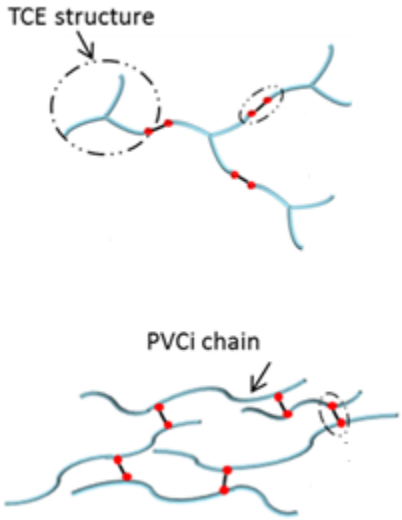

Figure 4. 8 Schematic Illustrations of a Three-Dimensional Network of TCE (top) and Cross-Linked Polymers of PVCi (bottom). Active Sites are in Red.

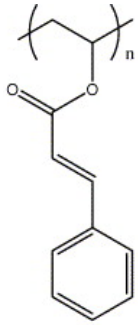

Figure 4. 9 Chemical structure of PVCi.

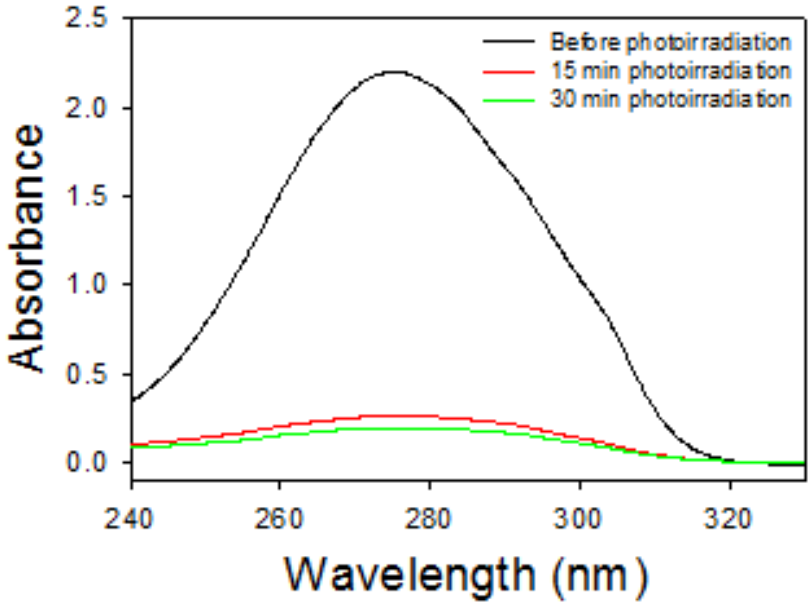

Figure 4. 10 The Change of UV Absorbance of TCE Solution as a Function of the UV Exposure Time.

The [2+2] photocycloadditon of the PVCi was confirmed by UV-Vis spectroscopy. Figure 4.10 displays the UV absorbance variation of PVCi dilute solution as a function of time. Similar to the behavior of TCE solution, the UV absorbance before photoirradiation was strong. The peak centered at around 280 nm corresponds to the abundance of π-π* transitions of the C=C double bond. The absorbance decrease as UV exposure time indicated the dimerization of C=C bond to cyclobutane. IR spectra also confirmed the cycloaddition process under UV exposure. In Figure 4.11, there are two peaks at 1710 cm^{-1} and 1636 cm^{-1} before UV irradiation. The peak at 1710 cm^{-1} attributes to the conjugated C=O stretching vibration and the peak at 1636 cm^{-1} corresponds to vinylene C=C stretching vibration. After 0.5 hour of photoirradiation, the C=C peak disappeared due to the consumption in forming cyclobutane through photodimerization

The C=O peak shifted to 1734 cm^{-1} with decreasing absorbance due to the loss of π conjugation from C=C double bond.

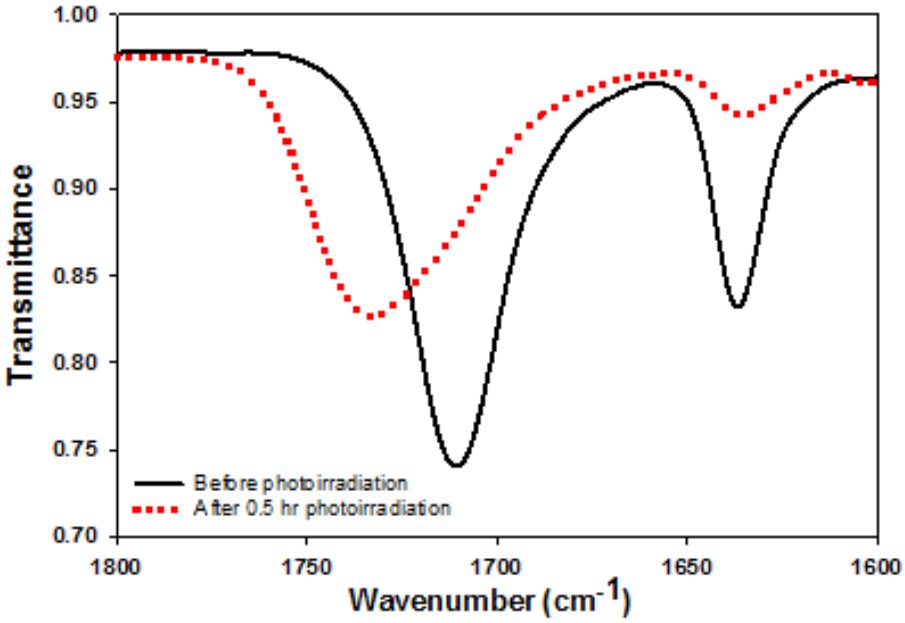

Figure 4. 11 IR Spectra of TCE Film on a KBr Disk before and after Photoirradiation.

The cross-linking efficiency can be calculated according to the rate of disappearance of the C=C double bond of cinnamoyl group using the equation 4.1 [188]:

$$\text{conversion } (\%) = (A_0 - A_t)/A_0 \times 100 \qquad (4.1)$$

where A_0 is the absorbance before irradiation at the maximal wavelength and A_t is the corresponding absorbance during photoreaction. The conversion is estimated based on the absorbance change at 280 nm, because both TCE and PVCi had the maximum absorbance at 280 nm. The conversion to cyclobutane as a function of time is plotted in Figure 4.12. The estimated conversion is over 80% and 90% for TCE and PVCi, respectively. In addition, it was observed from both plots that conversion (%) was never

100%. This could be explained by the steric hindrance from the formation of a cross-linked network.

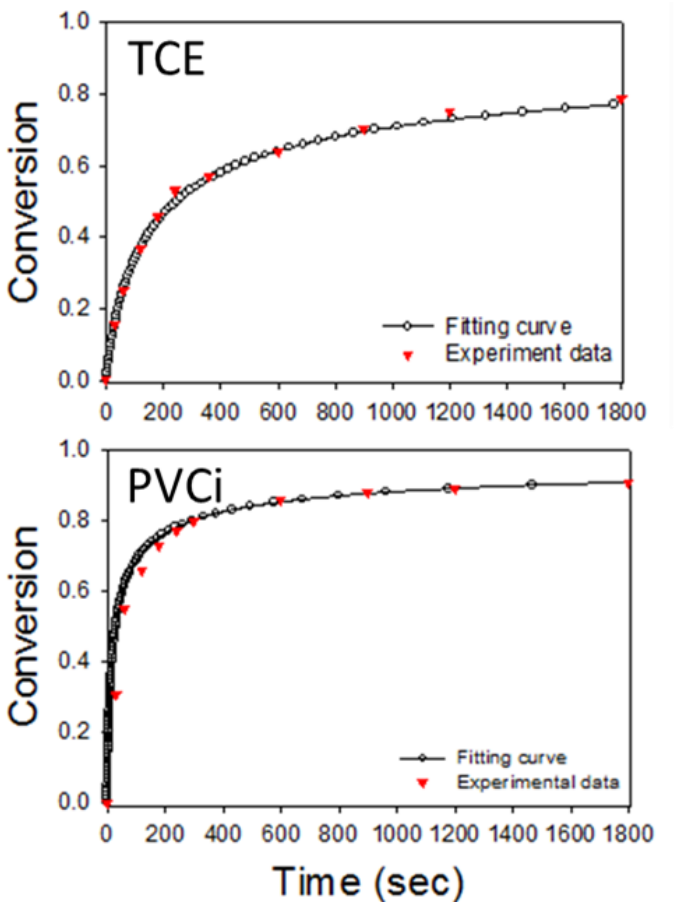

Figure 4. 12 The Change in the Conversion of (top) TCE and (bottom) PVCi as a Function of the UV Exposure Time.

The reaction conversion rates of TCE and PVCi in solution as a function of conversion were plotted and displayed in Figure 4.13. The experimental data of both chemicals shows the behavior of nth-order kinetics reaction under photoirridiation. The kinetics reaction equation 4.2 is described below [189],

$$\frac{\partial \alpha}{\partial t} = k\,(1-\alpha)^n \qquad (4.2)$$

where α is the reaction conversion, t the irradiation time, k the rate constant, and n the reaction order.

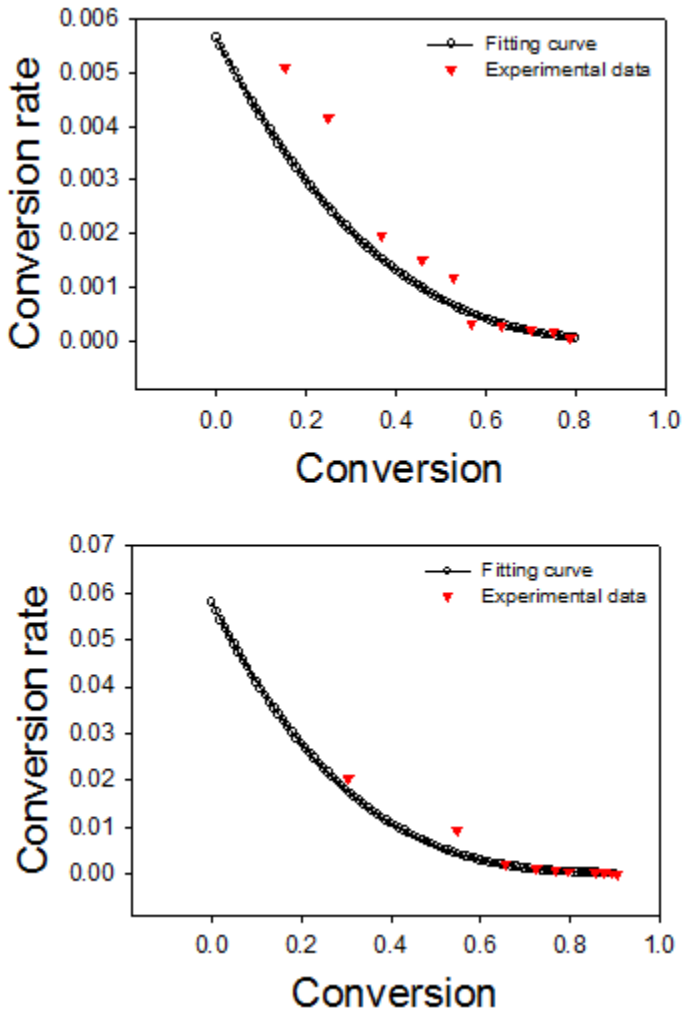

Figure 4. 13 Comparisons of Conversion Rates between the Experimental and Theoretical as a Function of the Conversion of the Photoreactive Molecule: (top) TCE and (bottom) PVCi.

The reaction rate constant and order for both chemicals are summarized in Table 4.1. Both Figure 4.13 and Table 4.2 show that the conversion rate and rate constant of TCE were lower than those of PVCi. The formation of cyclobutane ring by

photodimerization of cinnamate groups has a specific constraint for spatial conformation. PVCi may have more freedoms of mobility than TCE to perform the photoreaction due to the contribution of poly vinyl backbone which may increase the mobility of cinnamoyl groups on the chain. The conversion rate for both chemicals decreases with conversion, this trend can be explained by the growth of a cross-linking network, which decreases the mobility of molecule.

Table 4. 2 Kinetic Parameters of the Photoreactive Molecules.

Photoreactive Unit	k	n
TCE	0.0056	2.8
PVCi	0.058	3.3

4.1.2 Glass Transition Temperature and Cross-link Density Analysis

Epoxy Curing Process

Epoxy was used as matrix material in this study. Notably missing from the mechanochemistry literature is the incorporation of mechanophores into networked thermosets, such as epoxy, rather than the traditional thermoplastics and elastomers. Epoxy finds ubiquitous use due to their excellent mechanical and physical properties Epoxy systems contain two components, resin and hardeners, as seen in Figure 4.14. Epoxy resin is digycidylether of bisphenol F (DGEBPF) and epoxy hardener is diethylenetriamine (DETA). The number of molecules are determined by the weight ratio 100:27 (DGEBF:DETA) which is used for making experimental samples in this work.

When these two components are mixed, they chemically bond together. Once the chemical reaction is finished, they it yields a rigid polymeric material. A well-mixed epoxy-based system is required for good curing. The general curing reaction observed in this study was a nucleophilic attack of the amine on the terminal carbon of the epoxy monomer [190], this fundamental mechanism is depicted in Figure 4.15. First, the lone pair of electrons on the nitrogen atom (on the amine group of DETA) can easily attack the carbon atom on the end of the epoxy monomer (on the epoxide group of DGEBF). Second, a new C-N bond forms, and the C-O bond is broken simultaneously, which leaves a negative charge on the oxygen and a positive charge on the nitrogen. Third, the electrons on oxygen can then bond to the hydrogen on the positive nitrogen to generate O-H covalent bond. When the O-H bond is formed, the hydrogen leaves the nitrogen with its electrons. The amine group keeps one hydrogen which can react with another epoxide group. The number of hydrogens on nitrogen decides how many epoxide groups can react with. DETA has five hydrogens on nitrogen atoms and can generate five C-N covalent bonds; both end nitrogen atoms have two active sties and centered nitrogen atom has one active site. In this reaction manner, the resin monomers are tied together by hardener, which forms a network, as described in Figure 4.16. In experiment, not all active sites participate in the curing reaction. The possible explanation can be that the steric hindrance prevents the adjacent active sites from bonding; or the mixture is locally not well-mixed.

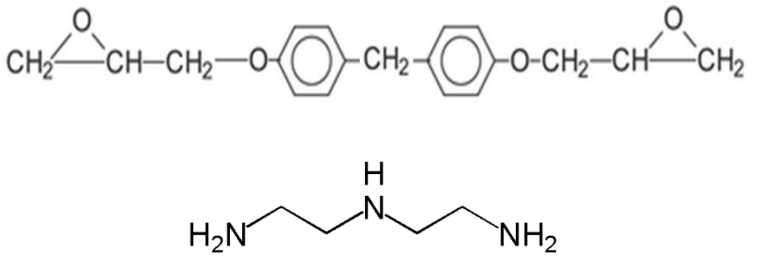

Figure 4. 14 Chemical Structure of Epoxy Resin (top) and Hardener (bottom)

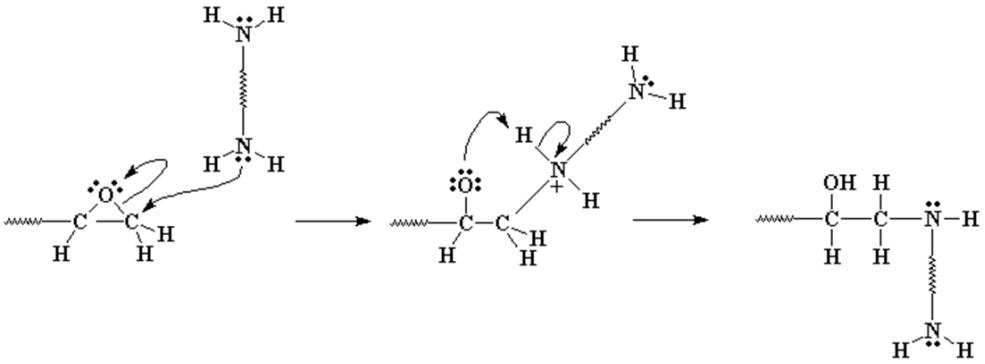

Figure 4. 15 Epoxy Curing Mechanism[176].

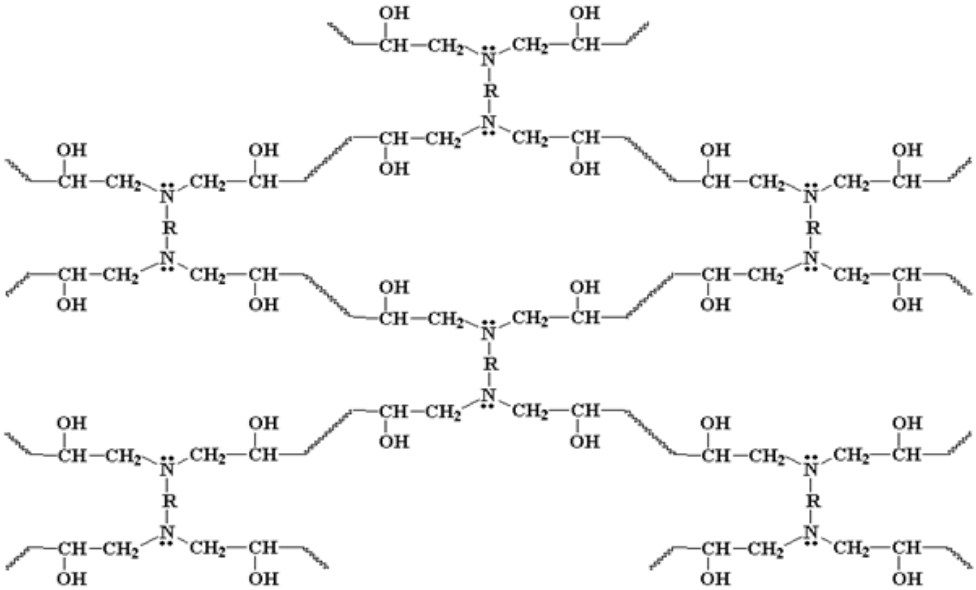

Figure 4. 16 Cured Epoxy Network[176].

Glass Transition Temperature

The effects of cyclobutane-based polymer on glass transition temperature (T_g) of the epoxy were studied by non-isothermal DSC scans. The tested samples included cross-linked TCE polymer, cross-linked PVCi polymer, neat epoxy and polymer blends. Polymer blending was recognized as a very common way to develop new materials, as prepared as in Figure 4.17. Once the epoxy resin, hardener and TCE molecules were mixed well, the mixture was exposed under a UV light. It was assumed that the epoxy curing reaction and [2+2] photocycloaddion of TCE occurred simultaneously.

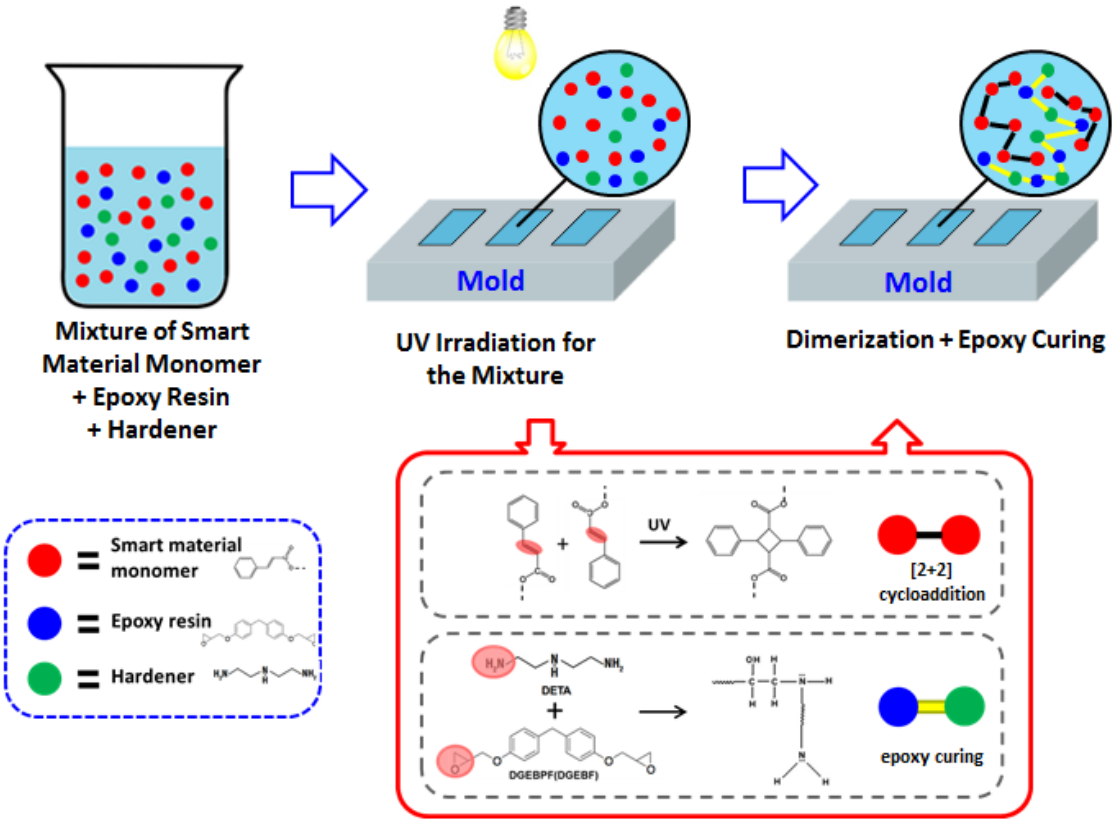

Figure 4. 17 Schematic Illustration of Preparation of Polymer Blends.

Appropriate blending can offer extended useful properties compared to the neat one. However, immiscibility and incompatibility are the main problems for most polymer blends which limit the usefulness in practical application. For example, incompatible polymer blends have poor mechanical properties because of high interfacial tension which always lead to mechanical failure when stress is applied. The value of T_g can tell us if the polymer blends is miscible or immiscible at all [191]. Full miscible blends are characterized by a single glass transition temperature, unaffected by the number of polymer components the blends contain. In contrast, immiscible blends for binary components usually have two glass transition temperatures.

The DSC curves were displayed in Figure 4.18. There is only one glass transition temperature observed for both blends, suggesting the epoxy and polymer were well miscible with each other. The miscibility of the blends was further confirmed by scanning electron microscope (SEM) through the detection of phase separations and interfaces. The specimens for SEM were sputter coated with gold and viewed by SEM-XL30 (FEI). Specimens for SEM experiments were prepared by placing a piece of epoxy or polymer blends onto mica substrates and applying Au coating of 10 – 15 nm thick using a sputter coater. The SEM images are displayed in Figure 4.19. It was found out only one phase existing either in neat epoxy or blends, indicating cyclobutane-based polymer was miscible well with epoxy.

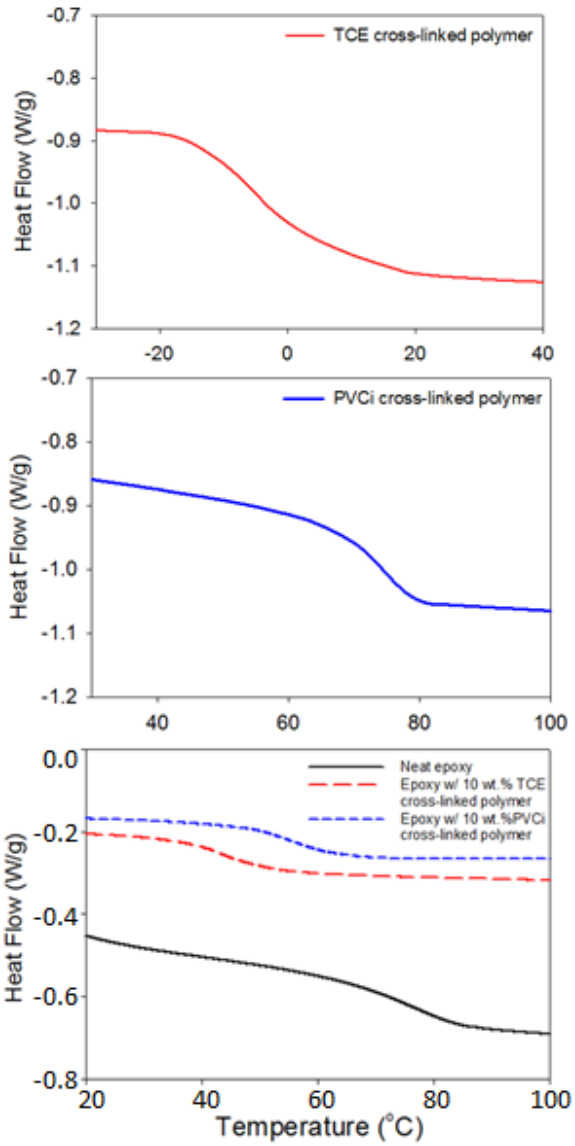

Figure 4. 18 DSC Curves for the (top) TCE Cross-Linked Polymer; (middle) PVCi Cross-Linked Polymer; (bottom) Neat Epoxy and Epoxy/Polymer Blends.

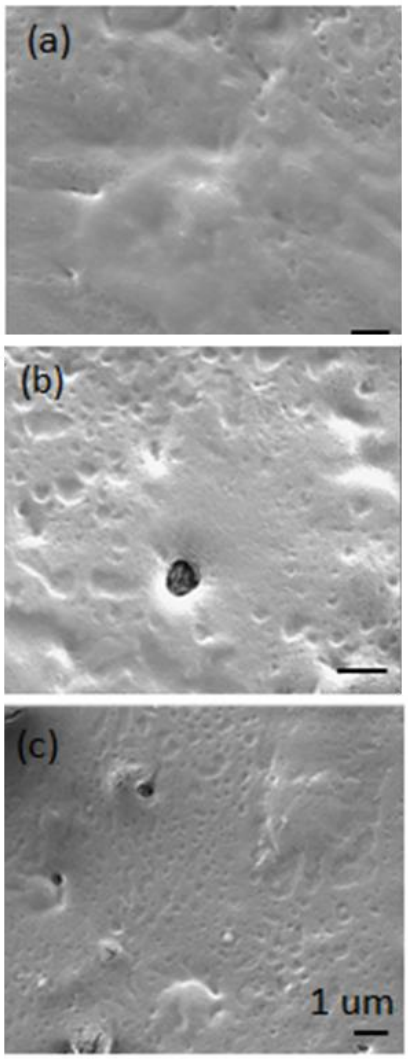

Figure 4. 19 SEM Micrographs of (a) Neat Epoxy (b) Epoxy with 10 wt. % TCE Polymer (c) Epoxy with 10 wt.% PVCi Polymer.

T_g was taken as the mid-point of the change of slope in DSC curves. The T_g for pure cross-linked TCE and PVCi polymer was measured to be around 0 ℃ and 75 ℃. The addition of cross-linked TCE or PVCi polymer to epoxy significantly changed the glass transition temperature. T_g was found to be 72 ℃ for neat epoxy, 43.85 ℃ and 54.67 ℃ for epoxy with cross-linked TCE and PVCi polymer, respectively. Theoretically, in the case of a binary polymer blend system, T_g of the miscible polymer blend can be

estimated empirically by the Fox equation and Wood equation by substituting T_gs of the individual components and their weight percentages in the blend. The expressions of the Fox equation and Wood equation are described below [182],

$$\frac{1}{T_g} = \frac{x_1}{T_{g,1}} + \frac{1-x_1}{T_{g,2}} \quad (4.3)$$

$$T_g = x_1 T_{g,1} + x_2 T_{g,2} \quad (4.4)$$

T_g corresponds to the blend, $T_{g,i}$ to pure component i, and x_i is the mass fraction of component i. Normally The estimation of T_g from Wood equation is higher than Fox equation. T_g of the blend system of epoxy with 10 wt. %, 20 wt. % and 30 wt. % of TCE or PVCi polymers were measured on DSC. The data are summarized in Table 4.3. The comparison between curve generated from equation and the experimental data is plotted as a function of weight fraction, as displayed in Figure 4.20.

Table 4. 3 T_g of Polymer Blends with Various Contents of Cross-Linked TCE or PVCi Polymers.

Polymer blends	T_g (10 wt.%), °C	T_g (20 wt.%), °C	T_g (30 wt.%), °C
Epoxy w/ TCE polymer	43.9±2.5	38.3±0.7	29.2±1.5
Epoxy w/ PVCi polymer	54.7±1.8	39.0±1.4	36.6±3.2

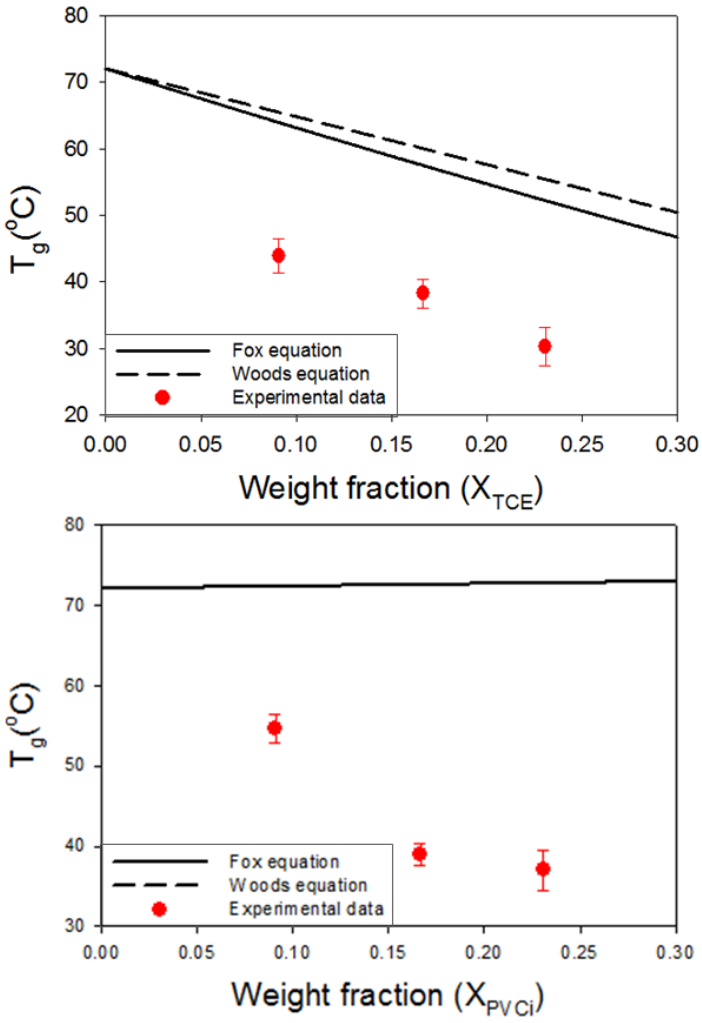

Figure 4. 20 T_g of Epoxy with Various Contents of Cross-Linked TCE (Top) and PVCi (Bottom) Polymer between Theoretical Value and Experimental Data.

In Figure 4.20, T_g by experiment is very different from the T_g by either Fox equation or Wood equation. T_g of polymer blends were quite lower. Especially for epoxy with cross-linked PVCi polymer, the equation curve predicted an increasing trend with more PVCi added; however, the experiment displayed an opposite tendency that was more PVCi could shift T_g to much lower. It is well known that T_g of epoxy polymer blends varies for reasons, like conversion of the curing reaction or compositions of the

blends [145-147]. The result above suggested that T_g of this blend system was not only effected by the compositions of the blends. More importantly, the photocycloaddition of TCE or PVCi reduced the curing degree of epoxy significantly. The curing mechanism of cross-linking reaction in neat epoxy was the nucleophilic amine on DETA attacked the carbon atom on ethylene oxide ring to form C-N bond meanwhile C-O bond was broken [176]. TCE or PVCi introduced additional carbonyl group to the blends, which might influence the cross-linking process of epoxy by increasing the resin to hardener ratio due to the possible interactions between carbonyl group and amine. However, these carbonyl groups on cinnamates were not preferred by amine, because conjugated carbonyl structure made it much less inactive compared to the ethylene oxide ring. In addition, the low cross-linking of epoxy could be caused by the network formation by cycloaddition of cinnamates which restrained the motion and rotation of resin and hardener monomers during curing process.

To investigate the effect of curing temperature on the T_g of epoxy and polymer blends, the samples were cured in vacuum at 60 ℃ for 24 hr. The corresponding T_g is shown in Figure 4.21. It was found that T_g was shifted to higher temperature for neat epoxy and polymer blends, indicating an improvement on curing at higher curing temperature. To better compare, the T_g of the samples cured at different temperature were summarized in Table 4.3. The difference between partially and fully cured samples was large for epoxy/polymer blends, especially for epoxy with TCE polymer. The network formation by dimerization of cinnamoyl function groups sterically hindered the network growth of epoxy, leaving quite a few epoxy resins and hardeners unreacted. The mobility of resin and hardener molecules was increased by heating up the system, facilitating the

formation of cross-linking. Therefore the T_g was increased significantly for the blend systems.

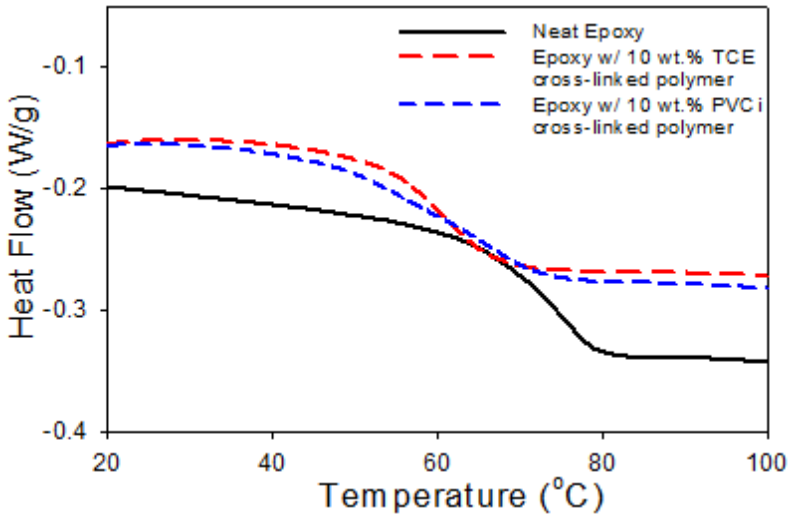

Figure 4. 21 DSC Curves for the Samples Cured at 60 ℃.

Table 4. 4 Comparison of T_g of Samples Cured at Different Temperatures.

Polymer	T_g(cured at 25°C), °C	T_g(cured at 60 °C), °C	Difference, °C
Neat epoxy	73.1±2.1	75.7±1.4	2.6
Epoxy w/ TCE polymer	43.9±2.5	61.3±1.7	17.4
Epoxy w/ PVCi polymer	54.7±1.8	64.7±2.9	10.0

Validation of Molecular Dynamics (MD) Simulation

The experimental work on T_g was further used to validate the molecular dynamics (MD) simulation work. MD simulation was conducted by Dr. A. Chattopadhyay's group. For MD simulation based on all-atom force field, atomistic molecular structures of each component in an objective system should be defined. Molecular structures of DGEBF (digycidylether of bisphenol F, DGEBPF) and DETA

(diethylenetriamine, DETA) are used to construct neat epoxy unit cell for MD simulation. A well-mixed epoxy-based system is guaranteed through the distribution of all the molecules randomly in each unit cell without overlap. The number of molecules are determined by the weight ratio 100:27 (DGEBF:DETA) which is used for making experimental samples in this study. The weight of TCE is 10% of the total weight of the neat epoxy unit cell. The force field MMFF, which is derived from computational data based on ab initio calculation, can accurately reproduce experimental results in chemical research. Based on MMFF, topologies and force field parameters of all the molecules used in MD simulations are generated by a web-based molecular structure generator. The MMFF force field is used in conjunction to LAMMPS, which has versatile features such as bond breaking/formation, unit cell deformation, and the ability to create/delete atoms. In the simulation, epoxy resin and hardener generate covalent bonds stochastically when the distance between active sites of epoxy resin and hardener is less than a certain distance; in this space two active sites can share their electrons to make potential energy stable. Details of the curing process are mentioned in the beginning of 4.1.2. Figure 4.22 shows a three dimensional visualization of DEGBF/DETA cross-linked systems. In Figure 4.22(a) the red dotted lines indicate that activated carbon atoms and activated nitrogen atoms react to generate a C-N covalent bond. DETA has three nitrogen atoms and can generate five C-N covalent bonds, because both end nitrogen atoms have two active sties and centered nitrogen atom has one active site. In addition to the C-N covalent bond between DGEBF and DETA, a photo-induced C-C covalent bond on cyclobutane produced from dimerization of C=C bonds of TCE monomers is considered. The photo-induced cross-linking degree is fixed at 40%, as investigated in Oya et al.[184].

In this simulation work, cross-linking degree means the extent of epoxy curing. In order to quantify cross-linking degree in MD simulation, the ratio of generated covalent bonds to total active sites of the system is defined. The schematic illustration of cross-linking degree is displayed in Figure 4.23 (DGEBF is in blue with active sites in red; DETA is in red with active sites in blue). For example, 0% cross-linking degree means there is no C-N covalent bond formation between DGEBF and DETA; when cross-linking degree is 50%, there are 2.5 out of 5 active sites on average on DETA participate in the epoxy curing reaction; 100% cross-linking degree indicates all the active sites are reacted between DGEBF and DETA.

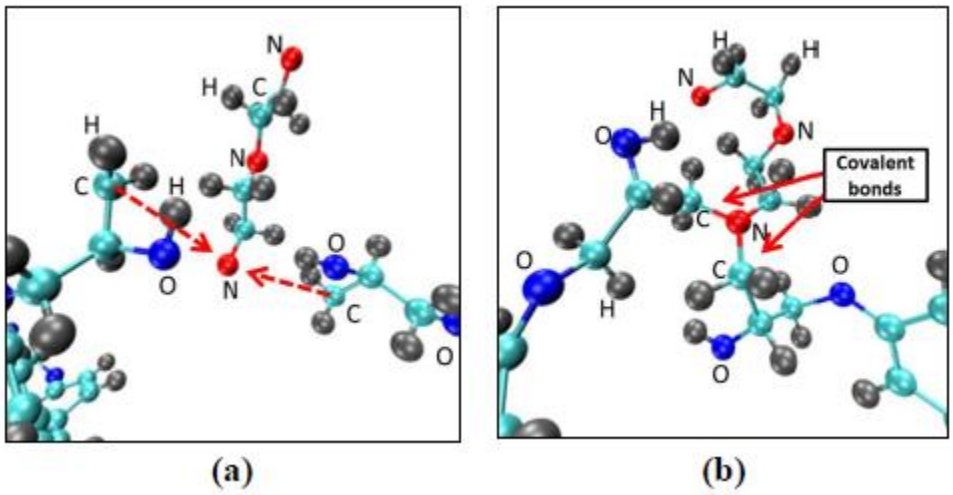

Figure 4. 22 Schematic of Molecular Structure before and after Covalent Bond Generation; Grey, Cyan, Blue and Red Sphere Represent Hydrogen, Carbon, Oxygen, and Nitrogen, Respectively. It Shows That Nitrogen Make Two Covalent Bonds with Two DGEBFs.

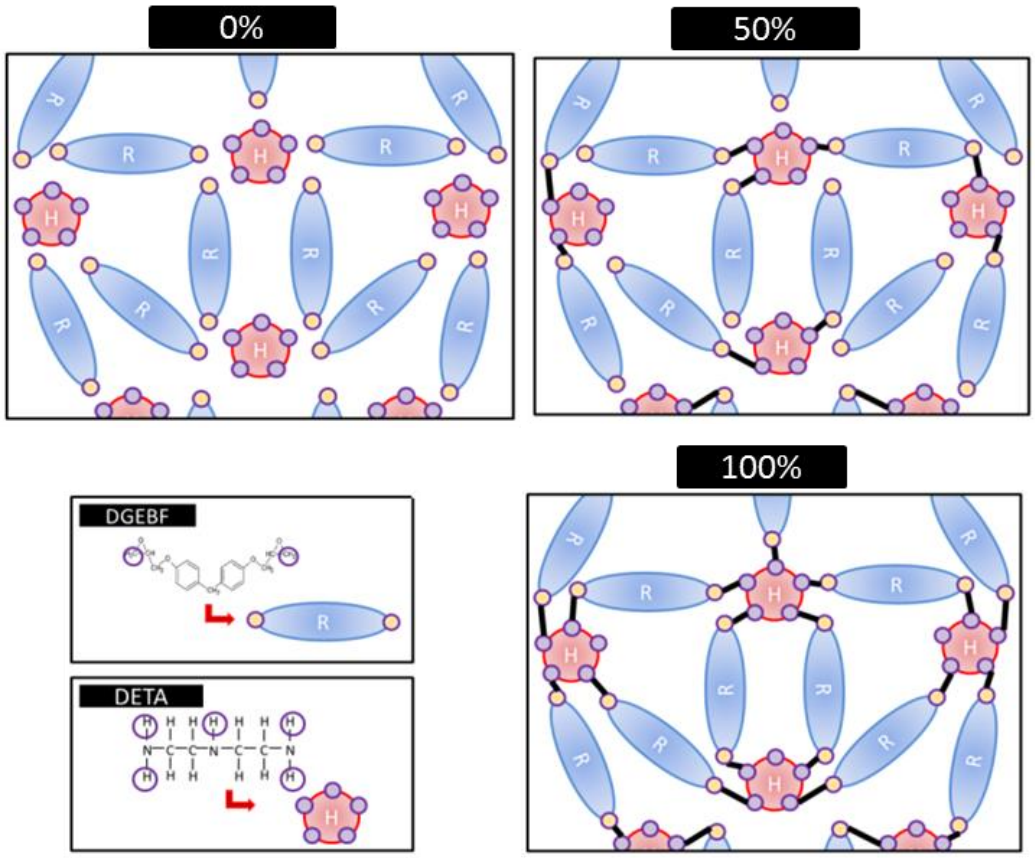

Figure 4. 23 Schematic Illustration of Active Sites and Cross-Linking Degree.

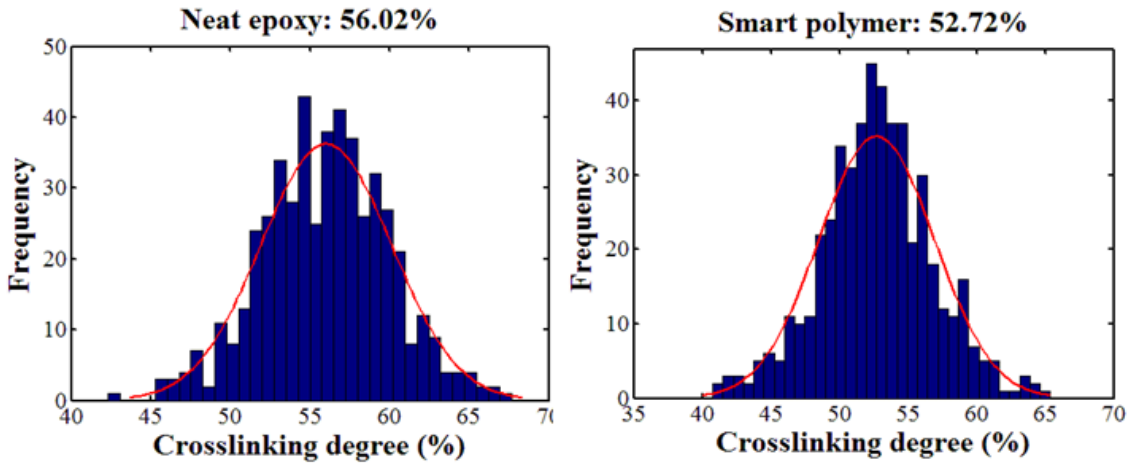

Figure 4. 24 Most Likely Cross-Linking Degrees of Neat Epoxy (a) and Smart Polymer (b); Red Solid Lines are Fitted Normal Distributions.

For the estimation of cross-linking degree of epoxy, the methodology comprises the following three steps: i) construct multiple unit cells with stochastic initial location of molecules, ii) generate numerical C-N covalent bonds for every unit cell, and iii) find average values of the cross-linking degree of all the unit cells. In this work 500 unit cells are constructed and C-N covalent bonds are generated for all the unit cells using the numerical curing process which was introduced in the previous section. After obtaining 500 cross-linking degree data a frequency distribution is plotted as seen in Figure 4.24. Two normal-like distributions are obtained from the histograms for both neat epoxy (mean is 56% and standard deviation is 4.1%) and smart polymer (mean is 52.7% and standard deviation is 4.2%). Calculated average cross-linking degrees are 56% for neat epoxy and 52.7% for smart polymer from a frequency distribution data, which are considered the most likely cross-linking degrees in the simulation work.

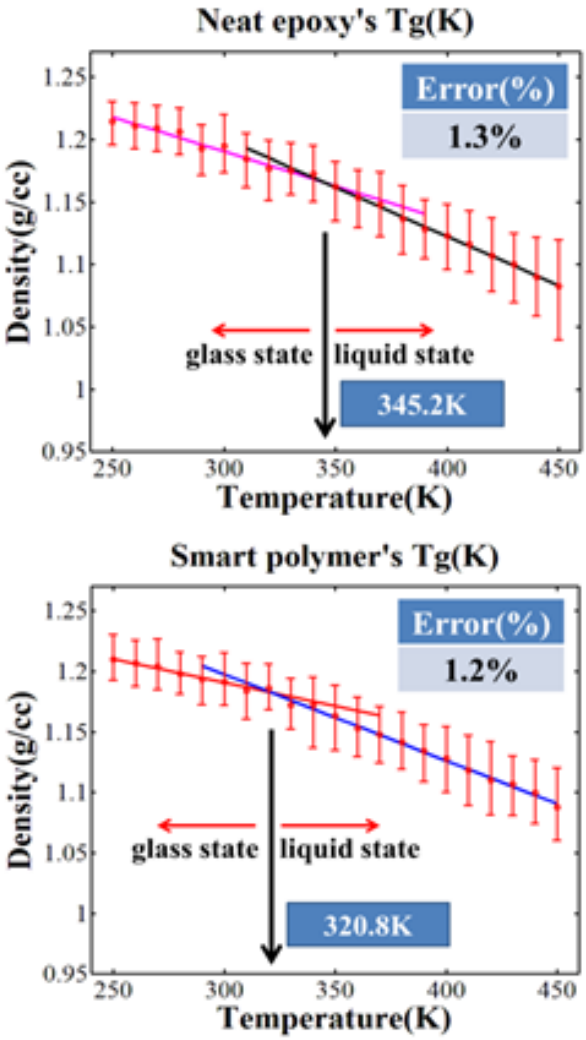

Figure 4. 25 T_g of Cross-Linked Epoxy Estimated by Relation of Density and Temperature during Simulation (Smart Polymer Represented Epoxy w/ 10 wt. % TCE Polymer).

Based on the most likely cross-linking degrees, T_gs have been investigated by calculating densities at temperatures ranging from 250K to 450K. After generating covalent bonds, the system becomes unstable due to newly generated bonds. In order to ensure the stability of the system before initiating MD simulation with different temperatures, additional energy minimization and NPT ensemble simulation (250K and 1atm for 200ps) are required. With stabilized system, a stepwise heating simulation is

performed by starting with equilibrated system (250K and 1atm) followed by intervals of 10K. For each temperature, NPT ensemble simulation has been conducted for 100ps. Comparing to experimental heating rate, 10K/100ps is very high; however it is used due to the inherent time scale limitation of MD simulation. To bridge the discrepancy between experiment and simulation, an assumption made in this study is that once the system is equilibrated computationally, it will stay at the same state without any significant change and 100ps was enough time to equilibrate the system. Densities at each temperature are calculated using time average of densities around equilibration state due to fluctuation behavior of molecules. Since the epoxy-based systems are amorphous polymer, there is a transition in density as the temperature varies. The T_g was estimated from the relation of density–temperature during cooling-down simulation by locating the intersection of two linearly fitted lines in the two regions: glass and liquid state region. Through this procedure, T_gs of neat epoxy and smart polymer are determined to be 345.2K and 320.8K, respectively, which was in good agreement with experimental T_g (346.3K, 317.0K), as displayed in Figure 4.25. To study the effect of cross-linking on the T_g, a relationship between T_g and cross-linking degree was established as shown in Figure 4.26. This relationship was established from the simulations which were run at different curing temperatures. From the plot, it is obvious to see that higher cross-linking degree leads to a higher T_g.

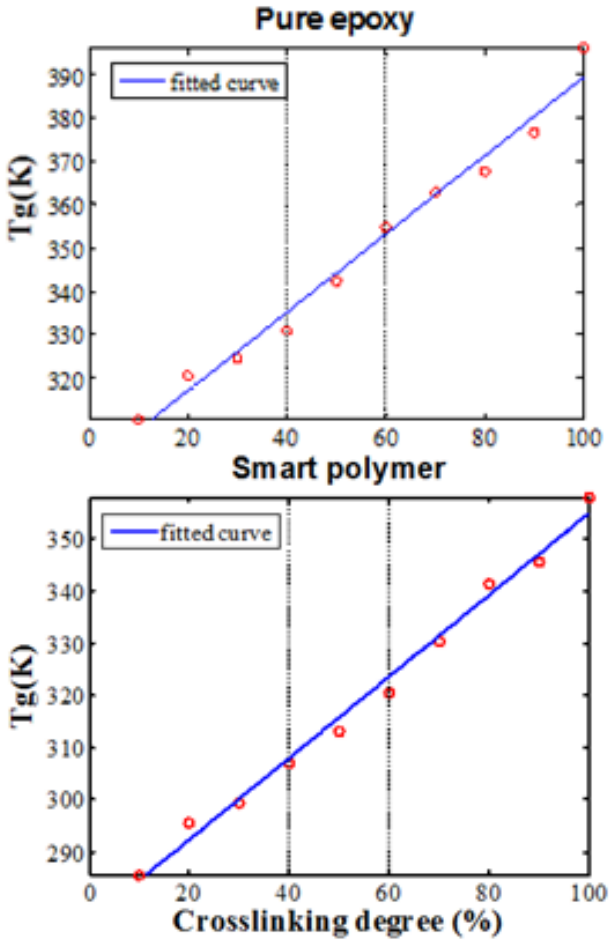

Figure 4. 26 Correlation between T_g and Cross-linking Degree Conducted from MD Simulation.

Cross-Link Density Analysis

By no means can the conversion of monomer reach 100% in any polymerization system. The polymer always contains a few even a considerable amount of unreacted monomers, which is related to the initial concentration of the monomer, the initiator and the reaction condition. Cross-link density of the polymer is important structural parameter because it can influence the physical properties of polymers. Epoxy resin monomer is cross-linked by a hardener. The cross-link density of epoxy can be changed by adjusting

the composition ratio of resin monomer, hardener and control of the cure conditions In this section, elastic modulus data above the glass transition temperatures (in the rubbery plateau region) from DMA was used to estimate the cross-link densities of epoxy networks. The effect on the cross-link density from the addition of cyclobutane-based cross-linked polymer was investigated. According to the theory of rubber elasticity, the equilibrium elastic modulus is provided via the equation 4.5 below [192],

$$\rho = \frac{E'}{3RT} \tag{4.5}$$

where ρ is the cross-link density expressed in moles of elastically effective network chains per cubic centimeter of sample, E' the rubbery plateau modulus , R the gas constant and T the absolute temperature at which the experimental modulus is determined.

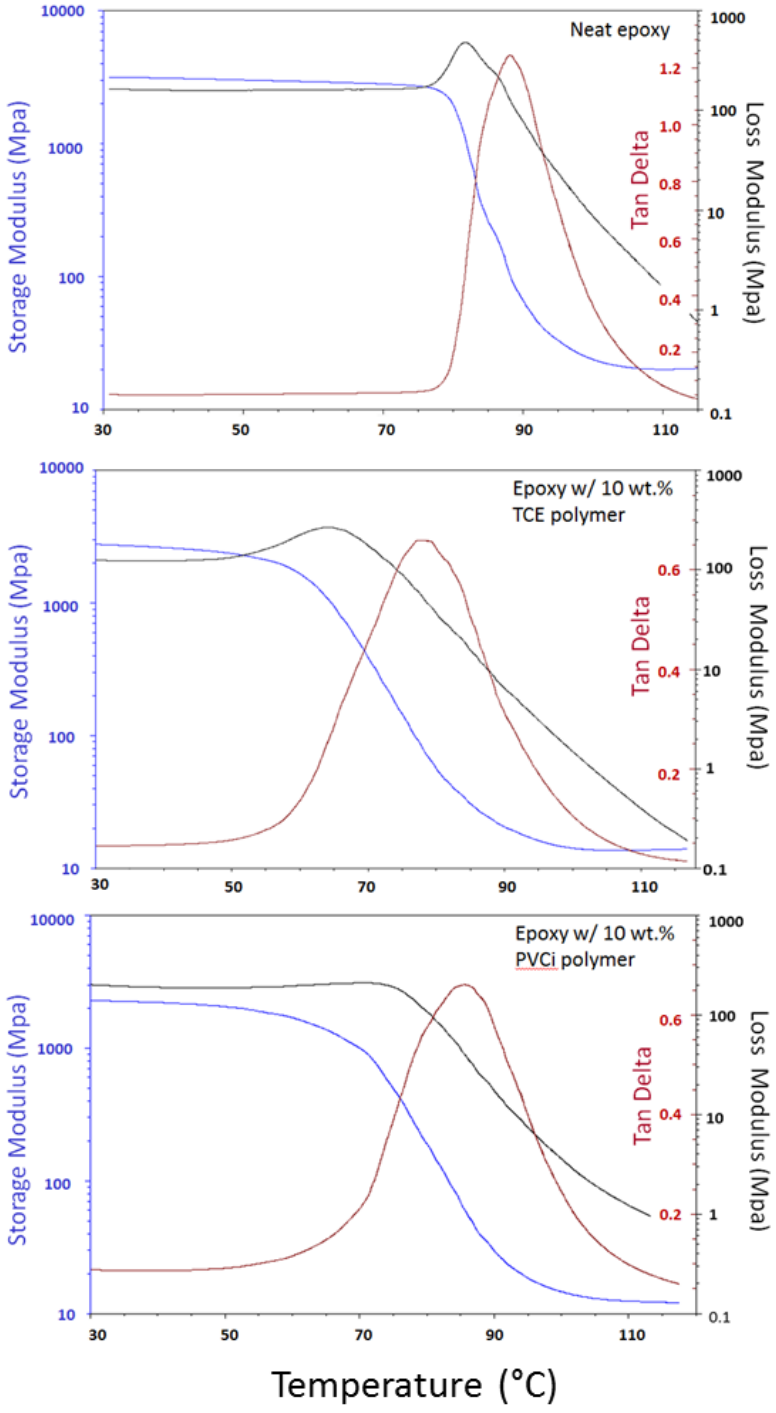

Figure 4. 27 DMA Curve for the Specimens of Neat Epoxy and Polymer Blends.

Experiments were performed in a tension mode with multi-frequency/strain on a TA Instruments Q800. Thin films of polymeric blend were mounted onto the tension clamp and the temperature was ramped from 25 to 120 ℃ at a heating rate of 5 ℃ /min. The frequency was 1Hz under amplitude control. The strain amplitude was set at 25 μm. DMA analysis can determine the storage modulus, loss moduli and the tan δ (E"/E´) as a function of temperature (Figure 4.27). The peak value of the tan δ curve can accurately described the glass transition midpoint and was taken as the T_g. They had well defined transition regions and rubbery plateau regions. The storage modulus changed only slightly with temperature in the rubbery plateau region which was considered as constant up to the chemical degradation temperature. Comparison between T_g obtained by DSC and DMA is summarized in Table 4.5. T_g of epoxy conducted by DMA was higher than the other two blends as expected. The experimental cross-link densities calculated from these elastic storage moduli are summarized in Figure 4.28. Cross-link density for neat epoxy was higher than the other two polymer blends systems, since it had higher glass transition temperature which always indicated a higher cross-linking degree. The interactions between cyclobutane polymer and epoxy network reduced the cross-link density of the blended systems because the network growth of the epoxy was considered to be encumbered by the cross-linking of cinnamoyl groups under photoirradiation. The density for the epoxy w/ PVCi blend system was much lower than the epoxy w/ TCE blend system, though the T_g for epoxy w/ PVCi was higher. This might be contributed from nature of cross-linked TCE and PVCi polymer themselves.

Table 4. 5 Comparison of T_g Determined by DSC and DMA

Polymer	T_g(DSC), °C	T_g(DMA), °C
Neat epoxy	75.6 ± 1.4	86.2 ± 2.2
Epoxy w/ TCE polymer	61.3 ± 1.7	79.8 ± 1.2
Epoxy w/ PVCi polymer	64.7 ± 2.9	84.0 ±2.1

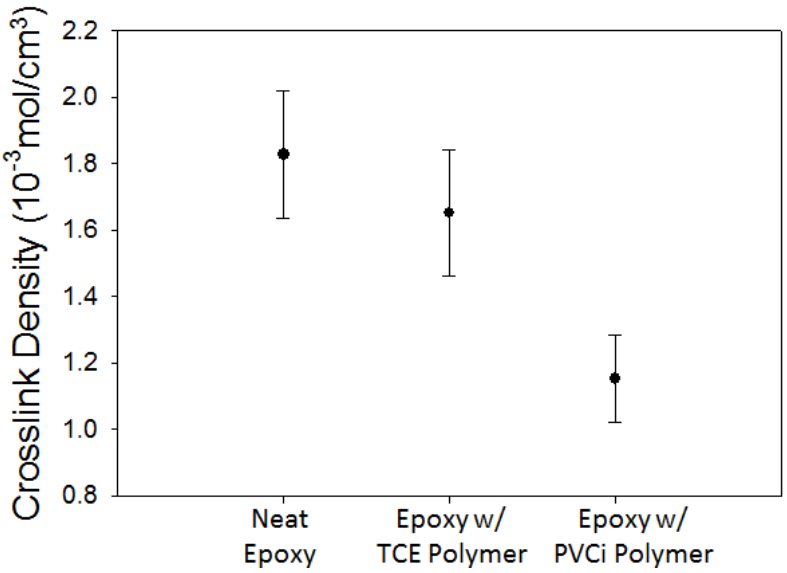

Figure 4. 28 Cross-Link Density for Neat Epoxy and Polymer Blends.

Thermal Stability

Thermogravimetric analysis (TGA) monitors the amount and rate of change in the mass of a sample as a function of temperature or time as a sample is heated at a programmed rate in a controlled atmosphere. The measurements are used primarily to determine the thermal stabilities of materials as well as their compositional properties. In this work, TGA was used for characterizing the thermal stability of cross-linked TCE and PVCi polymer and polymer blends. The information obtained can tell us whether the

polymer blends will be useful for high temperature application or not. Due to the sensitivity of TGA to experimental conditions, it is required that all the thermal stability analysis of sample of interest can only be complete under identical conditions. Weight loss due to thermal degradation is an irreversible process, which is most related to oxidation through the interaction between the molecular bonds of a polymer and oxygen molecules [193-195]. Besides oxidation, polymers can be thermally degraded by depolymerisation, random chain scission, side-group elimination and so on [196, 197]. Since we run all the TGA measurements under nitrogen in our experiment, thermal degradation by oxidation was not considered. The experiment was carried out using a TA Instruments (TGA Q500 machine). All the samples were heated from 30 to 600 ℃ at a heating rate of 10 ℃/min. The thermal weight loss curve and differential thermal gravimetry (DTG) curves as a function of temperature for cross-linked TCE and PVCi polymer are shown in Figure 4.29. The peak of the DTG indicated the point of greatest rate of change on the weight loss curve. Obviously, cross-linked TCE polymer showed a higher initial decomposition temperature which started from 250 ℃ and completed at 430 ℃. Thermal decomposition of cross-linked PVCi polymer took place at 100 ℃. From DTG curve, the major degradation process for TCE polymer appeared at 372 ℃ (60.18% wt. loss). It is observed that cross-linked PVCi polymer had two subsequent major decomposition steps separated by a transition region, occurring at 300 ℃ (30.97% wt. loss) and 420 ℃ (86.56% wt. loss). One can see that the main mass loss occurs at temperature region from 270 to 330 ℃. It indicated that the cinnamate groups were mainly broken from the main chain at this stage, and the detached cinnamates groups

were evaporated, resulting in the major weight loss [198]. In general, cross-linked TCE polymer and PVCi polymer both showed good thermal stability.

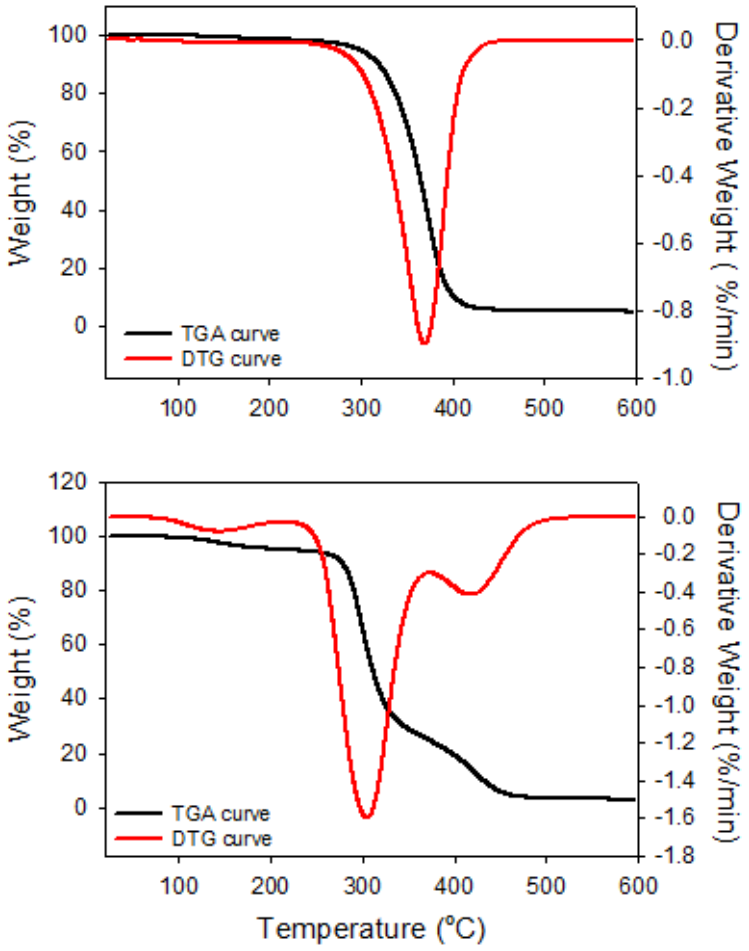

Figure 4. 29 TGA and DTG Curves of Cross-Linked (Top) TCE and (Bottom) PVCi Polymer.

TGA curves of neat epoxy and polymer blends are displayed in Figure 4.30. Single step decomposition was observed in all the samples. Thermal decomposition of epoxy w/ TCE took place firstly. From DTG curve, the value of derivative for epoxy with cross-linked PVCi polymer was higher than epoxy and epoxy with cross-linked TCE polymer. The major degradation process for these three types of samples all appeared at

around 350 ℃ (Epoxy: 347 ℃, 31.10% wt. loss; epoxy w/ TCE: 357 ℃, 47.94% wt. loss; epoxy w/PVCi: 357 ℃, 47.61% wt. loss), indicating the addition of polymer increased the rate of degradation of epoxy, which might be attributed to the weaker cross-linking of epoxy.

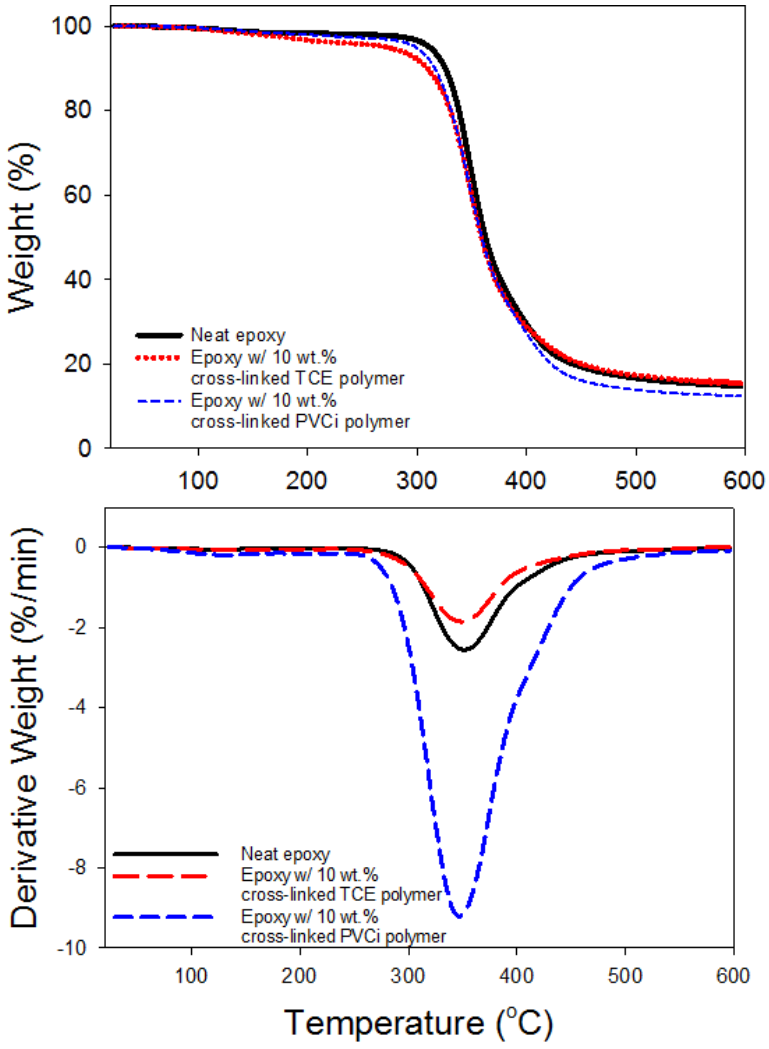

Figure 4. 30 (Top) TGA and the (Bottom) DTG of the Neat Epoxy and Polymer Blends.

Stress-Strain Curve

In compression test, the compressive stress-strain behavior of these systems was obtained on MTS servo hydraulic test system. All the compression tests were run in displacement control in longitudinal direction at loading rate of 1 mm/min. Representative stress-strain curves of neat epoxy and epoxy and cyclobutane-based cross-linked polymer blends were determined in compression tests, as shown in Figure 4.31. For the compression test, the strain (%) is calculated from the ratio of displacement to the initial dimension. All these three systems displayed a qualitatively similar stress-strain behavior. The curves exhibited an initial linear elastic response followed by yielding. With a slow drop-off on stress, a plateau region was observed for a wide range of strains. The Young's modulus for neat epoxy and polymer blends) was determined by a linear regression to the slope of the stress-strain curve in the initial linear elastic region (Table 4.6). The addition of cross-linked TCE and PVCi polymer into epoxy decreased the mechanical properties of the epoxy systems due to the lower cross-linking degree. The neat epoxy had the higher yield stress than the other two systems, revealing that the ability of epoxy system to resisting damage declined with the addition of cross-linked TCE or PVCi polymer, which brought in advantages in the application of a crack sensor, because the polymer blends could be more sensitive and easier to deform under stress.

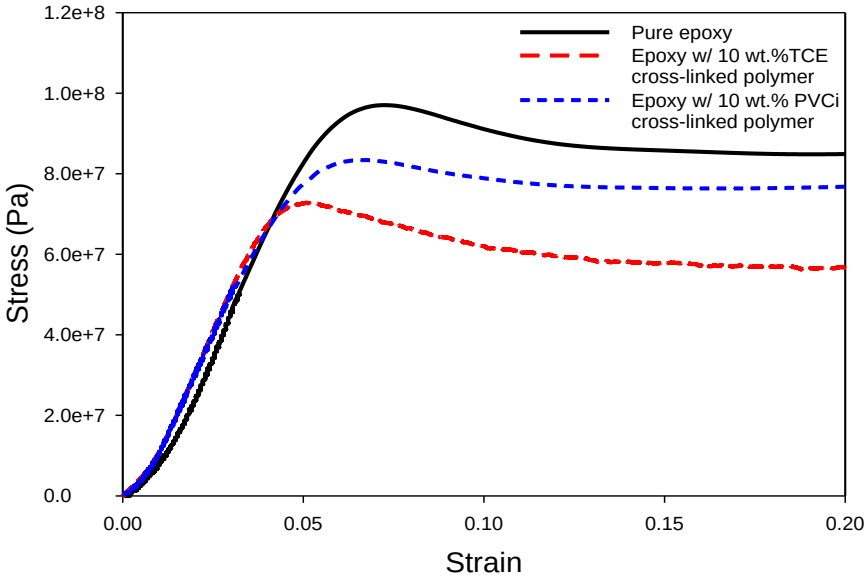

Figure 4. 31 Compressive Stress-Strain Curves for the Pure Epoxy and Epoxy w/ 10 wt.% Cross-Linked TCE and PVCi Polymers Dispersed in the Matrix.

Table 4. 6 Young's Modulus for Neat Epoxy and Polymer Blends

Polymer	Young's modulus, Gpa
Neat epoxy	2.2 ±0.1
Epoxy w/ TCE polymer	1.9 ± 0.1
Epoxy w/ PVCi polymer	2.0 ±0.1

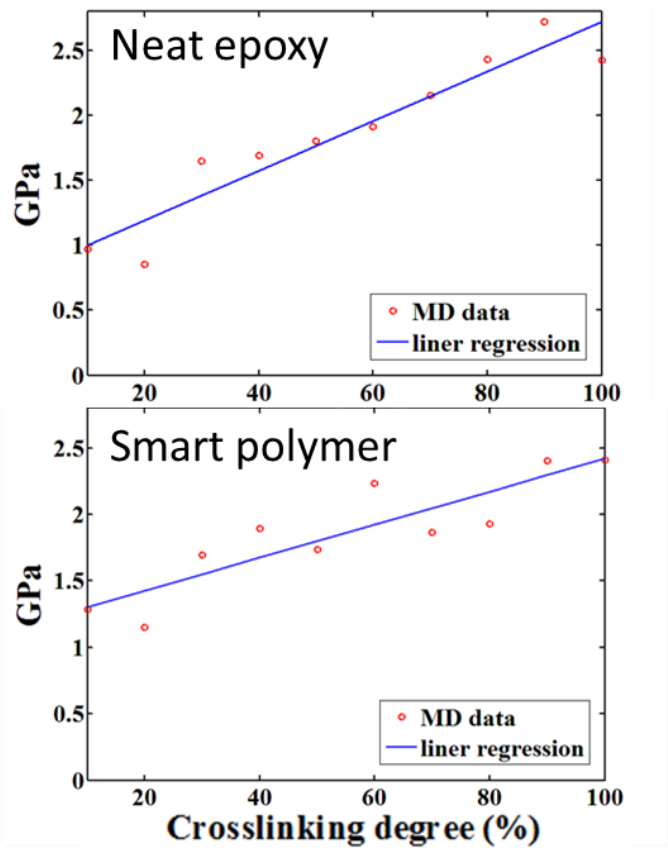

Figure 4. 32 Correlation between Young's Modulus and Cross-Linking Degree (%) Conducted by MD Simulation.

The mechanical properties were related to the network structure, which was expressed by the degree of cross-linking reaction. In Figure 4.32, the Young's modulus from simulation displays a linear relationship with the cross-linking degree %. As cross-linking degree % increased, the young's modulus increased. The slope of the fitted line for neat epoxy was a larger than the smart polymer, indicating that the addition of the TCE cross-linked polymer reduced the Young's modulus.

4.1.3 Fluorescence Response by Mechanically Activation

Compression Test

The goal for the application of cyclobutane-based polymer in solid state was to demonstrate mechanochemical cleavage of a covalent bond, and further to investigate the use of these cyclobutane polymers blended with epoxy as stress/strain or damage sensors by visual detection. Epoxy material and its composite are ubiquitous in everyday life. Therefore, it is very useful to detect the location of damage before an epoxy product undergoes failure. Here, we applied a simple and direct method for detecting mechanochemical reactions with UV microscopy, because cyclobutane-based cross-linked polymers of tricinnamates were reported to generate fluorescence upon the cleavage of cyclobutane ring.

Cyclobutane, a four-membered ring molecule is known for its highly strained structure largely attributed to angle strain and torsional strain [199]. Therefore, the cleavage of the C-C bonds of cyclobutane upon cracking was relatively easy compared to other bonds such as C–O and other C–Cs in the polymer structure. If cyclobutane is applied as a cross-linker in the cross-linked polymer, the mechanochemical cycloreversion of cyclobutane is the major reaction since it has lower bond strength. When the system was blended with epoxy, the C-C bond on cyclobutane is much weaker than the bond in epoxy.

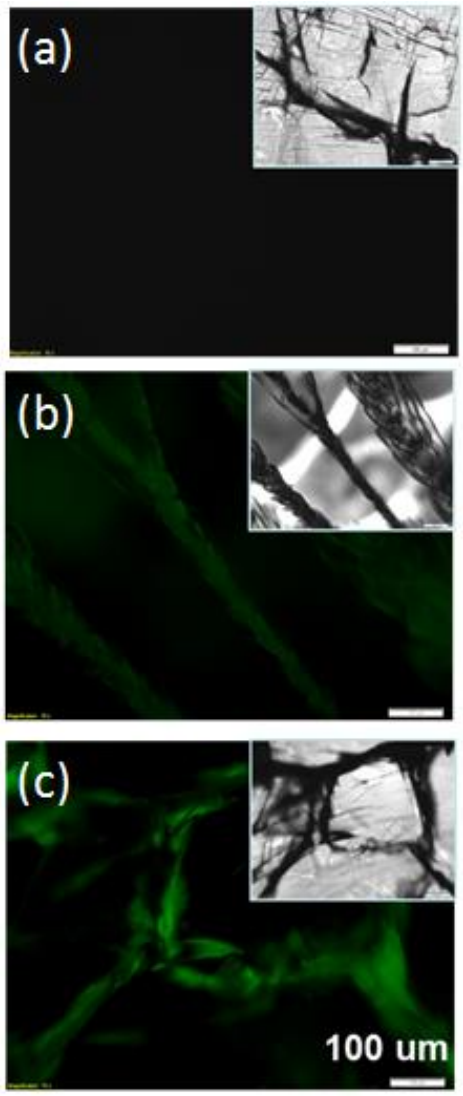

Figure 4. 33 Microscopic Images of Cracks Generated by Hammer Hit on (a) a Clean Polystyrene Substrate, a Polystyrene Substrate Coated with Cross-Linked (b)TCE and (c) PVCi Polymer under a UV Light. The Insets were the Corresponding Images under a White Light.

The fluorescence response was firstly confirmed by coating cross-linked TCE polymer film on a polystyrene substrate. The cracks were generated by external force and observed using UV microscopy, as shown in Figure 4.33. Under the microscope with white light, the cracks were observed both on the polystyrene and polystyrene with

coating. But the fluorescent signal was only detected on the polystyrene coated with cross-linked TCE polymer exposed to UV light. Furthermore, cross-linked PVCi polymer was coated on the polystyrene substrate. The fluorescence emission was observed along the crack as well. The results indicated the mechanochemical cleavage of cyclobutane occurred along the crack propagation and induced the fluorescence generation.

When the cracks were generated by external force on the polymer blends with different amounts of cross-linked TCE polymer, fluorescence emission from the cracks was clearly observed under UV and white light both, as shown in Figure 4.34. The fluorescent signal was further augmented with increasing amount of cross-linked TCE polymer blended with epoxy. No fluorescence emission was found on neat epoxy at the same experimental condition. From the images, epoxy with 10 wt. % cross-linked TCE polymer gave strong enough fluorescent emission to detect the damage. Thus, the content of 10 wt. % was used for the following fluorescent tests.

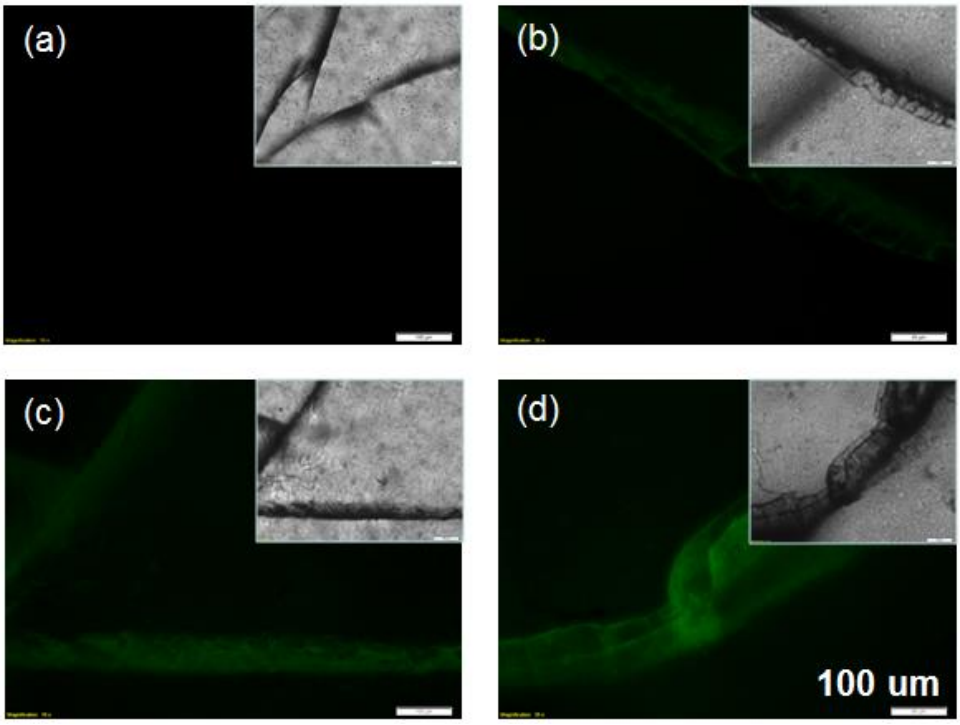

Figure 4. 34 Microscopic Images of Fluorescence Emission along Cracks Generated by Hammer Hit on Polymer Blends (a) without (b) with 10 wt.% (c) 30 wt. % (d) 50 wt.% Cross-Linked TCE Polymer. The Insets were the Corresponding Images under White Light.

Neat epoxy and polymer blends were compressed to different strains respectively. No fluorescence was detected on neat epoxy. The evolution of induced fluorescence emission on epoxy is shown in Figure 4.35. For both polymer blends, there was not obvious fluorescence observed before the yield point was reached; right after the yield point, the microcracks started to form and could be observed under UV by fluorescence emission. Those cracks could not been clearly observed under white light, indicating that the fluorescence emission could provide a higher sensitivity and easier detection for the location of cracks, especially cracks at micro scale. It is also noticed that fluorescence emission along the crack intensified with strain after the yield point.

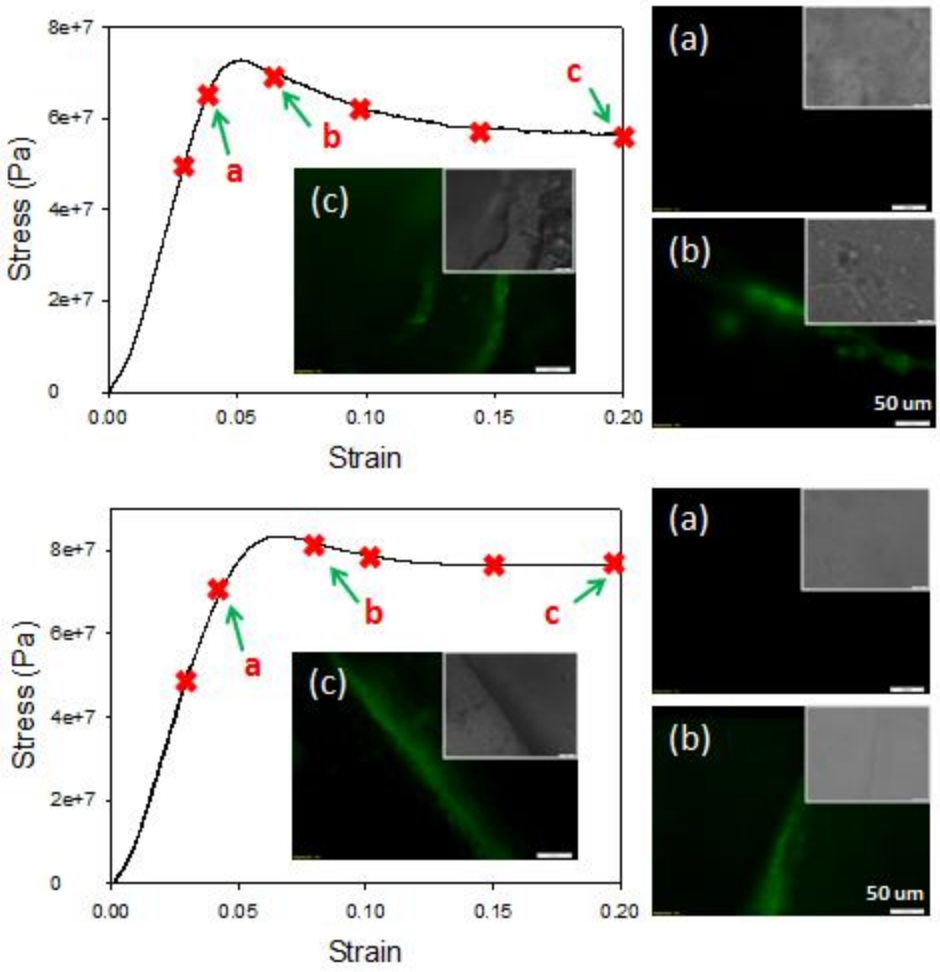

Figure 4. 35 Microscopic Images of Fluorescence Emission in Response to Different Strains of Epoxy w/ 10 wt.% Cross-Linked TCE (Top) and PVCi (Bottom) Polymer Blends.

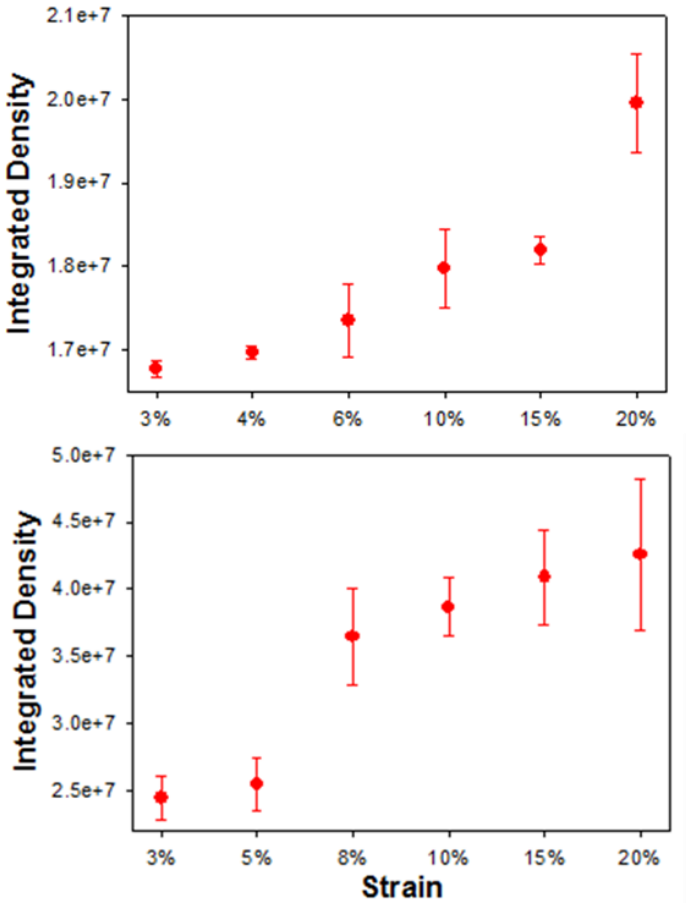

Figure 4. 36 Integrated Density of Fluorescence Emission in Response to Different Strains of Epoxy w/ 10 wt. % Cross-Linked TCE (Top) and PVCi (Bottom) Polymer Blends.

In order to further explore the relationship between the strains and their corresponding fluorescence response, ten fluorescent micrographs were processed by ImageJ and the average fluorescence densities were calculated. The density change as a function of strain was plotted in Figure 4.36. As expected, the densities increased with the accumulation of strain, which indicates that the more cleavages of cyclobutane were activated as strained increased.

Fatigue Test

Glass fibers are often incorporated into a polymeric matrix to enhance its mechanical and thermal properties. Glass fiber reinforced composites take advantages of both the properties of glass fiber and the polymeric matrix. Besides, the composite materials have a combination of properties that cannot be achieved by either glass fiber or polymeric matrix alone. Embedded glass fibers are the main load-carrying constituent, protected by the polymeric matrix from chemical degradation and mechanical abrasion. They offer a number of advantages such as the high tensile strength and high chemical resistance [200-203]. Therefore, the glass fiber reinforced epoxy composites, due to their high specific strength and stiffness at the low cost, are widely used in various structural applications where they are subjected to constant and variable amplitude fatigue loads in service, such as aeronautic, naval and construction [168-172].

The fluorescence response on the glass fiber reinforced composite (GFRC) was first confirmed by the damage applied with a metal tool. A circle was marked and the damage was made by the metal tool punch on one side of the single sheet within the circle, as seen in Figure 4.37 (right). The images within the circle before and after the damage were collected and compared. Obviously, the fluorescence was observed along the fiber after damage applied, as seen in Figure 4.37 (left).

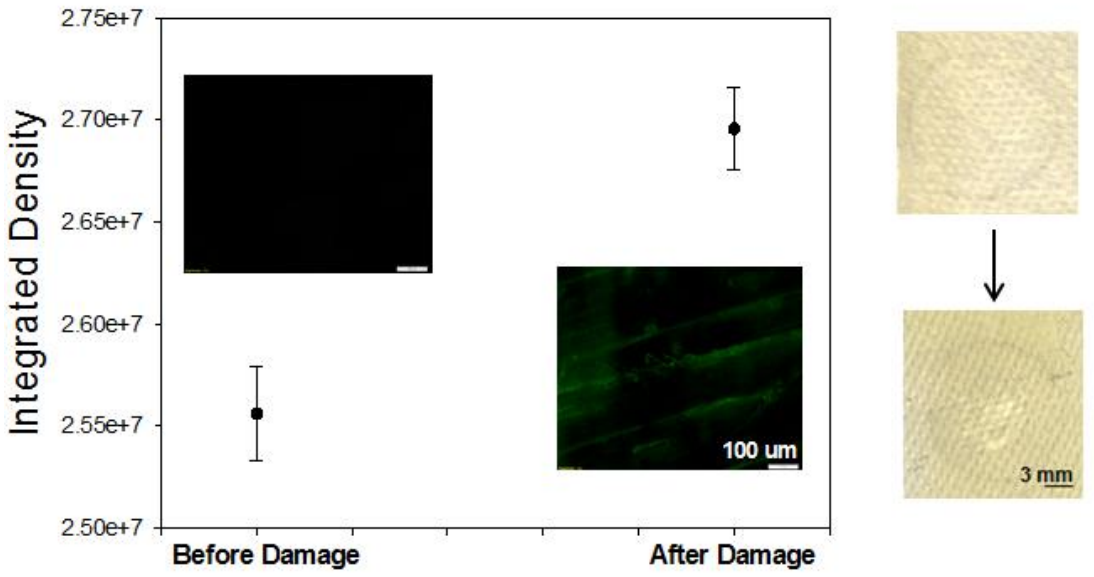

Figure 4. 37 (Left) Fluorescence Density of Fiberglass Epoxy Composite with 10% TCE before and after Damage was Applied. (Right) GFRC Specimen under a White Light.

The tensile fatigue failure in composite materials is a common failure mode in most of the GFRC. A uniaxial tensile fatigue test was performed on a GFRC sheet. The specimen loaded and cycled in a load-controlled mode at stress ratio (R), σ min / σ max = 0.1 on a uniaxial fatigue frame operating with a sinusoidal waveform at a frequency of 2 Hz. Maximum stress (1000 N) and minimum stress (100 N) was constant for each cycle of a test. After a certain number of load cycles, the test was paused and the specimen was dismounted and photographed under white light and UV microscope. Then the specimen was remounted and the fatigue cycles resumed. In order to monitor the crack growth on the GFRC specimen, SEM characterization of the specimen was carried out. Figure 4.38 shows the matrix cracks, matrix debonding and fiber breakage on the GFRP specimen surface. Figure 4.38 (top) the shows micro-cracks on the matrix after 500 cycles. The exposure of glass fibers after 1,000 cycles in Figure 4.38 (middle) shows interface

debonding. These exposed glass fibers tend to fracture under cyclic tensile force. After 1350 fatigue cycles, more breakage of glass fibers was observed as well as matrix cracks, causing a noticeable propagation along the longitudinal direction, as shown in Figure 4.38 (bottom). The corresponding macroscopic images are shown in Figure 4.38 (inset). With increasing fatigue cycles, the cracks developed in the 0 °direction and became visible. The higher the number of fatigue cycles, the more cracks formed. UV microscopic images of fluorescence emission at different fatigue stages are shown in Figure 4.39. The damages were first formed along the glass fibers at 0 ° direction. With cycles, the fluorescence emission became more obvious and the cracks along the glass fibers at 90 ° direction grew as well. Fluorescent micrographs at different fatigue cycles were processed through ImageJ and the average fluorescence densities were calculated. The corresponding fluorescence density change was plotted in Figure 4.40. As expected, the density intensified as cycles increased, indicating that there were more cyclobutane molecules cleaved into cinnamate molecules due to the weaker bond strength on the cyclobutane ring than the other bonds.

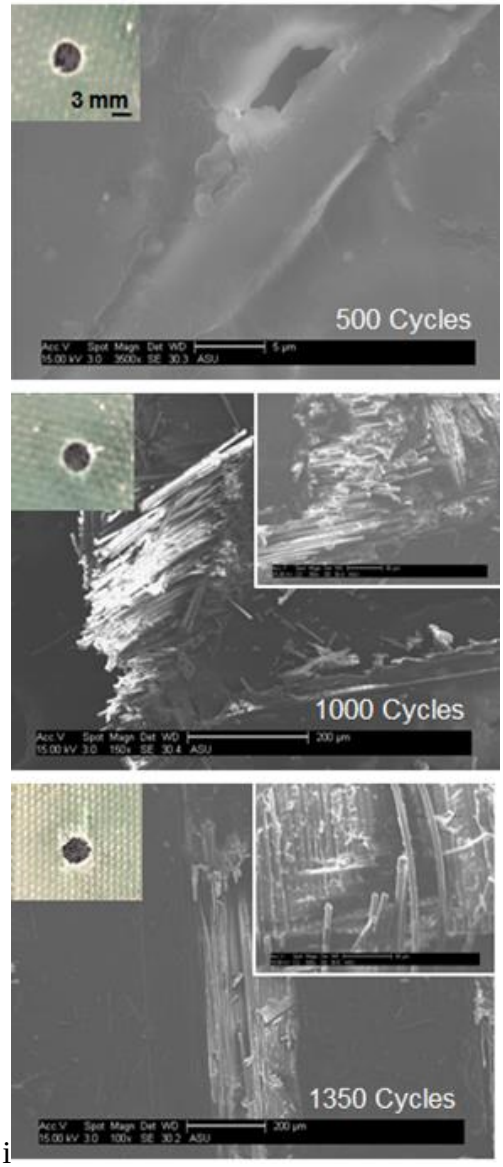

i

Figure 4. 38 SEM Micrographs of Glass Fiber Reinforced Epoxy Composite with 10% TCE at Different Fatigue Cycle Stages. Insets are the Images under White Light.

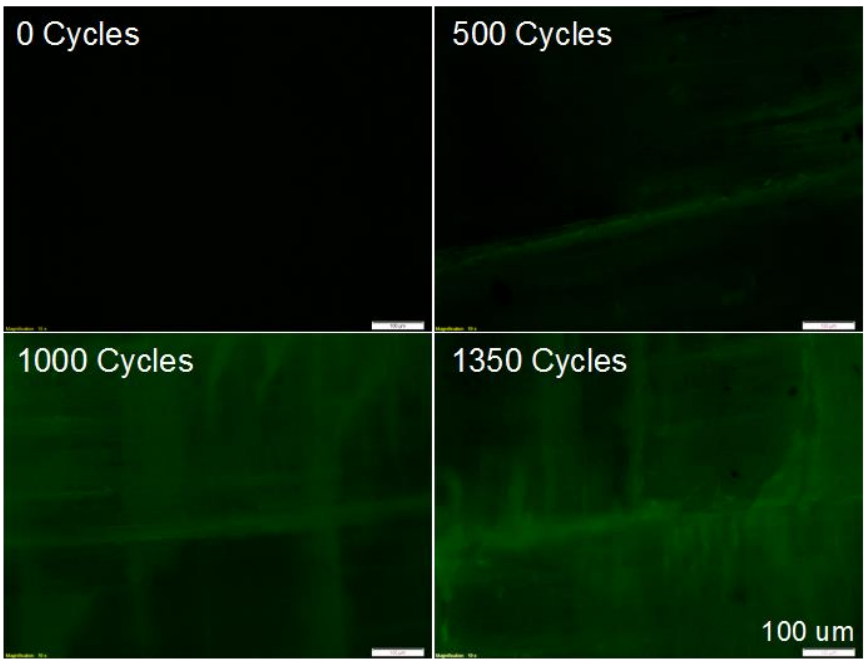

Figure 4. 39 Microscopic Images of Fluorescence Emission on GFRC in Response to Different Fatigue Cycle Stages.

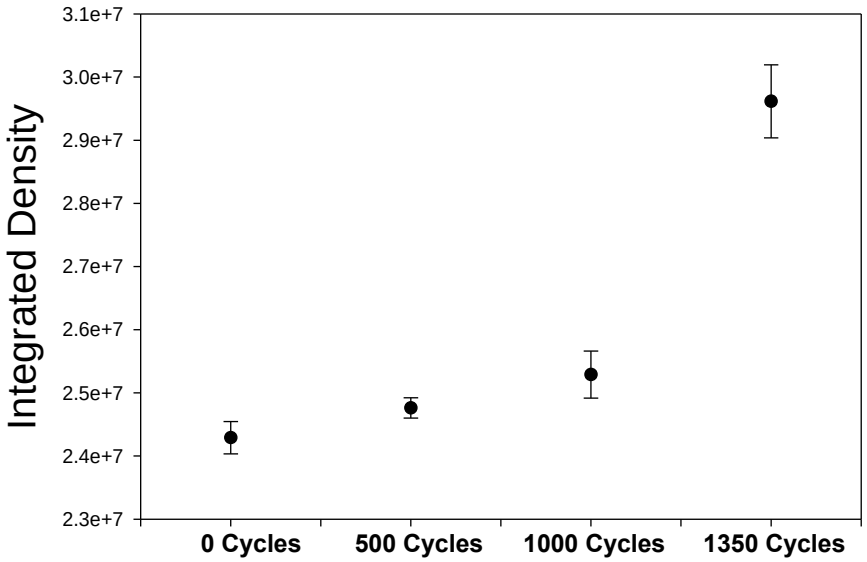

Figure 4. 40 Corresponding Fluorescence Density of Glass Epoxy Composite with 10% TCE at Different Fatigue Cycle Stages.

4.2 Cyclooctane-Based Polymers

4.2.1 Synthesis and Reaction Mechanisms

Similar to the mechanism of fluorescence emission from the cleavage of cyclobutane, the cyclooctane moiety can generated fluorescent emission upon the cleavage of cyclooctane due to the regeneration of anthracene. The use of anthracene is expected to allow for an earlier damage detection as the chemical exhibits over 10 times the absolute fluorescence quantum yield compared to that of cinnamates, due to the molecule containing three conjugated benzene rings [177]. Because of the superior quantum yield, an order of magnitude less individual mechanophore molecules are needed to break in cyclooctane to observe the same fluorescence that occurs with TCE or PVCi. Thus, earlier damage when only few molecules are broken is hypothesized to be observed. This high quantum yield also provides the possibility of detecting damage deep in the polymer matrix as well as the early damage precursor functionality, making the anthracene moiety more desirable to be used as a fluorescent sensor in practical applications. Also, it is reported that the longer conjugation system will bring the excitation/emission to longer wavelengths, generating the possibility for naked eye observation [178]. This functionality has been seen in that the maximum fluorescence emission wavelength is shifted from 495 nm for TCE to 568 nm for anthracene.

The synthesis of the cyclooctane-based polymer followed a method [177] described in Chapter 3. The first step was to produce di-anthracene by UV photoirradiation. The dimer was connected by two covalent bonds through [4+4] cycloaddition to form unusual butterfly shape, as displayed in Figure 4.41. The central

aromatic ring of the anthracene is most highly reactive compared to the other two aromatic rings. Since electrophilic substitution, such as the oxidation, occurs at the central positions readily, it is required that the dimerization of anthracene is performed under nitrogen atmosphere. The preference for destroying the aromaticity of the center ring than the one of the terminal ring can be explained by the aromatic stabilization energy. Destroying the aromaticity of the central ring can keep the aromaticity of the two terminal rings; while it only keeps one and a half ring if the dimerization occurs on one of the terminal rings. Anthracene is soluble in most organic solvents, while di-anthracene is not. So di-anthracene can be synthesized and purified by photoirradiation of anthracene solution and washed by a solvent. The next reaction occurred between poly vinyl alcohol and di-anthracene by cross-linked by the anthracene dimer in the presence of p-toluenesulfonic acid (p-TSA). This is labled as a Fischer esterification reaction [204]. The general synthesis route is described in Figure 4.41. The specific reaction mechanism involved was described in detail in Figure 4.42. In the esterification reaction, p-TSA is an aromatic sulfonic acid, which is often used as a strong acid catalyst. First, the proton on p-TSA protonates the carbonyl groups. Next, through the charge migration from oxygen to carbon, carbon atom on carbonyl groups becomes more electrophile. The nucleophilic attack from PVA becomes easier due to the positive charge on carbon. This attack generates a new bond between the carbon and oxygen and forms a tetrahedral intermediate, which gives water and the ester after a proton shift.

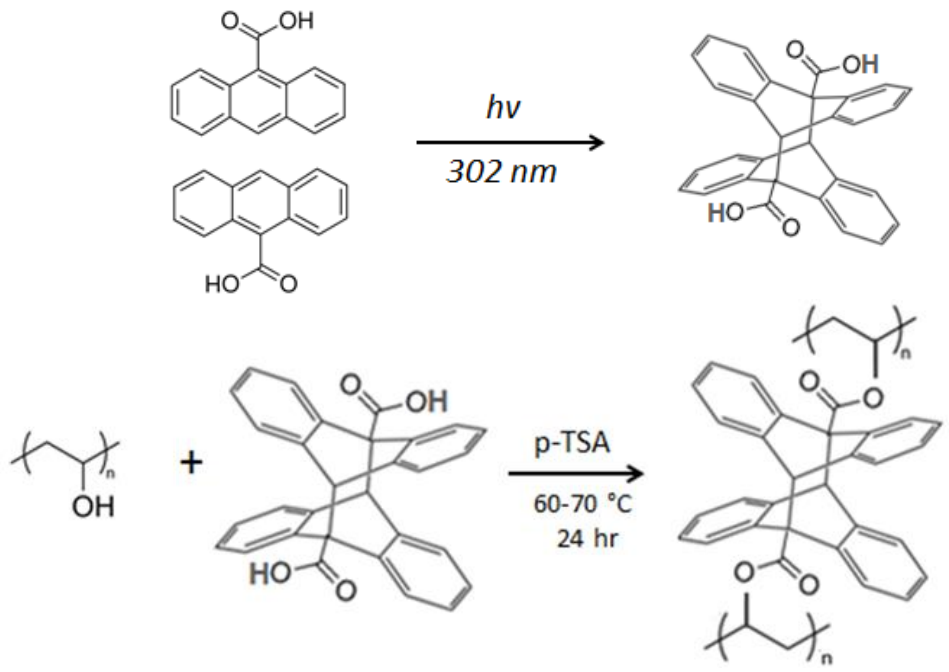

Figure 4. 41 Synthesis Route for Poly-Anthracene.(Top) Dimerization of Anthracene; (Bottom) Fischer Esterification under the Catalyst of p-TSA.

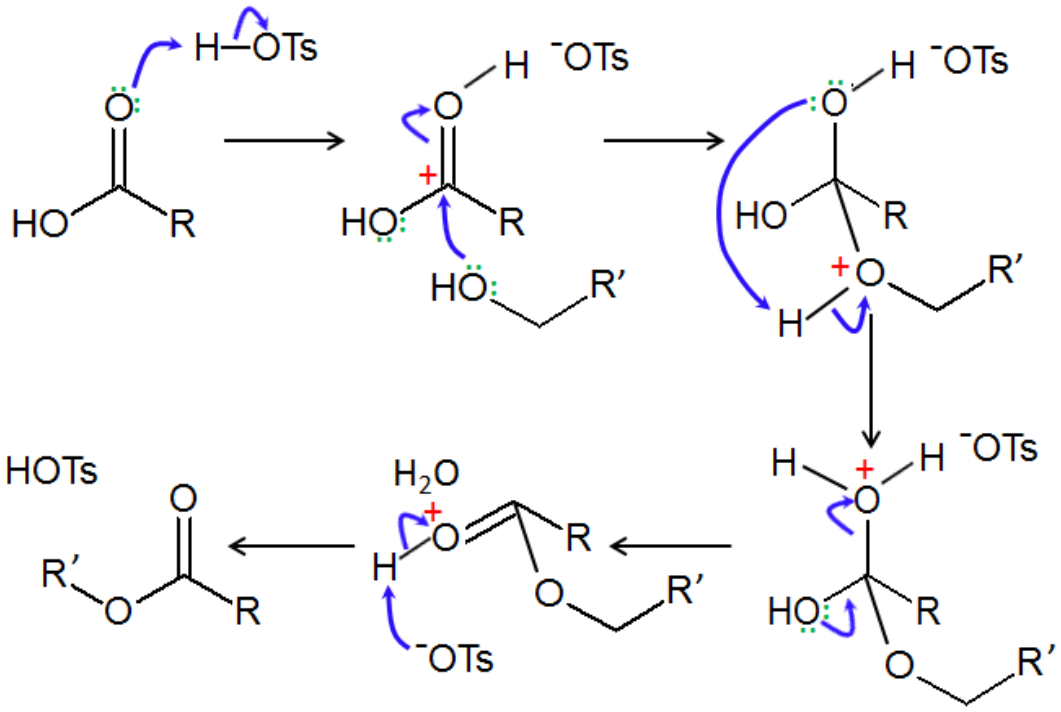

Figure 4. 42 Mechanism for p-TSA Catalyzed Fischer Esterification between Acids and Alcohols**.**

The [4+4] photocycloadditon of anthracene groups was confirmed and analyzed using UV-Vis spectroscopy. Figure 4.43 displays the UV absorbance variation of 9-anthracenecarboxylic acid dilute solution as a function of time. Compared to the UV absorbance of the TCE solution, the absorbance peak was shifted toward the longer wavelength, due to the longer conjugation system than that of the cinnamates. Conjugation can lower the energy differences between energy levels, therefore longer conjugated systems absorb at longer wavelengths [205, 206]. These conjugated systems have a large influence on the peak wavelengths and absorption intensities. The absorbance peaks are located at 330 nm, 345 nm, 365 nm, and 380 nm, corresponding to the anthracene vibroelectronic ^{1}La (1^{1}Ag→1^{1}B1u) transitions [207, 208]. The change in the absorbance value was monitored for continual irradiation, and it is facile to notice that the absorbance band decreases with exposure time and disappears almost completely within 6 hrs of photoirradiation, this implies that there is dimerization of C=C bond to cyclooctane. The absorbance disappearance rate was much slower compared to that of cinnamates. One possible explanation can be that the anthracene with larger conjugated system is more stable than cinnamates. However, it is also possible that the use of a UV lamp at 302 nm wavelength (limited by lab equipment availability) delayed the reaction Because the absorbance at 302 nm is relatively small for anthracene molecule.

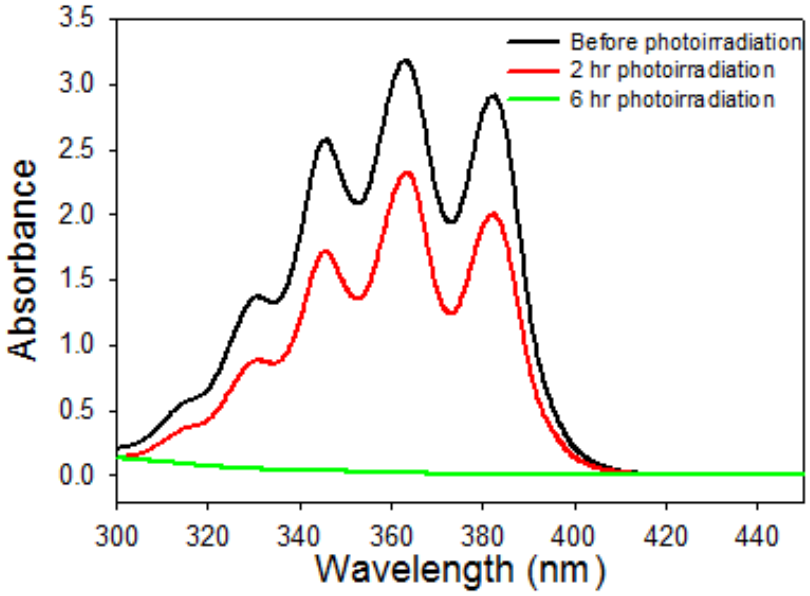

Figure 4. 43 The Change of UV Absorbance of Anthrance Solution as a Function of the UV Exposure Time.

The esterification reaction between the poly vinyl alcohol and di-anthracenecarboxylic acid in the presence of p-TSA was confirmed by IR spectra. The spectra of the solid mixture (di-anthracenecarboxylic acid and poly vinyl alcohol) and the final product poly-AC were displayed in Figure 4.44. By comparing these two spectra, it is obvious that after the reaction, the original absorption peak at 1698 cm^{-1} ($\nu_{C=O}$) disappeared, while the new peaks at 1716 cm^{-1} ($\nu_{C=O}$), 1215 cm^{-1} (ν_{C-O}) and 1110 cm^{-1} (ν_{C-O}) appeared, implying the formation of poly-AC.

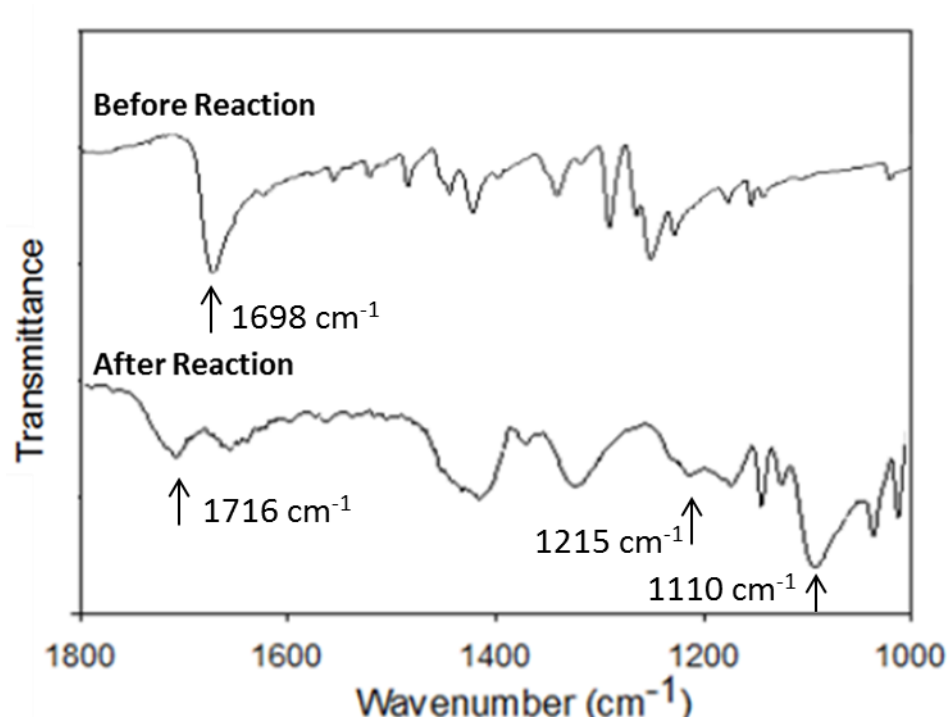

Figure 4. 44 IR Spectra of a Mixture of Reactants before Reaction and after Reaction.

4.2.2 Fluorescence Responses by Mechanical Activation

The cleavage of cyclooctane can yield anthracene which generates fluorescent emission under UV. For a preliminary comparison between cyclobutane-based polymers and cyclooctane-based polymers, thin films of poly-TCE and poly-anthracene were coated on a polyethylene substrate and micro-cracks were generated from bending. The resulting fluorescence along the cracks was observed by microscopy. Both images were taken under the same conditions and processed through ImageJ. The integrated intensity of cracked area of interest divided by the area gave the mean intensity value. It can be seen that anthracene has stronger fluorescence generation due to the larger conjugated system, as shown in Figure 4.45.

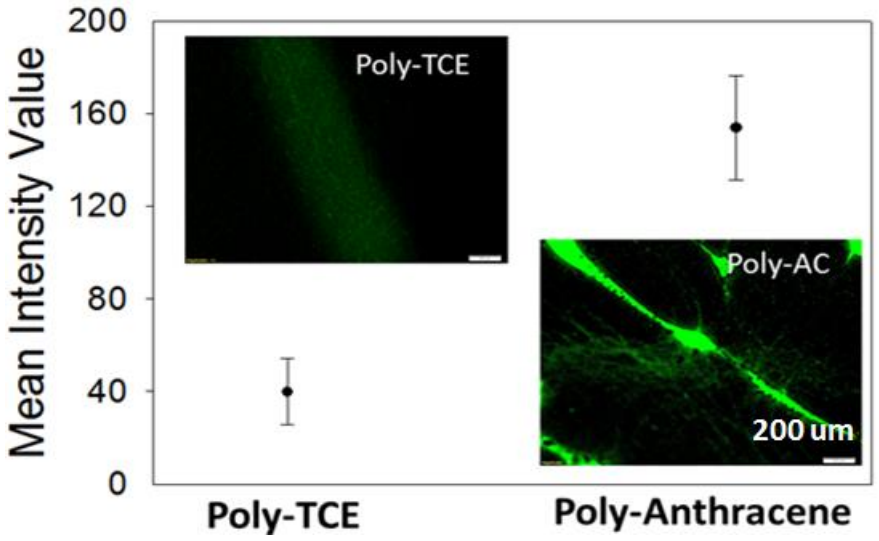

Figure 4.45 Enhanced Fluorescent Intensity Generation from Cracked Poly-Anthracene Compared to Cracked Poly-TCE.

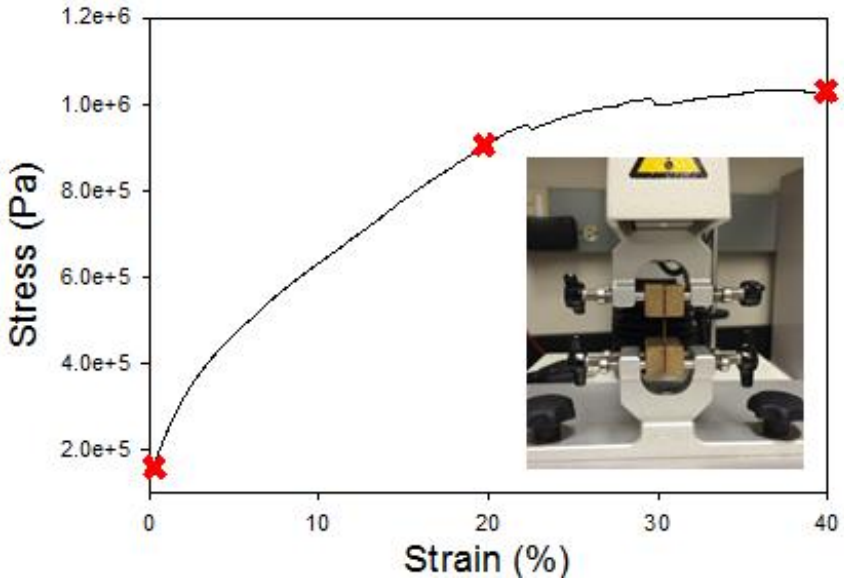

Figure 4. 46 Tensile Test of Poly-Anthracene Film. Inset is the Test Conducted on the Texture Analyzer Machine (TA.XT Plus Texture Analyzer).

In order to explore how the fluorescent intensity changed in response to the applied stress, tensile test was conducted. Texture analyzer (TA.XT Plus Texture Analyzer) coupled with Texture Exponent Software was used to measures the force involved in tension interaction of a probe with the polymer specimen. A rectangular poly-

AC film was gripped at its two ends and pulled to elongate. Pre-test speed and post-test speed were set as 1 mm/sec. The film was extended to 20% and further 40% strain with a strain rate of 1% per second. The stress-strain curve is displayed in Figure 4.46. At 0%, 20% and 40% strain point, images were taken under UV microscopy to monitor the fluorescence change. To establish the relationship between the strains and their corresponding fluorescence response, ten fluorescent micrographs were processed by ImageJ and the average fluorescence densities were calculated. The density change as a function of strain was plotted in Figure 4.47. The fluorescence intensified with increasing strain, indicating the applied tensile force facilitates retro [4+4] cycloaddtion reactions. The driving force for this chemical transformation is the relatively lower C-C bond strength on the cyclooctane ring and the restoration of the anthracene aromaticity [172].

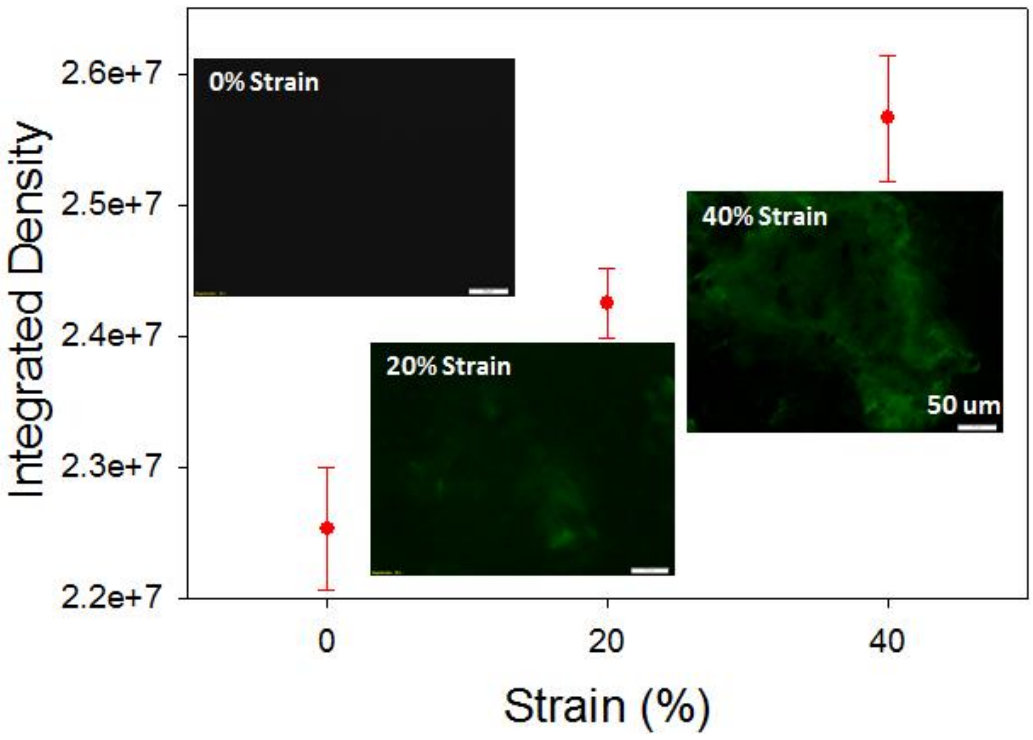

Figure 4. 47 Corresponding Integrated Fluorescent Density of Poly-AC in Tensile Test with Corresponding Images.

CHAPTER 5
SUMMARY AND FUTURE WORK

5.1 Summary

The blending of two or more polymers is an effective means to develop composite materials for desired applications. We have studied the effect of the addition of cyclobutane-based polymers on the thermal and mechanical properties of an epoxy matrix and more importantly, the ability to detect early and in-situ damage. Two cinnamate derivatives, 1,1,1-tris(cinnamoyloxymethyl) ethane (TCE) and poly(vinyl cinnamate) (PVCi), were photoirradiated to produce cross-linked cyclobutane-based polymer, respectively. The cross-linked TCE and PVCi polymers were both thermally stable for a wide range of temperatures. Differential scanning calorimetry (DSC) experiments showed that the addition of the TCE and PVCi polymers shifted the glass transition temperature (T_g) to a lower degree. Both polymer blends showed a lower cross-link density than the neat epoxy whereas the Young's modulus of the epoxy and the polymer blends remain comparable. The experimental results were also used to validate molecular dynamics simulations.

Identification of early damage in polymer composites is of great importance. We have incorporated cyclobutane-based cross-linked polymers into the epoxy matrix and demonstrated early and in-situ damage detection through mechanically induced fluorescence generation. The emergence of cracks was detected by fluorescence at a strain level right beyond the yield point of the polymer blends and the fluorescence intensified with accumulation of the strain. In addition, we tested the effectiveness of

damage in a glass fiber reinforced composite (GFRC) sheet by embedding glass fibers into a polymeric matrix. In the fatigue test the damaged locations were successfully identified through stress induced fluorescent emission. The fluorescent signals intensified with the number of the fatigue cycles. Overall, the results show that the in-situ damages can be detected through fluorescence generation along the crack propagation.

To investigate the effect of mechanophore type, a cyclooctane-based mechanophore, anthracene, was also studied. It is hypothesized that the cleavage of cyclooctane generates monomeric anthracene with fluorescence emission and possesses a larger conjugation system compared to the cinnamoyl functional group. Indeed, it was found that the anthracene moiety has a longer wavelength in excitation and emission compared to the cinnamoyl moiety and a higher quantum yield. We also prepared a poly-AC film, which consisted of poly(vinyl alcohol) (PVA) backbones cross-linked by the anthracene dimer, Di-AC. In the tensile test, the film was extended to 20% and 40% strain and the fluorescence intensified with the increasing strain.

In summary, the study suggests that early, in-situ damage and microcracks can be detected by incorporating cyclobutane-based mechanophore into an epoxy matrix and a glass fiber reinforced composite (GFRC) sheet. The impact of the cyclobutane-based mechanophore on the thermal and mechanical properties of the matrix has also been addressed. The possibilities of employing cyclooctane based mechanophores as earlier damage detection has also been explored.

5.2 Future Directions

So far, we have employed the photodimerization of cinnamoyl functional groups to create cyclobutane stress-sensing moieties, in which the mechanophores were simply used as additives in the polymer blends. The results have clearly demonstrated the effectiveness in early and in-situ damage. However, the fluorescent signals achieved occurred after the yield point and it is always desirable to detect potential damages as early as possible. Another notable drawback of utilizing the cyclobutane-based mechanophores as additives is the significant lowering of the glass transition temperature thus narrows the temperature window in which the matrix can be applied. To overcome these limitations, we propose to improve the system by directly grafting the mechanophore units into the epoxy resin and cross-linker (or hardener) through covalent bonding. The schematic illustration of the approach is displayed in Figure 5.1.

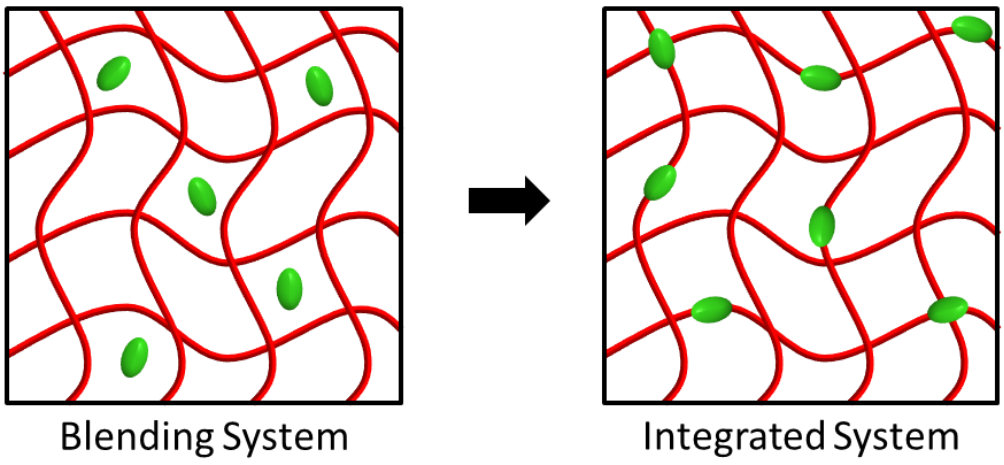

Figure 5. 1 Schematic Illustration of Moving from the Blending System to the Proposed Integrated System. The Epoxy Network is presented in Red and the Mechanophores are presented in Green.

Two routes, as shown in Figure 5.2, will be followed to explore the novel functionalization. The hardener (or cross-linker) will be modified by the addition of mechanophore units and used to form cross-links with un-modified resin, by a

combination of conventional chemical curing and UV activated photodimerization for the mechanophore units. Second, both the hardener and the resin will be modified by the addition of mechanophore units, which by UV curing, form a network polymer cross-linked by stress-sensing units. Route 1 and the first step of Route 2 show the reaction of the hardener, diethylenetriamine (DETA), with cinnamoyl chloride to obtain a di- or tetra-substituted cinnamoyl hardener. The second step of Route 2 shows the preparation of the cinnamoyl containing epoxy resin by the reaction of the resin, diglycidyl ether of bisphenol F (DGEBPF), with cinnamic acid. Specifically, for functionalization of the hardener, a solution of cinnamoyl chloride (0.1 mol for Route 1 and 0.2 mol for Route 2) in dichloromethane (200 mL) will be slowly added dropwise to a mixture of DETA (0.05 mol) and triethylamine (0.2 mol). The reaction solution will be stirred, placed in an ice bath, and purged with nitrogen for 8 hr. To synthesize the cinnamoyl epoxy resin, DGEBPF (0.05 mol) will be first dissolved in 200 mL of diethylene glycol dimethyl ether (diglyme), then cinnamic acid (0.01 mol) and benzyltrimethylammonium chloride catalyst (0.05 mol) will be added. The mixture will be heated to 150 ℃ and react for 5 h under stirring and nitrogen. The crude products will be purified by solvent evaporation, washing, and column chromatography. DGEBPF and DETA will be purchased from Epoxy System Inc. Cinnamoyl chloride, cinnamic acid, dichloromethane, triethylamine, diglyme, and benzyltrimethylammonium chloride will be purchased from Sigma Aldrich. Once the desired epoxy hardener and resin are obtained, they will be mixed well with a pre-determined ratio and cured under UV exposure (302 nm) at room temperature. Similarly to the synthesis described in Figure 5.2, anthracene groups will be incorporated into epoxy hardener and resin to ultimately form cyclooctane as the force-responsive unit.

A similar reaction scheme will be used and the modified resin and hardener will be obtained by the reaction of DGEBPF and DETA with anthracenecarboxylic acid, which will also be purchased from Sigma Aldrich. As previously mentioned, anthracene is expected to offer the advantage of early damage precursor detection over cinnamoyl mechanophores stemming from the enhanced fluorescence quantum yield.

This integrated system is illustrated in Figure 5.3, with the blue units representing the mechanophores on the resin and the red units representing the mechanophores on the hardener. It is hypothesized that a three-dimensional cross-linked polymer will be formed due to the four reactive units on the hardener and the two reactive units on the resin. Overall, the proposed cycloalkane-functional mechanophores will be separately incorporated into networked polymer matrices by both routes to probe their respective effectiveness as crack sensors.

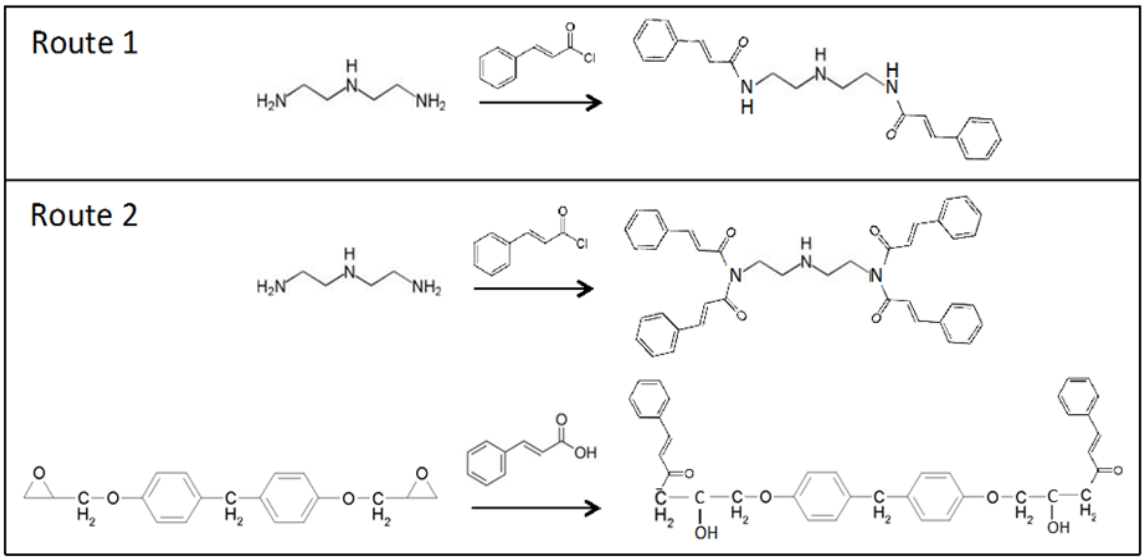

Figure 5. 2 Synthesis Routes for Incorporation of Cinnamoyl Mechanophore Functional Groups. Route 1: Incorporation into Epoxy Hardener for Use with Unmodified Resin. Route 2: Incorporation into Both Epoxy Hardener and Resin.

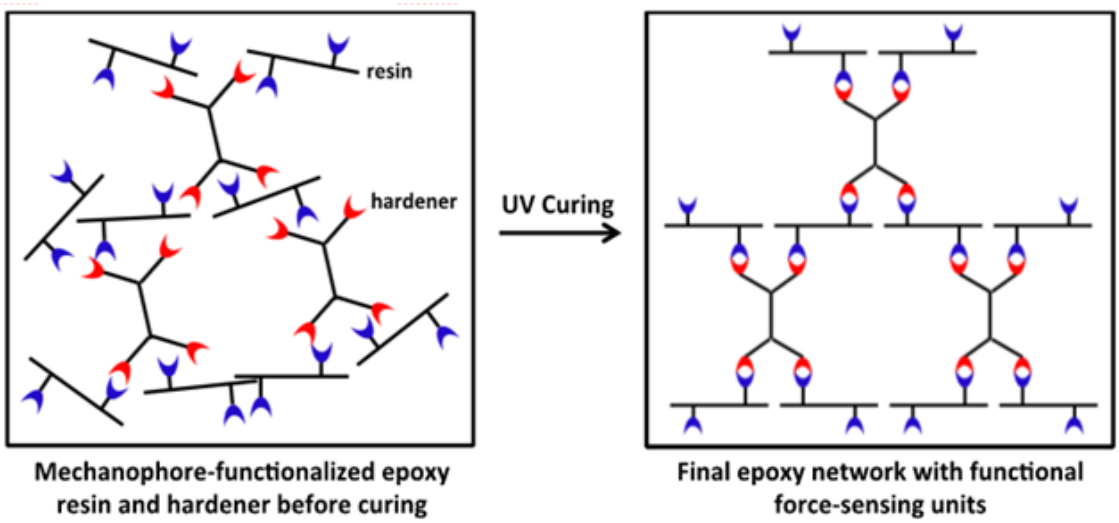

Figure 5. 3 UV Activated Epoxy Curing of Mechanophore-Functionalized Resin and Hardener Units, in Blue and Red, Respectively.

Exploration of Self-Healing

In addition to early damage detection, self-healing remains an interesting and challenging research topic. Previous studies on self-healing have focused on microcapsule-type self-healing (Figure 5.4 (a)), which involves incorporating a microencapsulated healing agent (monomer) and catalyst dispersed within a thermoset matrix [209-211]. When damage occurs, cracks propagate through the matrix, rupturing the embedded microcapsules, and releasing healing agent monomer. The healing agent is then immediately polymerized by contact with the dispersed catalyst [98]. However, once the microcapsules are broken, the self-healing can no longer be achieved. Recently, vascular network-type healing approach (Figure 5.4 (b)) has been developed which makes the repeated self-healing possible in composite material although with the limitation of irreversibility [212-214].

The proposed future direction of the integrated systems may also provide unique opportunities to explore self-healing. Unlike the microcapsule-type or vascular network-type healing, the self-healing of the following proposed mechanophore approach allows for repeatable/reversible self-sensing and self-healing (Figure 5.4 (c)).

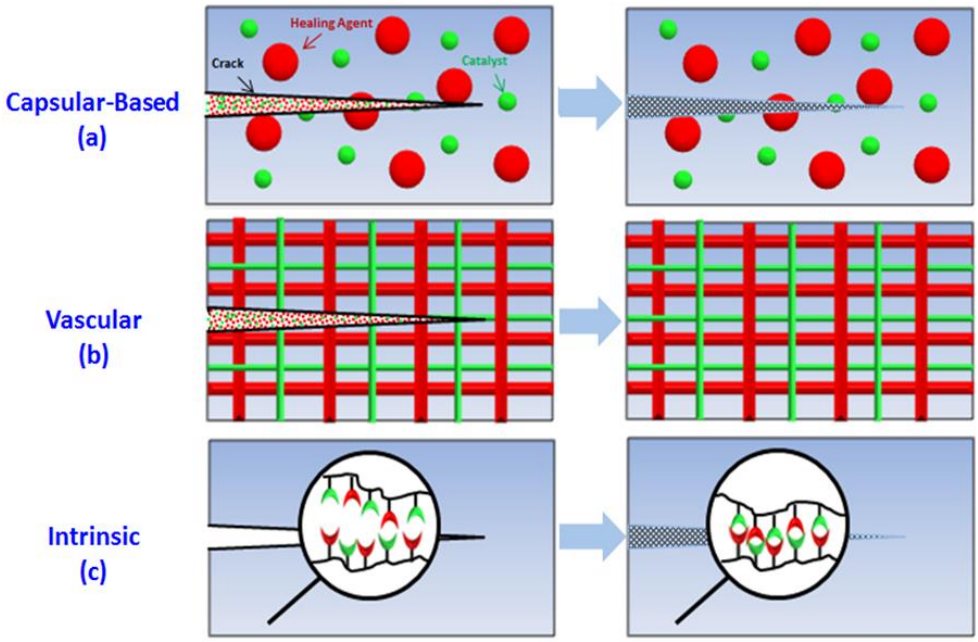

Figure 5. 4 Three Primary Approaches for Self-Healing.

Perhaps one of the most unique advantages of reversible cycloaddition type (cyclobutane and cyclooctane) mechanophores over ring-opening type mechanophores (such as spiropyran) is their self-healing ability in addition to self-sensing. For instance, with spiropyran, while the ring-opening mechanism can be reversed with light, but if the mechanophore molecules break during tension, healing is not possible. Alternatively, the actual mechanical scission of the bonds in the cycloalkane rings in cinnamoyl- and anthracene-based polymers can be completely healed. This self-healing can be achieved by simple UV light exposure to the damage when the crack surfaces contain reactive

moieties that then react to form new chemical bonds under irradiation. The use of reversible photo-crosslinking reactions is based on the reversible photodimerization and photocleavage of cinnamoyl and anthracene moieties (Figure 5.5).

In the integrated systems, the dimerization of these chromophores and recovery of their structure then occur through either [2+2] cycloaddition or [4+4] cycloaddition. As the photoreactive moieties will be used as cross-linkers in polymer networks, the strength of the overall material can then be recovered. The force applied on the systems to generate the damage will be controlled by using a MTS servo hydraulic test system (compression/tension/fatigue). The advantages of the hypothesized self-healing include: 1) Remote activation is easily obtained as light can travel over a long distance, 2) Spatially controlled activation is possible as the light beam (often a laser) can be delivered to selected areas, and 3) Light-triggered processes can be halted and resumed "on-demand" by turning off or turning on the excitation light.

An important consideration for the self-healing experiments is the degree of damage, as it is expected that self-healing will not be possible if the matrix itself is quite damaged. We will thus perform experiments to correlate the damage degree with the applied force and self-healing effectiveness in order to determine the critical damage point. The overall healing efficiency will be determined from measuring the mechanical properties (such as tensile strength, flexural strength, etc.) of the original, cracked, and healed samples.

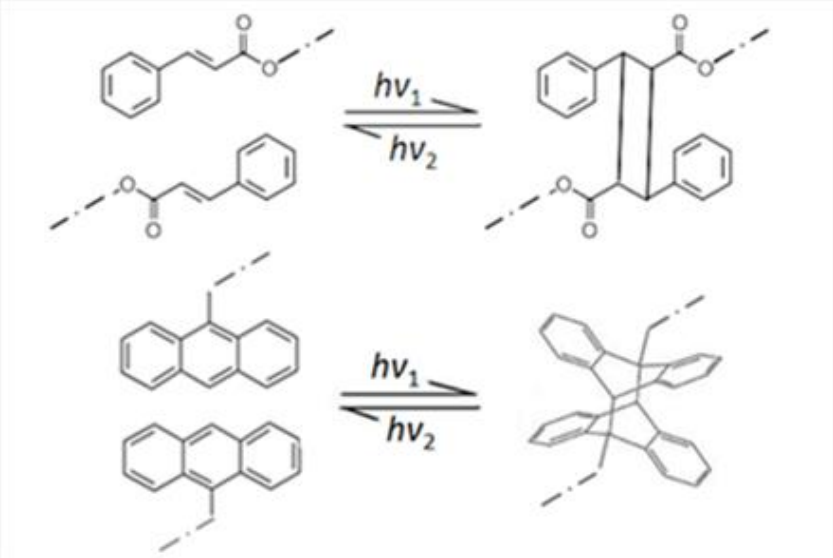

Figure 5. 5 Reversible Photodimerization and Photocleavage under UV Light Irradiation for (Top) Cinnamoyl and (Bottom) Anthracene.

Overall, the future direction of integrated system is anticipated to offer a novel frame work to detect earlier damage, improve thermal and mechanical properties, and explore self-healing over the current mechanophore/self-healing schemes in epoxy matrix. The systematic study will also provide further fundamental understanding of mechanochemistry as a whole.

REFERENCES

1. Gil, E.S. and S.M. Hudson, Stimuli-reponsive polymers and their bioconjugates. Progress in Polymer Science, 2004. **29**(12): p. 1173-1222.

2. Leroux, J.C., et al., Stimuli-responsive liposome-polymer complexes: Toward the design of intelligent drug carriers. Abstracts of Papers American Chemical Society, 2002. **223** (1-2): p. 92-COLL 92.

3. Beyer, M.K. and H. Clausen-Schaumann, Mechanochemistry: The mechanical activation of covalent bonds. Chemical Reviews, 2005. **105**(8): p. 2921-2948.

4. Schnitzer, M.J., K. Visscher, and S.M. Block, Force production by single kinesin motors. Nature Cell Biology, 2000. **2**(10): p. 718-723.

5. Holtz, J.H. and S.A. Asher, Polymerized colloidal crystal hydrogel films as intelligent chemical sensing materials. Nature, 1997. **389**(6653): p. 829-832.

6. Kikuchi, A. and T. Okano, Intelligent thermoresponsive polymeric stationary phases for aqueous chromatography of biological compounds. Progress in Polymer Science, 2002. **27**(6): p. 1165-1193.

7. Benjeddou, A., Advances in piezoelectric finite element modeling of adaptive structural elements: a survey. Computers & Structures, 2000. **76**(1-3): p. 347-363.

8. Kikuchi, A. and T. Okano, Pulsatile drug release control using hydrogels. Advanced Drug Delivery Reviews, 2002. **54**(1): p. 53-77.

9. Galaev, I.Y. and B. Mattiasson, 'Smart' polymers and what they could do in biotechnology and medicine. Trends in Biotechnology, 1999. **17**(8): p. 335-340.

10. Jeong, B. and A. Gutowska, Lessons from nature: stimuli-responsive polymers and their biomedical applications. Trends in Biotechnology, 2002. **20**(7): p. 305-311.

11. Chilkoti, A., et al., Targeted drug delivery by thermally responsive polymers. Advanced Drug Delivery Reviews, 2002. **54**(5): p. 613-630.

12. Meyer, D.E., et al., Drug targeting using thermally responsive polymers and local hyperthermia. Journal of Controlled Release, 2001. **74**(1-3): p. 213-224.

13. Jeong, B., et al., Thermogelling biodegradable copolymer aqueous solutions for injectable protein delivery and tissue engineering. Biomacromolecules, 2002. **3**(4): p. 865-868.

14. Meyer, D.E., et al., Targeting a genetically engineered elastin-like polypeptide to solid tumors by local hyperthermia. Cancer Research, 2001. **61**(4): p. 1548-1554.

15. Bromberg, L.E. and E.S. Ron, Temperature-responsive gels and thermogelling polymer matrices for protein and peptide delivery. Advanced Drug Delivery Reviews, 1998. **31**(3): p. 197-221.

16. Stayton, P.S., et al., Control of protein-ligand recognition using a stimuli-responseive polymer. Nature, 1995. **378**(6556): p. 472-474.

17. Ahn, S.-K., et al., Stimuli-responsive polymer gels. Soft Matter, 2008. **4**(6): p. 1151-1157.

18. Principi, T., et al., Solution properties of hydrophobically modified copolymers of N-isopropylacrylamide and N-glycine acrylamide: A study by microcalorimetry and fluorescence spectroscopy. Macromolecules, 2000. **33**(8): p. 2958-2966.

19. Liu, F. and M.W. Urban, Recent advances and challenges in designing stimuli-responsive polymers. Progress in Polymer Science, 2010. **35**(1-2): p. 3-23.

20. Klouda, L. and A.G. Mikos, Thermoresponsive hydrogels in biomedical applications. European Journal of Pharmaceutics and Biopharmaceutics, 2008. **68**(1): p. 34-45.

21. Stuart, M.A.C., et al., Emerging applications of stimuli-responsive polymer materials. Nature Materials, 2010. **9**(2): p. 101-113.

22. Fujishige, S., K. Kubota, and I. Ando, Phase-transition of aqueous-solutions of poly(N-isopropylacrylamide) and poly(N0isopropylmethacrylamide). Journal of Physical Chemistry, 1989. **93**(8): p. 3311-3313.

23. Schild, H.G., Poly(N-isopropylacrylamide)-experiment, theory and applicaiton. Progress in Polymer Science, 1992. **17**(2): p. 163-249.

24. Deng, Y.H., et al., A novel approach for preparation of thermoresponsive polymer magnetic microspheres with core-shell structure. Advanced Materials, 2003. **15**(20): p. 1729.

25. Qiu, Y. and K. Park, Environment-sensitive hydrogels for drug delivery. Advanced Drug Delivery Reviews, 2001. **53**(3): p. 321-339.

26. Kuijpers, A.J., et al., Characterization of the network structure of carbodiimide cross-linked gelatin gels. Macromolecules, 1999. **32**(10): p. 3325-3333.

27. Wu, X.S., A.S. Hoffman, and P. Yager, Synthesis and characterization of thermally reversible macroporous poly(Niisopropylacrylamide) hydrogels. Journal of Polymer Science Part a-Polymer Chemistry, 1992. **30**(10): p. 2121-2129.

28. Kishi, R., O. Hirasa, and H. Ichijo, Fast responsive poly(N-isopropylacrylamide) hydrogels prepared by gamma-ray irradiation. Polymer Gels and Networks, 1997. **5**(2): p. 145-151.

29. Beebe, D.J., et al., Functional hydrogel structures for autonomous flow control inside microfluidic channels. Nature, 2000. **404**(6778): p. 588.

30. Shibayama, M. and T. Tanaka, Volume phase-transition and related phenomena of polymer gels. Advances in Polymer Science, 1993. **109**: p. 1-62.

31. Chen, G.H. and A.S. Hoffman, Graft-copolymers that exhibit temperature-induced phase-transitions of over a wide-range of pH. Nature, 1995. **373**(6509): p. 49-52.

32. Iwata, H., et al., Preparation of temperature-sensitive membranes by graft-polymerization onto a porous membrane. Journal of Membrane Science, 1991. **55**(1-2): p. 119-130.

33. Okahata, Y., H. Noguchi, and T. Seki, Functional capsule membranes.23.Thermoselective permeation from a polymer grafted capsule membrane. Macromolecules, 1986. **19**(2): p. 493-494.

34. Bajpai, A.K., et al., Responsive polymers in controlled drug delivery. Progress in Polymer Science, 2008. **33**(11): p. 1088-1118.

35. Gupta, P., K. Vermani, and S. Garg, Hydrogels: from controlled release to pH-responsive drug delivery. Drug Discovery Today, 2002. **7**(10): p. 569-579.

36. Roy, D., J.N. Cambre, and B.S. Sumerlin, Future perspectives and recent advances in stimuli-responsive materials. Progress in Polymer Science, 2010. **35**(1-2): p. 278-301.

37. Zhao, C., et al., Polymeric pH-sensitive membranes-A review. Progress in Polymer Science, 2011. **36**(11): p. 1499-1520.

38. Osada, Y., K. Honda, and M. Ohta, Control of water permeability by mechanochemical contraction of poly(methacrylic acid)-grafed membranes. Journal of Membrane Science, 1986. **27**(3): p. 327-338.

39. Kumar, A., et al., Smart polymers: Physical forms and bioengineering applications. Progress in Polymer Science, 2007. **32**(10): p. 1205-1237.

40. Park, S.Y. and Y.H. Bae, Novel pH-sensitive polymers containing sulfonamide groups. Macromolecular Rapid Communications, 1999. **20**(5): p. 269-273.

41. Shchukin, D.G., G.B. Sukhorukov, and H. Mohwald, Smart inorganic/organic nanocomposite hollow microcapsules. Angewandte Chemie-International Edition, 2003. **42**(37): p. 4472-4475.

42. Dong, L.C. and A.S. Hoffman, A novel-approach for preparation of pH-sensitive hydrogels for enteric drug delivery. Journal of Controlled Release, 1991. **15**(2): p. 141-152.

43. Park, K., I.C. Kwon, and K. Park, Oral protein delivery: Current status and future prospect. Reactive & Functional Polymers, 2011. **71**(3): p. 280-287.

44. Kim, Y.H., Y.H. Bae, and S.W. Kim, pH/temperature-ssensitive polymers for macromolecular drug loading and release. Journal of Controlled Release, 1994. **28**(1-3): p. 143-152.

45. Lee, A.S., et al., Structure of pH-dependent block copolymer micelles: Charge and ionic strength dependence. Macromolecules, 2002. **35**(22): p. 8540-8551.

46. Pinkrah, V.T., et al., Physicochemical properties of poly(N-isopropylacrylamide-co-4-vinylpyridine) cationic polyelectrolyte colloidal microgels. Langmuir, 2003. **19**(3): p. 585-590.

47. Gohy, J.F., et al., Stimuli-responsive aqueous micelles from an ABC metallo-supramolecular triblock copolymer. Macromolecules, 2002. **35**(26): p. 9748-9755.

48. Sutton, R.C., et al., Microdomain characterization of stryene imidazole copolymers. Macromolecules, 1988. **21**(8): p. 2432-2439.

49. Mamada, A., et al., Photoinduced phase-transtion of gels. Macromolecules, 1990. **23**(5): p. 1517-1519.

50. Suzuki, A. and T. Tanaka, Phase-transition in polymer gels induced by visible-light. Nature, 1990. **346**(6282): p. 345-347.

51. Bedard, M.F., et al., Polymeric microcapsules with light responsive properties for encapsulation and release. Advances in Colloid and Interface Science, 2010. **158**(1-2): p. 2-14.

52. Shiga, T., Deformation and viscoelastic behavior of polymer gels in electric fields, in Neutron Spin Echo Spectroscopy Viscoelasticity Rheology. 1997. p. 131-163.

53. Yao, L. and S. Krause, Electromechanical responses of strong acid polymer gels in DC electric fields. Macromolecules, 2003. **36**(6): p. 2055-2065.

54. Liu, T.Y., et al., Magnetic-sensitive behavior of intelligent ferrogels for controlled release of drug. Langmuir, 2006. **22**(14): p. 5974-5978.

55. Zrinyi, M., Intelligent polymer gels controlled by magnetic fields. Colloid and Polymer Science, 2000. **278**(2): p. 98-103.

56. Gelbrich, T., M. Feyen, and A.M. Schmidt, Magnetic thermoresponsive core-shell nanoparticles. Macromolecules, 2006. **39**(9): p. 3469-3472.

57. Filipcsei, G., et al., Magnetic field-responsive smart polymer composites, in Oligomers Polymer Composties Molecular Imprinting. 2007. p. 137-189.

58. Farshad, M. and M. Le Roux, Compression properties of magnetostrictive polymer composite gels. Polymer Testing, 2005. **24**(2): p. 163-168.

59. Bhattacharya, S., et al., Temperature-, pH-, and magnetic-field-sensitive hybrid microgels. Small, 2007. **3**(4): p. 650-657.

60. Barsi, L. and M. Zrinyi, Ferrogels as magnetomechanical actuators. Ach-Models in Chemistry, 1998. **135**(3): p. 241-246.

61. Zrinyi, M., D. Szabo, and L. Barsi, Magnetic field sensitive polymeric actuators. Journal of Intelligent Material Systems and Structures, 1998. **9**(8): p. 667-671.

62. Savva, I., et al., Fabrication and Characterization of Magnetoresponsive Electrospun Nanocomposite Membranes Based on Methacrylic Random Copolymers and Magnetite Nanoparticles. Journal of Nanomaterials, 2012.

63. Kang, S.I. and Y.H. Bae, A sulfonamide based glucose-responsive hydrogel with covalently immobilized glucose oxidase and catalase. Journal of Controlled Release, 2003. **86**(1): p. 115-121.

64. Traitel, T., Y. Cohen, and J. Kost, Characterization of glucose-sensitive insulin release systems in simulated in vivo conditions. Biomaterials, 2000. **21**(16): p. 1679-1687.

65. Miyata, T., et al., Preparation of poly(2-glucosyloxyethyl methacrylate)concanavalin A complex hydrogel and its glucose-sensitivity. Macromolecular Chemistry and Physics, 1996. **197**(3): p. 1135-1146.

66. You, L.C., et al., Glucose-sensitive aggregates formed by poly(ethylene oxide)-block-poly(2-glucosyl-oxyethyl acrylate) with coneanavalin A in dilute aqueous medium. Macromolecules, 2003. **36**(1): p. 1-4.

67. Izyumskaya, N., et al., Processing, structure, properties, and applications of PZT thin films. Critical Reviews in Solid State and Materials Sciences, 2007. **32**(3-4): p. 111-202.

68. Zhu, X.H. and Z.Y. Meng, Operational principle fabricaiton and displacement characteristics of a functionally gradient piezoelectric ceramic actuator. Sensors and Actuators a-Physical, 1995. **48**(3): p. 169-176.

69. Koganezawa, S., et al., Dual-stage actuator system for magnetic disk drives using a shear mode piezoelectric microactuator. Ieee Transactions on Magnetics, 1999. **35**(2): p. 988-992.

70. Takagi, K., et al., Fabrication and evaluation of PZT/Pt piezoelectric composites and functionally graded actuators. Journal of the European Ceramic Society, 2003. **23**(10): p. 1577-1583.

71. Hess, A.E., et al., Development of a stimuli-responsive polymer nanocomposite toward biologically optimized, MEMS-based neural probes. Journal of Micromechanics and Microengineering, 2011. **21**(5).

72. Takacs, L., Mechanochemistry and the Other Branches of Chemistry: Similarities and Differences. Acta Physica Polonica A, 2012. **121**(3): p. 711-714.

73. Boldyrev, V.V. and K. Tkacova, Mechanochemistry of solids: Past, present, and prospects. Journal of Materials Synthesis and Processing, 2000. **8**(3-4): p. 121-132.

74. James, S.L., et al., Mechanochemistry: opportunities for new and cleaner synthesis. Chemical Society Reviews, 2012. **41**(1): p. 413-447.

75. Braga, D., et al., Three Polymorphic Forms of the Co-Crystal 4,4 '-Bipyridine/Pimelic Acid and their Structural, Thermal, and Spectroscopic Characterization. Chemistry-a European Journal, 2008. **14**(32): p. 10149-10159.

76. Lu, J. and S. Rohani, Preparation and Characterization of Theophylline-Nicotinamide Cocrystal. Organic Process Research & Development, 2009. **13**(6): p. 1269-1275.

77. Etter, M.C., S.M. Reutzel, and C.G. Choo, Self-organization of adenine and thymine in the solid-state. Journal of the American Chemical Society, 1993. **115**(10): p. 4411-4412.

78. Restrepo, D., et al., Size controlled mechanochemical synthesis of ZrSi2. Chemical Communications, 2013. **49**(7): p. 707-709.

79. Kauzmann, W. and H. Eyring, The viscous flow of large molecules. Journal of the American Chemical Society, 1940. **62**: p. 3113-3125.

80. Sohma, J., Mechanochemistry of polymers. Progress in Polymer Science, 1989. **14**(4): p. 451-596.

81. Dachille, F. and R. Roy, Effectiveness of shearing stresses in accelerating solid phase reactions at low temperatures and high pressures. Journal of Geology, 1964. **72**(2): p. 243-247.

82. Tojo, T., Q.W. Zhang, and F. Saito, Mechanochemical synthesis of rutile-type CrMO4 (M = V, Sb) and their solid solutions. Journal of Solid State Chemistry, 2006. **179**(2): p. 433-437.

83. Nachbaur, V., et al., Mecanosynthesis of partially inverted zinc ferrite. Journal of Alloys and Compounds, 2009. **473**(1-2): p. 303-307.

84. Cristobal, A.A., et al., Structural alterations during mechanochemical activation of a titanium-magnetite mixture. Materials Chemistry and Physics, 2008. **111**(2-3): p. 341-345.

85. Jacobsen, C.J.H., et al., Synthesis of ternary nitrides by mechanochemical alloying. Journal of Materials Chemistry, 2002. **12**(10): p. 3113-3116.

86. Nichols, P.J., C.L. Raston, and J.W. Steed, Engineering of porous pi-stacked solids using mechanochemistry. Chemical Communications, 2001(12): p. 1062-1063.

87. Kolotilov, S.V., et al., Efficient mechanochemical synthesis of tris(pyrazolylborate) complexes of manganese(II), cobalt(II) and nickel(II). Inorganic Chemistry Communications, 2004. **7**(4): p. 485-488.

88. Sokolov, M.N., et al., New syntheses of Nb-2(mu-Q(2))(2)(4+) (Q =S, Se) complexes with bidentate ligands, their isomerism and electronic structure. Inorganica Chimica Acta, 2005. **358**(7): p. 2371-2383.

89. Suzuki, N., et al., Hydrogen formation during wet grinding of alumina and silicon-carbide. Chemistry Letters, 1994(2): p. 327-330.

90. Kameda, J., K. Saruwatari, and H. Tanaka, Hydrogen generation by wet grinding of quartz powders and its dependence on the pH and ionic strength of liquid media. Bulletin of the Chemical Society of Japan, 2003. **76**(11): p. 2153-2154.

91. Kameda, J., K. Saruwatari, and H. Tanaka, H-2 generation during dry grinding of kaolinite. Journal of Colloid and Interface Science, 2004. **275**(1): p. 225-228.

92. Streletskii, A.N., et al., Hydrogenation of CO and C during mechanical treatment of Zr and Ni containing systems, in Mechanically Alloyed, Metastable and Nanocrystalline Materials, Part 1, M.D. Baro and S. Surinach, Editors. 1998. p. 283-288.

93. Streletskii, A.N., et al., Mechanochemical reactions in gas (H2,Co) solid (Zr,a-NiZr) systems, in Metastable, Mechanically Alloyed and Nanocrystalline Materials, Pts 1 and 2, R. Schulz, Editor. 1996. p. 539-544.

94. Turcaniova, L. and P. Balaz, Reactivity of coal activated by mechanochemical treatment. Journal of Materials Synthesis and Processing, 2000. **8**(5-6): p. 365-367.

95. Black, A.L., J.M. Lenhardt, and S.L. Craig, From molecular mechanochemistry to stress-responsive materials. Journal of Materials Chemistry, 2011. **21**(6): p. 1655-1663.

96. Caruso, M.M., et al., Mechanically-Induced Chemical Changes in Polymeric Materials. Chemical Reviews, 2009. **109**(11): p. 5755-5798.

97. Davis, D.A., et al., Force-induced activation of covalent bonds in mechanoresponsive polymeric materials. Nature, 2009. **459**(7243): p. 68-72.

98. Bensimon, D., et al., Stretching DNA with a receding meniscus-experiments and models. Physical Review Letters, 1995. **74**(23): p. 4754-4757.

99. Clausen-Schaumann, H., et al., Force spectroscopy with single bio-molecules. Current Opinion in Chemical Biology, 2000. **4**(5): p. 524-530.

100. Kishino, A. and T. Yanagida, Force measurements by micromanipulation of a single actin filament by glass needles. Nature, 1988. **334**(6177): p. 74-76.

101. Smith, S.B., L. Finzi, and C. Bustamante, Direct mechanical measurements of the elasticity of single DNA-molecules by using magnetic beads. Science, 1992. **258**(5085): p. 1122-1126.

102. Ashkin, A., et al., Force generation of organelle transport measured invivi by an infrared-laser trap. Nature, 1990. **348**(6299): p. 346-348.

103. Zhang, Z., et al., Enzymatic surface erosion of poly(trimethylene carbonate) films studied by atomic force microscopy. Biomacromolecules, 2005. **6**(6): p. 3404-3409.

104. Grandbois, M., et al., How strong is a covalent bond? Science, 1999. **283**(5408): p. 1727-1730.

105. Tsuda, Y., et al., Torsional rigidity of single actin filaments and actin-actin bond breaking force under torsion measured directly by in vitro micromanipulation. Proceedings of the National Academy of Sciences of the United States of America, 1996. **93**(23): p. 12937-12942.

106. Arai, Y., et al., Tying a molecular knot with optical tweezers. Nature, 1999. **399**(6735): p. 446-448.

107. Saitta, A.M. and M.L. Klein, Evolution of fragments formed at the rupture of a knotted alkane molecule. Journal of the American Chemical Society, 1999. **121**(50): p. 11827-11830.

108. Saitta, A.M. and M.L. Klein, Polyethylene under tensil load: Strain energy storage and breaking of linear and knotted alkanes probed by first-principles molecular dynamics calculations. Journal of Chemical Physics, 1999. **111**(20): p. 9434-9440.

109. Saitta, A.M., et al., Influence of a knot on the strength of a polymer strand. Nature, 1999. **399**(6731): p. 46-48.

110. Glynn, P.A.R., Vanderho.Bm, and P.M. Reilly, General model for prediction of molecular weight distributions of degraded polymers-development and comparison with ultrasonic degradation experiments. Journal of Macromolecular Science-Chemistry, 1972. **A 6**(8): p. 1653-1664.

111. Glynn, P.A.R. and Vanderho.Bm, Degradation of polystyrene in solution by ultrasonation-molecular weight distribution study. Journal of Macromolecular Science-Chemistry, 1973. **A 7**(8): p. 1695-1719.

112. Staudinger, H. and H.F. Bondy, On isoprene and caoutchuc, 17. Announcement: On the fractioning of balata. Berichte Der Deutschen Chemischen Gesellschaft, 1930. **63**: p. 724-730.

113. Lumley, J.L., Drag reduction by additives. Annual Review of Fluid Mechanics, 1969. **1**: p. 367-&.

114. Horn, A.F., Midpoint scission of macromolecules in dilute solution in turbulent-flow. Nature, 1984. **312**(5990): p. 140-141.

115. Merrill, E.W. and A.F. Horn, Scission of macromolecules in dilute solution-extensional and turbulent flows. Polymer Communications, 1984. **25**(5): p. 144-146.

116. Nguyen, T.Q., Dynamics of flexible polymer chains in elongational flow. Chimia, 2001. **55**(3): p. 147-154.

117. Carrington, S.P. and J.A. Odell, How do polymers stretch in stagnation point extensional flow-fields? Journal of Non-Newtonian Fluid Mechanics, 1996. **67**: p. 269-283.

118. Merrill, E.W. and P. Leopairat, Scission of non-interpenetrating macromolecules in transient extensional flows. Polymer Engineering and Science, 1980. **20**(7): p. 505-511.

119. Buchholz, B.A., et al., Flow-induced chain scission as a physical route to narrowly distributed, high molar mass polymers. Polymer, 2004. **45**(4): p. 1223-1234.

120. Smith, D.E. and S. Chu, Response of flexible polymers to a sudden elongational flow. Science, 1998. **281**(5381): p. 1335-1340.

121. Wiggins, K.M., J.N. Brantley, and C.W. Bielawski, Methods for activating and characterizing mechanically responsive polymers. Chemical Society Reviews, 2013. **42**(17): p. 7130-7147.

122. Brantley, J.N., K.M. Wiggins, and C.W. Bielawski, Polymer mechanochemistry: the design and study of mechanophores. Polymer International, 2013. **62**(1): p. 2-12.

123. Piermattei, A., S. Karthikeyan, and R.P. Sijbesma, Activating catalysts with mechanical force. Nature Chemistry, 2009. **1**(2): p. 133-137.

124. Tennyson, A.G., K.M. Wiggins, and C.W. Bielawski, Mechanical Activation of Catalysts for C-C Bond Forming and Anionic Polymerization Reactions from a Single Macromolecular Reagent. Journal of the American Chemical Society, 2010. **132**(46): p. 16631-16636.

125. Lenhardt, J.M., A.L. Black, and S.L. Craig, gem-Dichlorocyclopropanes as Abundant and Efficient Mechanophores in Polybutadiene Copolymers under Mechanical Stress. Journal of the American Chemical Society, 2009. **131**(31): p. 10818-+.

126. Klukovich, H.M., et al., Tension Trapping of Carbonyl Ylides Facilitated by a Change in Polymer Backbone. Journal of the American Chemical Society, 2012. **134**(23): p. 9577-9580.

127. Florea, M., New Use of size-exclusion chromatography in kinetics of mechanical degradation of polymers in solution. Journal of Applied Polymer Science, 1993. **50**(12): p. 2039-2045.

128. Li, J., S.Y. Guo, and X.N. Li, Degradation kinetics of polystyrene and EPDM melts under ultrasonic irradiation. Polymer Degradation and Stability, 2005. **89**(1): p. 6-14.

129. Taghizadeh, M.T. and A. Bahadori, Degradation kinetics of poly (vinyl-pyrrolidone) under ultrasonic irradiation. Journal of Polymer Research, 2009. **16**(5): p. 545-554.

130. Hickenboth, C.R., et al., Biasing reaction pathways with mechanical force. Nature, 2007. **446**(7134): p. 423-427.

131. Klukovich, H.M., et al., Mechanically Induced Scission and Subsequent Thermal Remending of Perfluorocyclobutane Polymers. Journal of the American Chemical Society, 2011. **133**(44): p. 17882-17888.

132. Kryger, M.J., et al., Masked Cyanoacrylates Unveiled by Mechanical Force. Journal of the American Chemical Society, 2010. **132**(13): p. 4558-+.

133. Brantley, J.N., K.M. Wiggins, and C.W. Bielawski, Unclicking the Click: Mechanically Facilitated 1,3-Dipolar Cycloreversions. Science, 2011. **333**(6049): p. 1606-1609.

134. Dasgupta, A. and M. Pecht, MATERIAL FAILURE MECHANISMS AND DAMAGE MODELS. Ieee Transactions on Reliability, 1991. **40**(5): p. 531-536.

135. Sih, G.C. and X.S. Tang, Micro/macro-crack growth due to creep-fatigue dependency on time-temperature material behavior. Theoretical and Applied Fracture Mechanics, 2008. **50**(1): p. 9-22.

136. Kwon, J.D., et al., An investigation of the degradation characteristics for casting stainless steel, CF8M, under high temperatures. Nuclear Engineering and Design, 2000. **198**(3): p. 227-240.

137. Drummond, J.L., Degradation, fatigue, and failure of resin dental composite materials. Journal of Dental Research, 2008. **87**(8): p. 710-719.

138. John, R., K.V. Jata, and K. Sadananda, Residual stress effects on near-threshold fatigue crack growth in friction stir welds in aerospace alloys. International Journal of Fatigue, 2003. **25**(9-11): p. 939-948.

139. Farrar, C.R. and K. Worden, An introduction to structural health monitoring. Philosophical Transactions of the Royal Society a-Mathematical Physical and Engineering Sciences, 2007. **365**(1851): p. 303-315.

140. Ortiz, M., Microcrack coalescence and macroscopic crack-growth initiaion in brittle solides. International Journal of Solids and Structures, 1988. **24**(3): p. 231-250.

141. Ritchie, R.O., Mechanisms of fatigue-crack propagation in ductile and brittle solids. International Journal of Fracture, 1999. **100**(1): p. 55-83.

142. Kim, J.T., et al., Damage identification in beam-type structures: frequency-based method vs mode-shape-based method. Engineering Structures, 2003. **25**(1): p. 57-67.

143. Salawu, O.S., Detection of structural damage through changes in frequency: A review. Engineering Structures, 1997. **19**(9): p. 718-723.

144. Giurgiutiu, V. and A. Zagrai, Damage detection in thin plates and aerospace structures with the electro-mechanical impedance method. Structural Health Monitoring-an International Journal, 2005. **4**(2): p. 99-118.

145. Hamzeloo, S.R., M. Shamshirsaz, and S.M. Rezaei, Damage detection on hollow cylinders by Electro-Mechanical Impedance method: Experiments and Finite Element Modeling. Comptes Rendus Mecanique, 2012. **340**(9): p. 668-677.

146. Zagrai, A.N. and V. Giurgiutiu, Electro-mechanical impedance method for crack detection in thin plates. Journal of Intelligent Material Systems and Structures, 2001. **12**(10): p. 709-718.

147. Kessler, S.S., S.M. Spearing, and C. Soutis, Damage detection in composite materials using Lamb wave methods. Smart Materials & Structures, 2002. **11**(2): p. 269-278.

148. Monnier, T., Lamb waves-based impact damage monitoring of a stiffened aircraft panel using piezoelectric transducers. Journal of Intelligent Material Systems and Structures, 2006. **17**(5): p. 411-421.

149. Zhang, Y. Piezoelectric paint sensor for real-time structural health monitoring. 2005.

150. Ali, R., D.R. Mahapatra, and S. Gopalakrishnan, Constrained piezoelectric thin film for sensing of subsurface cracks. Smart Materials & Structures, 2005. **14**(2): p. 376-386.

151. Rattanachan, S., Y. Miyashita, and Y. Mutoh, Fabrication of piezoelectric laminate for smart material and crack sensing capability. Science and Technology of Advanced Materials, 2005. **6**(6): p. 704-711.

152. Monti, M., et al., Impact Damage Sensing in Glass Fiber Reinforced Composites Based on Carbon Nanotubes by Electrical Resistance Measurements. Journal of Applied Polymer Science, 2011. **122**(4): p. 2829-2836.

153. Pucci, A., et al., Bis(benzoxazolyl)stilbene excimers as temperature and deformation sensors for biodegradable poly(1,4-butylene succinate) films. Journal of Materials Chemistry, 2007. **17**(8): p. 783-790.

154. Chi, Z.G., et al., Recent advances in organic mechanofluorochromic materials. Chemical Society Reviews, 2012. **41**(10): p. 3878-3896.

155. Ooyama, Y. and Y. Harima, Molecular design of mechanofluorochromic dyes and their solid-state fluorescence properties. Journal of Materials Chemistry, 2011. **21**(23): p. 8372-8380.

156. Qi, Q.K., et al., AIE (AIEE) and mechanofluorochromic performances of TPE-methoxylates: effects of single molecular conformations. Rsc Advances, 2013. **3**(21): p. 7996-8002.

157. Crenshaw, B.R., et al., Deformation-induced color changes in mechanochromic polyethylene blends. Macromolecules, 2007. **40**(7): p. 2400-2408.

158. Chen, Y.L., et al., Mechanically induced chemiluminescence from polymers incorporating a 1,2-dioxetane unit in the main chain. Nature Chemistry, 2012. **4**(7): p. 559-562.

159. Neebe, M., et al., Thermochromism of bacteriorhodopsin and its pH dependence. Journal of Physical Chemistry B, 2008. **112**(23): p. 6946-6951.

160. Durr, H., A new photochromic system potential limitations. Pure and Applied Chemistry, 1990. **62**(8): p. 1477-1482.

161. Schonberg, A., et al., Experiments with 4-thiopyrones and with 2,2',6,6'-tetraphenyl-4,4'-dipyrylene Journal of the American Chemical Society, 1958. **80**(23): p. 6312-6315.

162. Yoshida, M., et al., Two-dimensional piezochromism and orientational modulations in polysilane monolayer. Macromolecules, 1997. **30**(6): p. 1860-1862.

163. Minkin, V.I., Photo-, thermo-, solvato-, and electrochromic spiroheterocyclic compounds. Chemical Reviews, 2004. **104**(5): p. 2751-2776.

164. Bucknall, C.B. and A.H. Gilbert, Toughening tetrafunctional epoxy-resions using polyetherimide. Polymer, 1989. **30**(2): p. 213-217.

165. Cantwell, W.J. and J. Morton, The impact resistance of composite-materials-a review. Composites, 1991. **22**(5): p. 347-362.

166. Allaoui, A., et al., Mechanical and electrical properties of a MWNT/epoxy composite. Composites Science and Technology, 2002. **62**(15): p. 1993-1998.

167. Bascom, W.D., et al., Fracture of epoxy-modified and elastermer0modified and elastomer. Journal of Applied Polymer Science, 1975. **19**(9): p. 2545-2562.

168. Gong, X.Y., The dynamic mechanical behavior of random-in-plane short fiber-reinforced epoxy resin composites. Polymers for Advanced Technologies, 1996. **7**(2): p. 141-145.

169. Norkhairunnisa, M., A.B. Azhar, and C.W. Shyang, Effects of organo-montmorillonite on the mechanical and morphological properties of epoxy/glass fiber composites. Polymer International, 2007. **56**(4): p. 512-517.

170. Maity, T. and B.C. Samanta, Modification of Glass Fiber-Reinforced Epoxy with Amine Functional Aniline Formaldehyde Condensate (AFAFC). Journal of Adhesion Science and Technology, 2010. **24**(6): p. 1031-1043.

171. Brantseva, T.V., et al., Modification of epoxy resin by polysulfone to improve the interfacial and mechanical properties in glass fibre composites. II. Adhesion of the

epoxy-polysulfone matrices to glass fibres. Journal of Adhesion Science and Technology, 2004. **18**(11): p. 1293-1308.

172. Manjunatha, C.M., et al., The Tensile Fatigue Behavior of a Glass-fiber Reinforced Plastic Composite Using a Hybrid-toughened Epoxy Matrix. Journal of Composite Materials, 2010. **44**(17): p. 2095-2109.
173. Cho, S.Y., J.G. Kim, and C.M. Chung, A fluorescent crack sensor based on cyclobutane-containing crosslinked polymers of tricinnamates. Sensors and Actuators B-Chemical, 2008. **134**(2): p. 822-825.

174. Iimura, Y., et al., Alignment control of liquid crystal molecules using photo-dimerization reaction of poly(vinyl cinnamate). Ieice Transactions on Electronics, 1996. **E79C**(8): p. 1040-1046.

175. Murase, S., et al., Photo-optical control with large refractive index changes by photodimerization of poly(vinyl cinnamate) film. Macromolecules, 1997. **30**(25): p. 8088-8090.

176. Tsuda, M., Some aspects of photosensitivity of poly(vinyl cinnamate). Journal of Polymer Science Part a-General Papers, 1964. **2**(6PA): p. 2907-&.

177. Song, Y.K., et al., Fluorescence sensing of microcracks based on cycloreversion of a dimeric anthracene moiety. Journal of Materials Chemistry, 2012. **22**(4): p. 1380-1386.

178. Xing, J.F., et al., C-2v symmetrical two-photon polymerization initiators with anthracene core: synthesis, optical and initiating properties. Physical Chemistry Chemical Physics, 2012. **14**(45): p. 15785-15792.

179. Gossweiler, G.R., et al., Mechanochemical Activation of Covalent Bonds in Polymers with Full and Repeatable Macroscopic Shape Recovery. Acs Macro Letters, 2014. **3**(3): p. 216-219.

180. Cho, S.Y., J.G. Kim, and C.M. Chung, Photochemical Crack Healing in Cinnamate-Based Polymers. Journal of Nanoscience and Nanotechnology, 2010. **10**(10): p. 6972-6976.

181. Koo, B., et al., Study of glass transition temperature (T-g) of novel stress-sensitive composites using molecular dynamic simulation. Modelling and Simulation in Materials Science and Engineering, 2014. **22**(6).

182. Egerton, P.L., E. Pitts, and A. Reiser, Photocycloaddition in solid polyvinyal cinnamate. Macromolecules, 1981. **14**(1): p. 95-100.

183. Ramamurthy, V. and K. Venkatesan, Photochemical reactions of organic-crystals. Chemical Reviews, 1987. **87**(2): p. 433-481.

184. Oya, N., et al., Photoinduced mendable network polymer from poly(butylene adipate) end-functionalized with cinnamoyl groups. Polymer Journal, 2012. **44**(7): p. 724-729.

185. Ali, A.H. and K.S.V. Srinivasan, Photoresponsive functionalized vinyl cinnamate polymers: Synthesis and characterization. Polymer International, 1997. **43**(4): p. 310-316.

186. Coleman, M.M., et al., Infrared characterization of poly(vinyl cinnamate) and its blends with poly(4-vinyl phenol) before and after UV exposure. Journal of Polymer Science Part B-Polymer Physics, 1998. **36**(9): p. 1579-1590.

187. Chae, B., et al., Photoreaction and molecular reorientation in a nanoscaled film of poly(methyl 4-(methacryloyloxy)cinnamate) studied by two-dimensional FTIR and UV correlation spectroscopy. Langmuir, 2003. **19**(3): p. 687-695.

188. Kim, T.D., H.M. Bae, and K.S. Lee, Synthesis and characterization of a new polyester having photo-crosslinkable cinnamoyl group. Bulletin of the Korean Chemical Society, 2002. **23**(7): p. 1031-1034.

189. Kim, W.G., Photocure Reactions of Photoreactive Prepolymers with Cinnamate Groups. Bulletin of the Korean Chemical Society, 2011. **32**(3): p. 993-999.

190. Bandyopadhyay, A., et al., Molecular modeling of crosslinked epoxy polymers: The effect of crosslink density on thermomechanical properties. Polymer, 2011. **52**(11): p. 2445-2452.

191. Brostow, W., et al., Prediction of glass transition temperatures: Binary blends and copolymers. Materials Letters, 2008. **62**(17-18): p. 3152-3155.

192. Nielsen, L.E., Cross-linking-effect on physical properties of polymers. Journal of Macromolecular Science-Reviews in Macromolecular Chemistry, 1969. **C 3**(1): p. 69-&.

193. Blumstei.A, Polymerization of adsorbed monolayers. Journal of Polymer Science Part a-General Papers, 1965. **3**(7PA): p. 2665-&.

194. Collier, A., et al., Degradation of polymer electrolyte membranes. International Journal of Hydrogen Energy, 2006. **31**(13): p. 1838-1854.

195. Chattopadhyay, D.K. and D.C. Webster, Thermal stability and flame retardancy of polyurethanes. Progress in Polymer Science, 2009. **34**(10): p. 1068-1133.

196. Aoyagi, Y., K. Yamashita, and Y. Doi, Thermal degradation of poly (R)-3-hydroxybutyrate , poly epsilon-caprolactone , and poly (S)-lactide. Polymer Degradation and Stability, 2002. **76**(1): p. 53-59.

197. Starnes, W.H., Structural and mechanistic aspects of the thermal degradation of poly(vinyl chloride). Progress in Polymer Science, 2002. **27**(10): p. 2133-2170.

198. Kim, H.T. and J.K. Park, Thermal degradation of poly(vinyl cinnamate). Polymer Bulletin, 1998. **41**(3): p. 325-331.

199. Bach, R.D. and O. Dmitrenko, Strain energy of small ring hydrocarbons. Influence of C-H bond dissociation energies. Journal of the American Chemical Society, 2004. **126**(13): p. 4444-4452.

200. Ghosh, P., et al., Dynamic mechanical analysis of FRP composites based on different fiber reinforcements and epoxy resin as the matrix material. Journal of Applied Polymer Science, 1997. **64**(12): p. 2467-2472.

201. Peng, K., et al., Scalable Preparation of Multiscale Carbon Nanotube/Glass Fiber Reinforcements and Their Application in Polymer Composites. Fibers and Polymers, 2014. **15**(6): p. 1242-1250.

202. Gupta, N., B.S. Brar, and E. Woldesenbet, Effect of filler addition on the compressive and impact properties of glass fibre reinforced epoxy. Bulletin of Materials Science, 2001. **24**(2): p. 219-223.

203. Padmanabhan, K., Time-temperature failure analysis of epoxies and unidirectional glass epoxy composites in compression. Composites Part a-Applied Science and Manufacturing, 1996. **27**(8): p. 585-596.

204. Darstellung der Ester. Berichte der Deutschen chemischen Gesellschaft zu Berlin, 1895. **28**(3): p. 3252-3258.

205. Abdel-Mottaleb, M.S.A., et al., Fluorescence and photostability studies of anthracene-9-carboxylic acid in different media. International Journal of Photoenergy, 2000. **2**: p. 47-53.

206. Frank, P.G., et al., Intra- Chain Photodimerization of Pendant Anthracene Units as an Effi cient Route to Single- Chain Nanoparticle Fabrication. Macromolecular Rapid Communications, 2014. **35**(2): p. 249-253.

207. Zilberg, S., et al., The vibrational structure of the S0-S1 transmition of anthracne. Chemical Physics, 1994. **186**(2-3): p. 303-316.

208. Wolf, J. and G. Hohlneicher, High-resolution one-photon and 2-photon spectra of matrix-isolated anthracene. Chemical Physics, 1994. **181**(1-2): p. 185-208.

209. Jin, H.H., et al., Self-healing thermoset using encapsulated epoxy-amine healing chemistry. Polymer, 2012. **53**(2): p. 581-587.

210. Blaiszik, B.J., N.R. Sottos, and S.R. White, Nanocapsules for self-healing materials. Composites Science and Technology, 2008. **68**(3-4): p. 978-986.

211. Zhang, H. and J.L. Yang, Development of self-healing polymers via amine-epoxy chemistry: I. Properties of healing agent carriers and the modelling of a two-part self-healing system. Smart Materials and Structures, 2014. **23**(6).

212. Fifo, O., K. Ryan, and B. Basu, Glass fibre polyester composite with in vivo vascular channel for use in self-healing. Smart Materials and Structures, 2014. **23**(9).

213. Huang, H.L., G. Ye, and Z.H. Shui, Feasibility of self-healing in cementitious materials - By using capsules or a vascular system? Construction and Building Materials, 2014. **63**: p. 108-118.

214. Toohey, K.S., et al., Delivery of Two-Part Self-Healing Chemistry via Microvascular Networks. Advanced Functional Materials, 2009. **19**(9): p. 1399-1405.

APPENDIX A

EFFECTS OF GELATOR 12-HYDROXYSTEARIC ACID (12-HSA) ON IONIC LIQUID BASED PICKERING EMULSIONS

Introduction

Colloidal particles have received increasingly wide attention in a new application: Pickering emulsions. In these emulsions the colloidal particles adhere to the emulsion droplet interfaces, forming an "armor" to protect the droplets against coalescence. Consequently, the most radical aspect of these emulsions is that there is no need for conventional surfactants. Ramsden [1] and later Pickering [2] were the first to report this phenomenon over a century ago, but only recently has interest resurfaced. The absence of surfactant makes these emulsions attractive for cosmetic, food, and pharmaceutical applications [3-5], where toxicity is an issue. Furthermore, functionalization of the colloidal particles can introduce a new level of applicability for emulsions. For instance, Fuller's group employed paramagnetic solid particles to prepare water-decane emulsions whose stability could be tuned and controlled using an external magnetic field [6]. Using Pd, Resasco's group has shown that colloidal particles could be used as catalysts for hydrogenation reactions at the oil/water droplet interface [7]. Such a system significantly simplifies hydrogenation reactions because the products are separated from the reactants within the reactor, eliminating the need for expensive separation equipment [7]. Recently, thermally responsive Pickering emulsions were reported by Tilton's group in which temperature sensitive polymer brush coated nanoparticles were successfully incorporated as emulsion stabilizers [8].

Pickering emulsions are also attractive routes for the synthesis of novel microstructures. Self-assembled hollow spheres with a permeable shell of microparticles are known as "colloidosomes." Colloidosomes have potential application in controlled

delivery and cosmetics, arising from the controllable permeability of the particle shell [9-16]. Velev et al. first reported a technique for the preparation of hollow spheres by the assembly of micron-sized sulfate latex particles on the surface of octanol droplets in water [11]. Many groups have since exploited this process to create solid structures: particles are generally cross-linked at the interface, leaving a stable colloidosome of a few nm to microns in diameter [17]. Raspberry-type formations are solid cores decorated with smaller colloidal particles and can be synthesized by polymerizing the Pickering emulsion droplets covered with particles [17]. Our group has used Pickering emulsions to develop a framework to synthesize organic-inorganic hybrid core-shell microparticles [18,19]. Other structures formed from Pickering emulsion droplets include rod-shaped liquid cylinders [20] and partially coalesced droplets [21]. Pickering emulsion applications continue to proliferate. In this paper we will explore a new avenue that has received attention only very recently: ionic liquid-based Pickering emulsions.

Room temperature ionic liquids (RTIL) are a unique collection of materials that exist in the liquid state at room temperature. This is because, in a typical RTIL, the steric mismatch of a bulky organic cation and a small organic or inorganic anion does not allow lattice packing, which happens in most inorganic salts. The large ion size also damps the coulombic attractions of ion pairs [22]. Ionic liquids, especially RTILs, have attracted much attention as a replacement for traditional organic solvents as they have many unique properties, such as negligible volatility, non-flammability, high thermal and chemical stability, high ionic conductivity, and large electrochemical window [23-25].

In recent years, ionic liquid (IL)-based microemulsions have received more attention. Many surfactants have been demonstrated to effectively stabilize ionic liquid microemulsions [26-29]. In contrast, very few studies have focused on ionic liquid based Pickering emulsions that are stabilized by solid particles. Binks and coworkers prepared a series of ionic liquid emulsions stabilized solely by fumed silica nanoparticles and investigated the emulsion stability and phase inversions [30,31]. Ma and Dai studied 1-butyl-3-methylimidazolium hexafluorophosphate ([BMIM][PF_6])-in-water Pickering emulsions and observed the self-assembled particle morphology at ionic liquid-water interfaces and the partition preferences of the particles [32]. In the work by Walker et al, a unique and new bridging phenomenon has been reported: in polydimethylsiloxane (PDMS)-in-[BMIM][PF_6] Pickering emulsions, solid particles mostly formed bridges among the oil droplets rather than equilibrating at the oil-ionic liquid interface and the aggregated oil droplets promoted oil/ionic liquid phase separation [33].

There has been a growing interest in making semi-solid colloidal particles through hot emulsification followed by cooling to room temperature [34,35]. Ma and Dai reported that [BMIM][PF_6] had good extraction ability for certain types of particles in [BMIM][PF_6]-in-water Pickering emulsions [32]. The motivation of the current study is to perturb these Pickering emulsions by employing a gelator, 12-Hydroxystearic acid (12-HSA), to solidify ionic liquid droplets containing extracted particles. The gelator 12-HSA, mainly produced from castor oil by hydrogenation of the double bond, has been used as a low molecular mass organogeltor (LMOG) [36-39]. LMOG-based gels are prepared by mixing the melted gelator and solution at high temperature and then cooling the solution mixture at gelation point. Most of them are physical gels which are thermally reversible,

because the fiber structure network which immobilizes the solution is formed by non-covalent interactions [38]. Voss et al prepared ionic liquid solid membranes for CO_2 separation application by physical gelation of 1-hexyl-3-methylimidazolium bis-(trifluoromethylsulfonyl) imide [C_6mim][Tf_2N] using a small weight percent of 12-HSA [36]. In this report, we will study how 12-HSA affects [BMIM][PF_6]-in-water and PDMS-in-[BMIM][PF_6] Pickering emulsions. The original objectives were to gel IL by 12-HSA to solidify IL droplets with extracted particles in water and to stabilize the oil-in-IL Pickering emulsion by taking the advantage of the sol-gel transition of 12-HSA.

2. Methodology

2.1 [BMIM][PF_6] gel

The ionic liquid gel with 0.5 wt. % and 1 wt. % 12-HSA(Aldrich) was prepared by heating and mixing 0.005 g and 0.01 g 12-HSA with 1 g [Bmim][PF_6] (≥97%, Aldrich), respectively, in a water bath maintained at 80 ℃. For a good dispersion of 12-HSA, the mixture was agitated by an ultrasonic processor (Sonics VibraCell, 500 W model) once 12-HSA was completely melted, and then cooled at room temperature to form an opaque white soft gel.

2.2 [BMIM][PF_6]-in-water emulsions w/o and w/12-HSA

The [BMIM][PF_6]-in-water Pickering emulsions contained 0.1g [BMIM][PF_6], 1.1 g water (HPLC, Acros Organics) and 0.1 g particle dispersion (fluorescent polystyrene microspheres from Molecular Probes™ ,1 μm diameter, 2% dispersion in distilled water with 2 mM sodium azide). The characteristics of the particles are included

in Table 1. The emulsions were prepared using the same ultrasonic processor in an ice bath at 21% amplitude for 10 pulses at duration of 1 second each pulse. For the system with 12-HSA, the mixture contained 0.1 g prepared 1 wt. % ionic liquid gel and 1.1 g water and 0.1 g particles . The emulsions were dispersed by the ultrasonic processor once the gel became transparent in 80 ℃ water bath and then cooled at room temperature.

2.3 PDMS-in-[BMIM][PF_6] emulsions w/o and w/12-HSA

The PDMS-in-[BMIM][PF_6] Pickering emulsions contained 0.1 g PDMS (Thodorsil Fluid 47 V20, viscosity of 20 cSt at 25 ℃) and 1.1 g [BMIM][PF_6] with 0.002 g dry S-PS particles. The emulsion was prepared using the same ultrasonic processor. For the system with 12-HSA, the mixture consisted of 0.1 g PDMS, 1.1 g prepared 0.5 wt. % and 1 wt. % [BMIM][PF_6] gel and 0.002 g dry S-PS particles. The emulsion was dispersed by the ultrasonic processor in 80 ℃ water bath and cooled at room temperature, unless stated otherwise.

2.4 Confocal Laser Scanning Microscopy (CLSM) and Rheological Characterization

Images were obtained using a Leica SP5 confocal laser scanning microscope under ambient conditions. The fluorescent intensity spectra were obtained via a wavelength scan over the range of 645-744 nm for S-PS particles under excitation at 633 nm, over the range of 550-649 nm for C-PS particles under excitation at 543 nm and over the range of 500-599 nm for A-PS particles under excitation at 488 nm. The spectra for the aqueous phases before and after emulsification were collected under the same laser intensity and at the approximately the same depth within the samples. For each intensity plot, the data was averaged from five runs of the same sample.

The strain sweep test was monitored using a TA Instruments AR-G2 rheometer at 25 ℃. Strain % was ranging from 0.05-200, at a frequency of 1 Hz. There were three types of samples tested: pure [BMIM][PF_6], 0.5 wt. %, and 1 wt. % 12-HSA [BMIM][PF_6] gel. For each type, the final results were calculated by averaging two measurements of fresh samples.

Table 1. Properties of charged fluorescent polystyrene microspheres.

Type	**Surface Dissociable Group**	**Size(μm)**	**Surface Charge Density (C/m^2)**	**Excitation/Emission Wavelengths (nm)**
S-PS	Sulfate	1.0±0.031	-0.029	580/605
C-PS	Carboxylate	1.1±0.035	-0.325	540/560
A-PS	Amine	1.0±0.023	0.152	505/515

3. Results and Discussion

3.1 Ionic Liquid Gels

We first set out to investigate the effect of 12-HSA on pure [BMIM][PF_6]. Experimental evidence indicates that 12-HSA effectively gels a number of oils including Canola oil [37,38], methyl oleate [39], glycerol [39], methanol [40], toluene [40], mineral oil [39,41], and an IL, [C_6MIM][Tf_2N] [36]. In order for effective gelation to occur, the 12-HSA molecules must immobilize the solvent by self-assembling into 3D networks of thin, entangled fibers [42,43]. Zhu and Dordick showed that this process only occurs when the interactions between the gelator molecules and the solvent are minimized [44]. Otherwise, large structures form and macroscopic phase separation occurs [43]. Therefore, only if the IL-gelator interactions were small could 12-HSA successfully gel [BMIM][PF_6].

A super-saturated solution of 1.0 wt. % 12-HSA in [BMIM][PF_6] was mixed at 80°C and allowed to cool. No macroscopic phase separation was observed and the 12-HSA effectively gelled the IL. The top right image of Figure 1 shows that the resulting gel was opaque and did not flow under gravity (vial is upside down). In contrast, we found that at 0.5 wt. % 12-HSA was unable to gel the IL. Due to an insufficient amount of 12-HSA molecules to form a completely gelled network, the mixture was translucent (see the middle image of Figure 1) and flowed under gravity. Clearly, a rheological transition took place between these two concentrations.

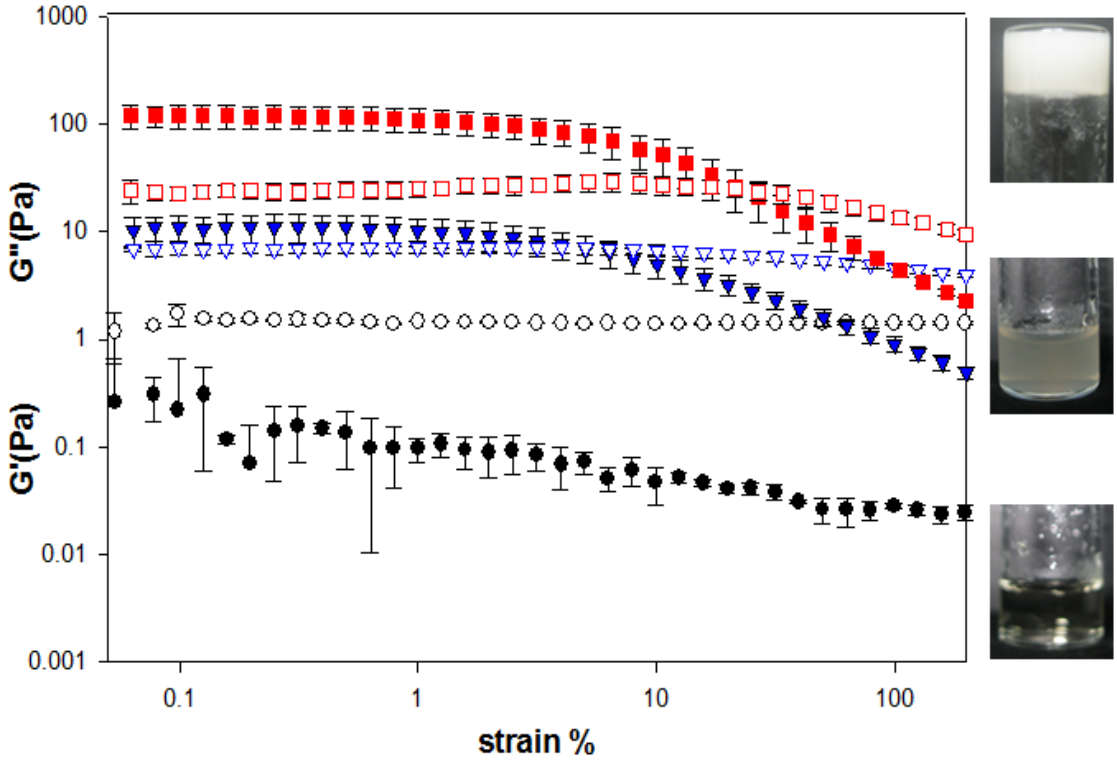

Figure 1. Variation of rheological properties as a function of strain %. The solid symbol is storage modulus G' and the open symbol is loss modulus G". ● pure IL; ▼ 0.5 wt.% gel; ■ 1 wt.% gel. The frequency is 1 Hz.

Therefore, we compared the rheological properties of these two mixtures with the pure IL. Specifically, we measured the storage modulus (G', elastic component) and the loss modulus (G", viscous component) for each sample as a function of strain percentage (a strain-sweep test). Figure 1 shows that the elastic component, G', of the 1.0 wt% mixture was dominant in gel state at low strain %. With increasing strain rate, however, the gel structure was overcome to exhibit more liquid-like behavior (shear-thinning), evidenced by the dominant viscous component. Increased 12-HSA concentration also resulted in higher G' and G". These results confirmed the visual observations that a rheological transition (liquid to gel) indeed took place upon addition of 12-HSA and that complete gelation of [BMIM][PF_6] by 12-HSA only occurred above 0.5 wt%.

Since the Pickering emulsions studied herein included water and PDMS, we briefly investigated how 12-HSA behaved in these two solvents. It was found that 12-HSA effectively gelled the PDMS at 1 wt%. In water, 12-HSA did not gel the solvent, but aggregated, causing a macroscopic phase separation. The structure difference under the microscopy was also apparent. Microscopic images of 12-HSA in the IL, PDMS, and water are displayed in Figure 2, respectively. For reference, the original 12-HSA powder is shown as an inset of Figure 2a. Long and highly entangled fibers were observed in gels formed in both IL and PDMS. The presence of these macroscopic fibers accounted for the cloudy white, non-transparent appearance of the gels. In water, 12-HSA molecules self-assembled into branched structures centered on nuclei, resulting in large clusters. This morphology is a result of isotropic self-assembly and is characteristic of weak or non-existent gelation [44]. As mentioned before, good gelation (formation of fibrous networks) is disrupted by high gelator-solvent interactions. High solvent-gelator interactions (or higher solubility) allow the gelator molecules to move more freely and thus aggregate isotropically rather than form thin fibers [44]. We can conclude, therefore, that PDMS and [BMIM][PF_6] maintained minimal interactions with 12-HSA, whereas water interacted more favorably. H-bonding between water and 12-HSA was likely the main factor behind aggregation, leading to macroscopic phase separation rather than microscopic phase separation [38,44]. However, the fact that the fibers were thicker in IL than in PDMS is evidence that the former interacted more with 12-HSA. It should be noted that even though the fibers were thicker, 1-dimension growth was still dominant, which is the defining feature of gelled structures [44]. Strong interaction between the

charged species of the IL and the hydroxyl groups of the 12-HSA can only be expected, but it was not strong enough to induce significant branching in the fibrous structures.

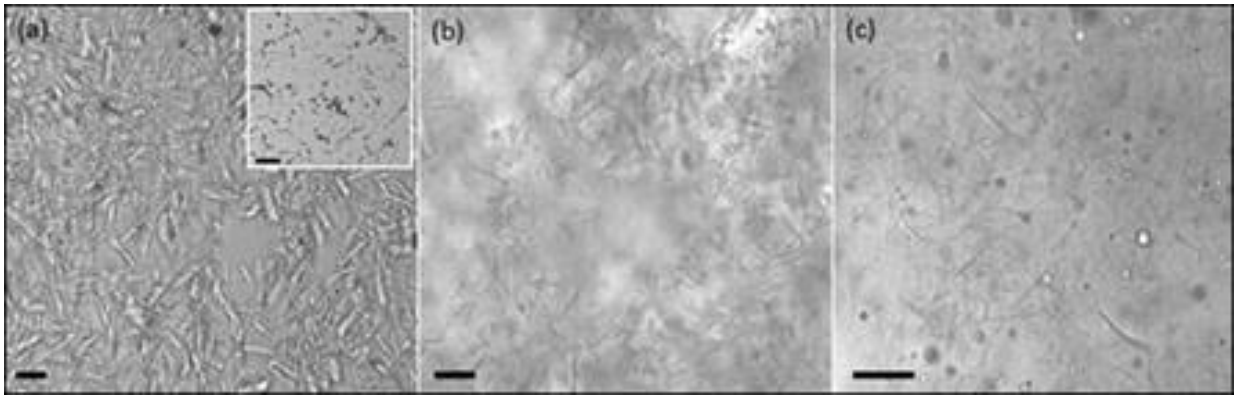

Figure 2. Microscope images of 12-HSA fiber structure in (a) IL, the inset is original morphology the 12-HSA powder, (b) PDMS, and (c) water. The scale bars represent 20 um.

Fiber growth is also affected by the rate of cooling [45]. Typically, slower cooling rates allow for longer fibers [45]. We prepared IL gels at three different cooling rates and measured the fiber lengths using ImageJ ®. Figure 3 shows representative images of these three gels with their respective fiber lengths. At cooling rates of 0.1 ℃/s, fibers of ~50 microns (with large standard deviation) in length were formed. These fibers were significantly shortened and branched at faster cooling rates. Such behavior follows what is called the nucleation-growth-crystallographic mismatch branching (CMB) mechanism [46]. CMB suggests that one-dimensional growth is favored at low cooling rates due to the relatively high energy required to form branches [46]. Gelation of [BMIM][PF_6], therefore, appears to have followed conventional mechanisms.

Gelation of ILs has received increasing interest in the wake of the proliferation of IL-based applications. Many applications require properties unique to ILs, but are unable

to support a liquid phase. For example, ILs offer excellent gas separation qualities and tunability, but are not easily employed in membranes because they can be displaced by the pressure difference. Voss et al showed how gelation overcomes this obstacle without inhibiting the advantageous properties of the IL. Gelled ionic liquids, or ionogels, have numerous other applications. Dye-sensitized solar cells based on ionogels have shown high efficiency and temperature durability [47,48]. Ionogels have also been used to create controlled-release drug devices, where the IL itself has antibacterial qualities [49]. Other applications include catalytic membranes, lithium-ion batteries, fuel cells, sensors, and actuators [50]. Having established that 12-HSA gels the pure IL, we will now investigate how this gelator behaves in the heterogeneous systems: IL-based Pickering emulsions.

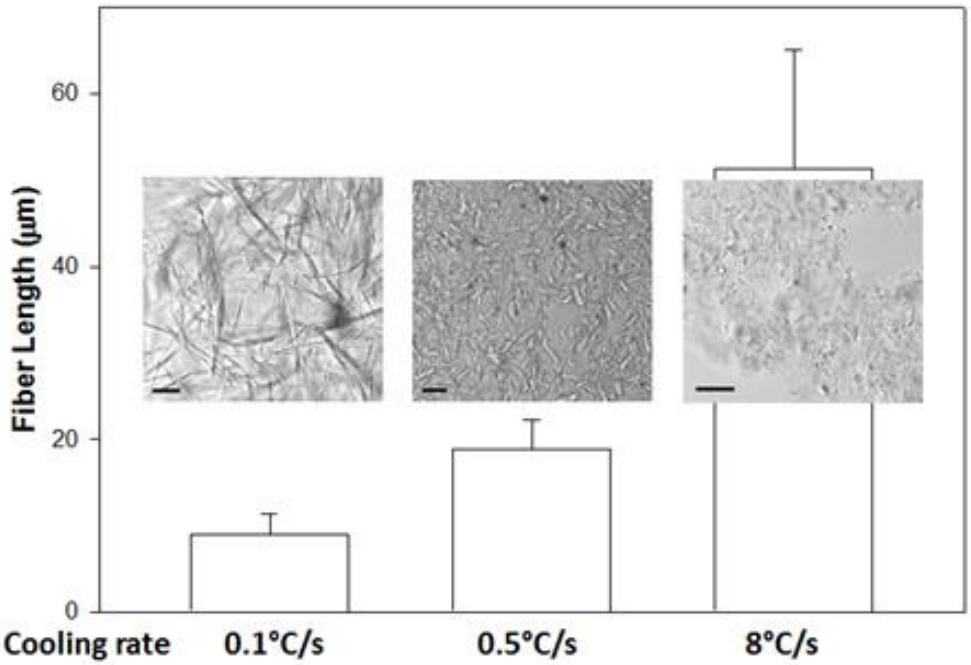

Figure 3. The effect of cooling rate on the self-assembled 12-HSA fiber lengths with representative images. The scale bars represent 20 um.

3.2 Effect of 12-HSA on [BMIM][PF_6]-in-Water Pickering Emulsions

For reference, we formulated three gelator-free IL-in-water Pickering emulsions. The representative confocal images in Figure 4(a-c) show that the particles generally self-assembled at the interfaces of the IL droplets. This is in agreement with general consensus of Pickering emulsion morphology [51,52]. In the S-PS and C-PS systems, droplets were generally only partially covered. For the A-PS system, both fully- and partially-covered droplets were observed. Cross-sectional images of the Pickering emulsion droplets are included in Figure 4(d-f). Interestingly, many S-PS and C-PS particles were observed in IL phase, which indicates that they must have been transported across the IL/water interface since the particles were originally dispersed in water phase. No A-PS particles were transported to IL phase. This phenomenon is unusual because the energy required for a particle to desorb from the interface is on the order of 1000-10^6 kT due to capillary effects [53]. Particle transport across the liquid-liquid interface appears to be unique to IL systems and has been discussed in recent literature, usually with emphasis on extraction applications [32,54-58]. The observation that only particles with acidic functional groups were extracted into the IL phase suggests that proton exchange between the surface groups and the [PF_6] may have lead to more favorable particle-IL interactions. Layering of IL ions at the particle surface may also play a role in this phenomenon [54]. Admittedly, the mechanism behind this extraction is not yet fully understood. However, it promises useful applications in oil sand/tar processing and oil

spill beach cleanup: recent work has shown that imidazolium ILs can efficiently extract sand particles from oil at ambient conditions [54-57].

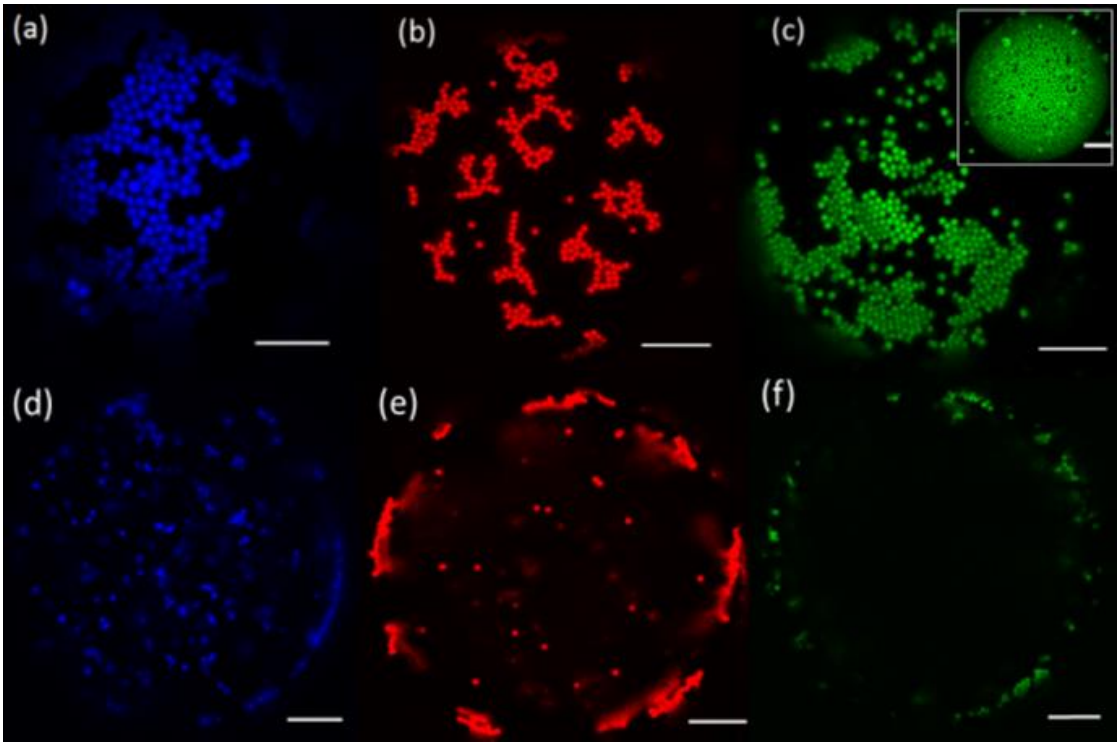

Figure 4. (a-c) Overlays of depth-series confocal microscope images of IL droplets in water in the presence of particles; (d-f) Confocal microscope images of IL droplet cross sections in the presence of particles. (a,d) S-PS particles, (b,e) C-PS particles, (c,f) A-PS particles. The scale bars represent 10 μm.

Based on the results of the previous experiments, we expected that 12-HSA would exclusively gel the IL droplets, immobilizing the S-PS and C-PS particles inside. Melted IL-gelator mixture was dispersed in water in the presence of particles via sonication at 80°C. An emulsion resulted and was allowed to cool at room temperature. Interestingly, it was observed that the 12-HSA did not gel the IL droplets as a whole, but the fibers aggregated exclusively at the droplet interfaces (see Figure 5a-c). Also, the number particles (S-PS and C-PS) in the individual droplets was significantly less than in

these systems. An explanation on how the addition 12-HSA facilitated these effects is due.

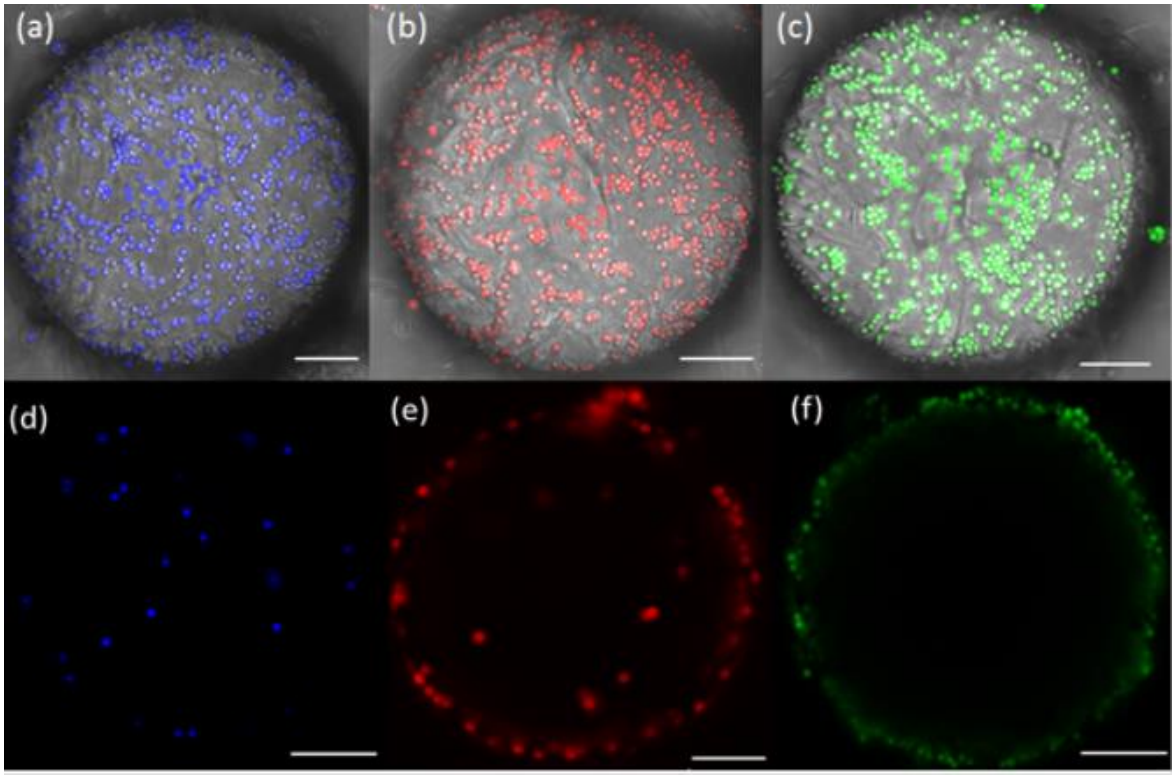

Figure 5. (a-c) Overlays of depth-series confocal and differential interference contrast (DIC) images of IL droplets in water in the presence of particles w/12-HSA; (d-f) Confocal microscope images of IL droplet cross sections in the presence of particles. (a,d) S-PS particles, (b,e) C-PS particles, (c,f) A-PS particles. The scale bars represent 10 μm.

A separate experiment was performed to study the behavior of 12-HSA at the IL/water interface. One sample containing equal amounts of water and prepared 1 wt. % 12-HSA IL gel was kept at 80 ℃ in hot water bath for five minutes and then cooled to room temperature. During heating, some liquid 12-HSA was noticeably transported out of the IL phase and into the bulk water phase (partially favoring the top of the water phase because of buoyancy). After cooling, white solids were observed at the water/IL interface and partially in the bulk water phase. The IL phase was no longer a gel. This

phase partitioning was expected since we had already observed that 12-HSA was more "soluble" in (or has higher interactions with) water than in the IL. This relatively higher "solubility", however, prevented the 12-HSA from forming any gel in the bulk water phase, as was discussed in the previous section. Consequently, the 12-HSA could only form gel fibers in close contact with the ILat the interface. Capillary forces likely aided their adhesion to the IL/water interface. In this way the 12-HSA exclusively gelled IL/water interfaces, rather than either of the liquid phases. Thus, the results from this experiment explain why fibers were only seen at droplet surfaces as in Figure 5a-c. Besides, in another separate experiment, 12-HSA fibers alone were sufficient enough to stabilize the emulsion in the absence of polystyrene particles. It is likely that this phenomenon was related to the observed decreased number of particles in the IL droplets. We quantified particle absorption by measuring the particle occupancy for the S-PS particles (μm^2) in individual droplets of systems without 12-HSA and with 12-HSA as a function of cooling rate. Figure 6 suggests that these measurements verified the microscopic observations. It was observed that at slower cooling rates, the fibers grew longer at the droplet interfaces; correspondingly, the fibers were significantly shortened at fast cooling rates. However, compared to the fiber length in bulk IL, these fibers were relatively small, only reaching approximately 20 microns in length at a cooling rate of 0.1 ℃/s. We hypothesized that was due to the restrictive geometric nature of the droplet template. Particle transport was affected by the fiber length: longer fibers trapped more particles on interfaces, possibly because of the interpenetration and entanglement of long fibers which made the gel shell thicker at the interface, hindering the particle motion into the droplets. Oppositely, the shorter fiber matrix did not hinder particle transport across

the interface. Therefore, quite a few particles were observed inside of the droplets. In this way, 12-HSA perturbed the original Pickering emulsion morphology and the particle transport process could be controlled by manipulating the degree of interfacial gelation via cooling rate.

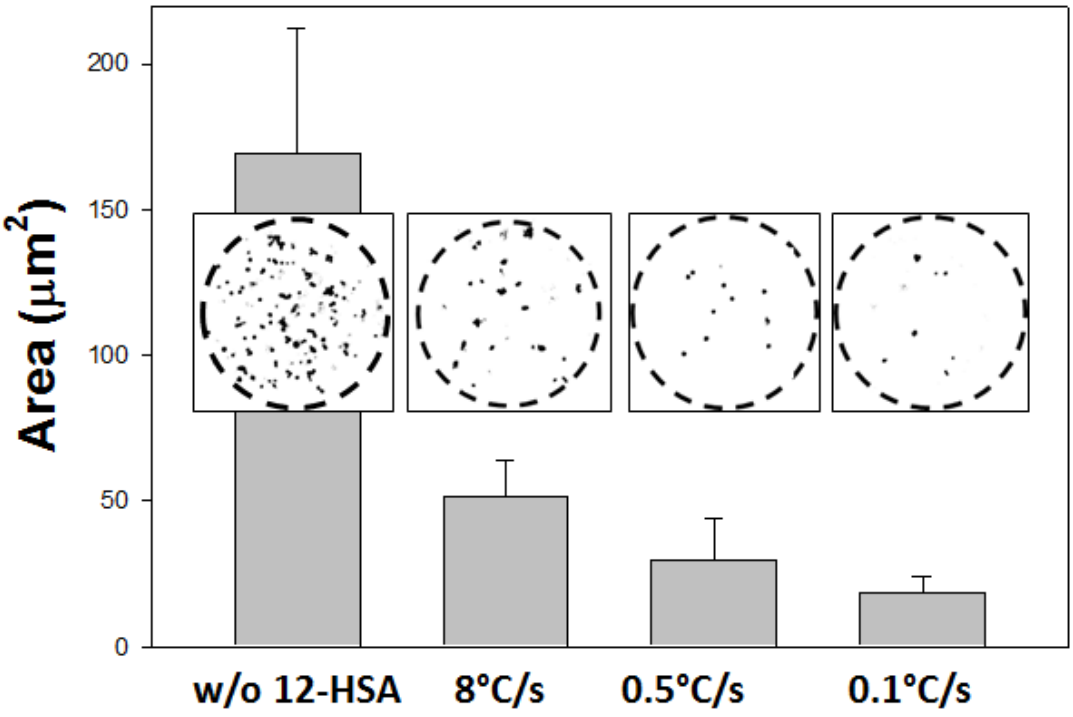

Figure 6. Occupancy of particles in the individual emulsion droplets without 12-HSA as well as with 12-HSA at varying cooling rates. The insets are sample images from ImageJ analyses and the particles are approximately 1 micron in diameter.

Also of interest is the number of particles absorbed from the water phase. To better compare the number of particles in the bulk phase before and after emulsification for each system, the concentration of particles in water phase was characterized by quantifying the fluorescence intensity over the emission wavelength range of the corresponding fluorescent particles in the bulk. The top panels in Figure 7 show the

fluorescence intensity spectra of the water phase before and after emulsification without 12-HSA. For S-PS and C-PS systems, the fluorescence intensity after emulsification fell nearly to zero level, suggesting that almost all the particles were transferred out of the water phase either to the droplets or to the interfaces. For the A-PS system, the fluorescence intensity dropped only slightly, indicating that many particles remained in water phase after emulsification. Intensity measurement of the systems with 12-HSA are shown in the bottom panel of Figure 7. While the S-PS and C-PS systems showed negligible change upon addition of 12-HSA, the A-PS system showed a significant decrease in bulk particle concentration. Since IL-absorbed A-PS particles were not observed in the confocal images, we can assume that these particles were adsorbed at the droplet interfaces. The presence of fibers at the droplet interfaces provided more surface area with which the particles could interact and this may have lead to higher interfacial adsorption. Furthermore, the S-PS and C-PS fluorescence intensities exhibited little change, indicating that the previously absorbed particles migrated to only to the interface, rather than to the bulk. Therefore, greater degrees of interfacial particle adsorption were observed in the presence of 12-HSA.

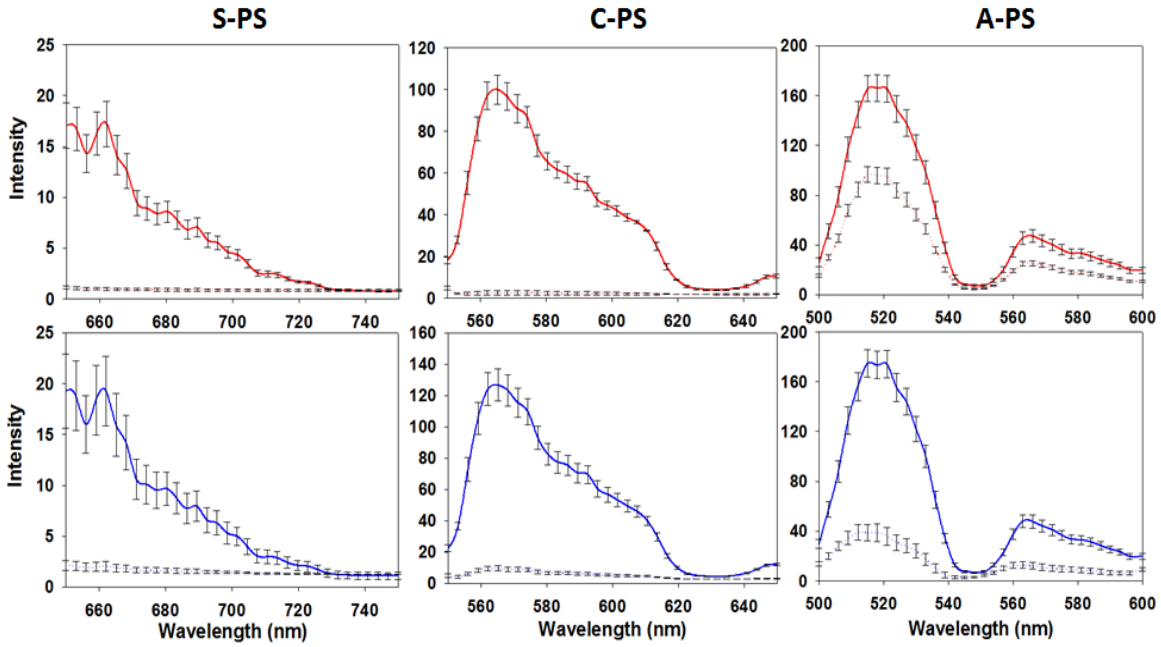

Figure 7. Fluorescence intensity spectra of the emulsions (top: no 12-HSA; bottom: with 12-HSA) before (solid line) aqueous phase and after (dashed line) emulsification.

Some brief discussion of the effect of particle surface chemistry on their behavior in these systems is warranted. As discussed in our previous work [32], particles in these experiments had various surface dissociable groups, so the phase preference was likely a function of particle properties including hydrophobicity, sign and density of surface charge, and specific surface chemistry. First, hydrophobicity was considered, but since both hydrophobic (S-PS) and hydrophilic (C-PS) particles were absorbed by the IL, it was ruled out as a dominant factor. The fact that both of these particles were absorbed also rules out the possibility that charge density played a major role. These results support the conclusions made in ref [32]. Next, the sign of surface charge may have affected partition preference. Positive charge (in the dissociated state) is one feature unique to the A-PS particles, which were not absorbed. There is some experimental evidence indicating that the large cations can inhibit the solvation of positively charged

species [59-61]. Another feature unique to the A-PS particles was the fact that it had basic surface functionality, while the S-PS and C-PS particles had acidic groups. The latter two particles could undergo dissociation in either the water or IL phase since the PF_6 anion could accept acidic protons. On the other hand, A-PS particles could undergo dissociation only in the water phase since the IL, being aprotic, had no free protons. Therefore, while we can rule out surface charge density and hydrophobicity as important factors in this process, surface chemistry and charge sign likely played a defining role.

3.3 Effect of 12-HSA on PDMS-in-[BMIM][PF_6] Pickering Emulsions

In contrast to the IL-in-water emulsion, oil-in-IL Pickering emulsions exhibit a completely different morphology. It was observed by Walker et al that in PDMS-in-[BMIM][PF_6] Pickering emulsions, the particles exclusively bridged the oil droplets, creating flocculated droplet structures of varying size and morphology [33]. A representative microscopy image of a Pickering emulsion of oil-in-IL in the presence of S-PS particles is shown in Figure 8(a). The possible explanation of bridge formation is that the particles, which were dispersed in IL phase, were trapped between oil droplets as they approached each other during mixing. This bridge formation inhibited droplet-droplet coalescence, but these aggregated droplets distressed the overall emulsion stability by promoting creaming due to buoyancy [33].

Emulsion stability is usually a desirable quality, so we hypothesized that gelling the IL to immobilize oil droplets would stabilize these emulsions. As demonstrated in the previous experiments, 12-HSA was able to gel both the IL and PDMS phases. A measured amount of 12-HSA was added to see how it would affect the emulsions. At low

(0.5 wt. %) 12-HSA concentration, bridged droplets were not observed, suggesting that the bridging effect was limited in the presence of a gelator. This may have been due to partial gelation of the IL, which would greatly slow the motion of droplets during mixing, decreasing the chance that the droplets collided with each other. Very few particles were attached to the droplet interfaces. Even without bridging, droplets were still aggregated together to form clusters of varying sizes. The corresponding image is displayed in Figure 8(b). At high (1 wt. %) 12-HSA concentration, droplet clusters were larger and packed more tightly. Particles were observed to be trapped at the droplet interfaces. Representative images are included in Figure 8(c). Additionally, it should be noted that droplets with and without fibers on interface were both observed under microscopy.

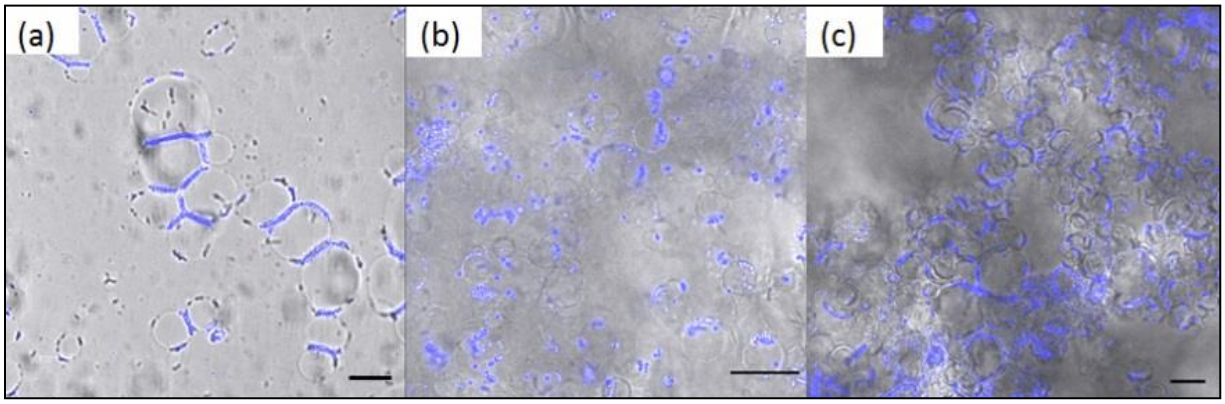

Figure 8. Overlays of confocal and differential interference contrast (DIC) images of oil-in-IL Pickering emulsions in the presence of S-PS particles.(a)w/o 12-HSA; (b) 0.5 wt.% 12-HSA; (c) 1 wt.% 12-HSA. The scale bars represent 20 μm.

Droplet cluster formation may be explained by two mechanisms. One is that bridged flocculation occurred as 12-HSA fibers were bound directly to multiple droplet interfaces. 12-HSA on the interfaces or around the droplets would form fibrils to interconnect the droplets acting as a bridge. A similar behavior has been observed with

long proteins which may bridge droplets in gelled food emulsions [62,63]. In these studies, evidence of this bridging mechanism lies in the fact that, droplet flocculation increased with protein concentration [62]. Such behavior appears analogous to the dependence of flocculation on 12-HSA concentration in the present study (see Figure 6). Another important cluster-forming mechanisms is depletion flocculation. Effectively, this means that before complete gelation, the shell immediately surrounding the droplets was free of 12-HSA fibrils, creating a concentration gradient. The osmotic pressure difference because of concentration gradient would then induce an attractive force between the droplets. Flocculated droplet would be subsequently gelled upon cooling. Recent theoretical and experimental work has shown that droplet packing is dependent on both attractive and repulsive forces included in the depletion mechanism [64-66]. This packing, and not the forces themselves, determine the rheology of depletion-induced emulsion gels [64]. The depletion force depends on a concentration gradient, which gives rise to effective osmotic pressure to push the droplets together. This may explain why droplet clusters were more tightly packed in the emulsion at 1 wt.% 12-HSA.

Despite cluster formation, we found that higher concentrations of 12-HSA increased the stability of the bridging emulsions significantly. Figure 9 compares the stability of oil-in-IL Pickering emulsion with and without 12-HSA. Due to the low density and large volume, the bridged oil droplets in the system without 12-HSA quickly rose to the top and finally separated from IL phase to form a cream layer. At high 12-HSA concentration, oil droplets were immobilized in IL gel matrix, therefore, no separation occurred. Low 12-HSA concentration could not immobilize oil droplets completely because the storage modulus was not big enough to withstand the buoyant

force. These observations confirmed our hypothesis that gelation would stabilize these unique emulsions.

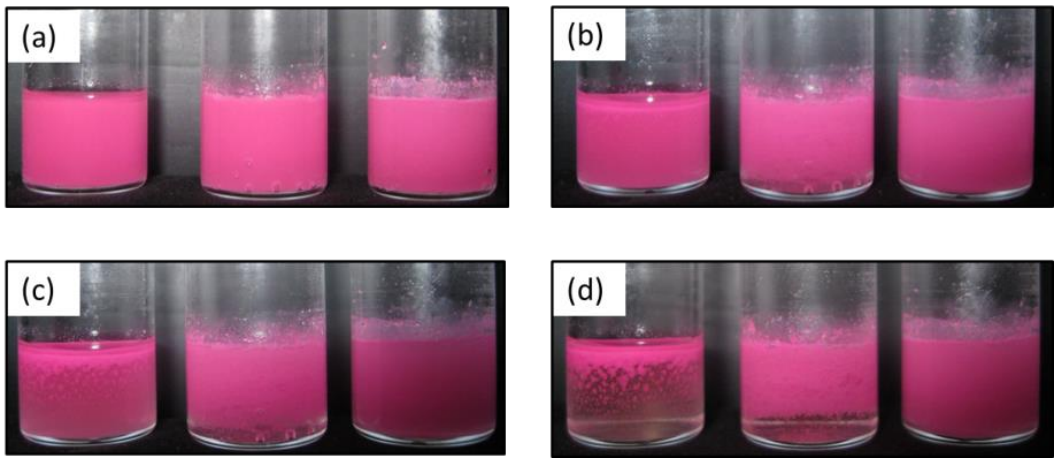

Figure 9. Emulsion stability as a function of time. The vials from left to right contain no 12-HSA, 0.5 wt. % 12-HSA, 1 wt. % 12-HSA. They all have the same amount of S-PS particles. (a) t = 0; (b) t = 0.5 h; (c) t=6 h; (d) t= 24 h.

The characteristics of bridged droplets and droplet clusters can produce a number of benefits in high internal phase emulsions (HIPEs) manufacturing for which their internal phase has a high volume fraction (up to 74% by volume or above) [67]. HIPEs have many potential applications in different fields, such as encapsulation [68] and synthesis of porous materials [67,69] for tissue scaffolds [70], sensors [71], and hydrogen storage [72]. The thermoreversible gelation opens new possibilities for the control of emulsion properties and performance in the preparation of advanced materials with respect to the improvement of chemical release, manipulation of emulsion rheology, and stability by temperature control.

4. Conclusion

In this work, we have examined the perturbation effects of HSA on IL-based Pickering emulsions. The 12-HSA gelled pure [BMIM][PF_6] and PDMS effectively by the formation of entangled networks of thin fibers but not the water phase since proper gelation can only occur in the presence of a less polar solvent. In IL-in-water Pickering emulsions, the 12-HSA gelled the IL-water interfaces rather than the entire IL droplets since they partitioned into the water phase. In addition, we found that the morphology of interfacial gelation could be engineered by manipulating cooling rate and consequently provided a new way of controlling the solid particle transport into the dispersed phase. The 12-HSA effectively stabilized oil-in-IL Pickering emulsions by increasing the elastic modulus of the bulk phase and consequently overcoming the buoyancy force of the bridged droplets. These results indicate that phenomena unique to IL based Pickering emulsions can be tuned by the addition of an organogelator.

5. Acknowledgements

We thank the National Science Foundation for financial support and the NASA/ASU Graduate Fellowship to D. Frost.

6. References

[1] W. Ramsden, Proc. R. Soc. London. 91 (1903) 940.

[2] S.U. Pickering, Emulsions, J. Chem. Soc. Trans. 91 (1907) 2001.

[3] E. Dickinson, Use of nanoparticles and microparticles in the formation and stabilization of food emulsions, Trends Food Sci. Technol. 24 (2012) 4-12.

[4] E. Dickinson, Food emulsions and foams: Stabilization by particles, Curr. Opin. Colloid Interface Sci. 15 (2010) 40-49.

[5] S. Simovic, N. Ghouchi-Eskandar, C. Prestidge, Pickering emulsions for dermal delivery, J. Drug Delivery Sci. Technol. 21 (2011) 123-133.

[6] S. Melle, M. Lask, G.G. Fuller, Pickering emulsions with controllable stability, Langmuir. 21 (2005) 2158-2162.

[7] S. Crossley, J. Faria, M. Shen, D.E. Resasco, Solid nanoparticles that catalyze biofuel upgrade reactions at the water/oil interface, Science. 327 (2010) 68-72.

[8] T. Saigal, H.C. Dong, K. Matyjaszewski, R.D. Tilton, Langmuir. 26 (2010) 15200-15209.

[9] A.D. Dinsmore, M.F. Hsu, M.G. Nikolaides, M. Marquez, A.R. Bausch, D.A. Weitz, Colloidosomes: Selectively Permeable Capsules Composed of Colloidal Particles, Science. 298 (2002) pp. 1006-1009.

[10] B.P. Binks, Applications of Emulsions, in: Anonymous Modern Aspects of Emulsion Science, Royal Chemistry Society, Cambridge, 1998, pp. Chapter 12.

[11] O. Velev, K. Furusawa, K. Nagayama, Assembly of latex particles by using emulsion droplets as templates .1. Microstructured hollow spheres, Langmuir. 12 (1996) 2374-2384.

[12] O.D. Velev, K. Nagayama, Assembly of Latex Particles by Using Emulsion Droplets. 3. Reverse (Water in Oil) System, Langmuir. 13 (1997) 1856-1859.

[13] M.F. Hsu, M.G. Nikolaides, A.D. Dinsmore, A.R. Bausch, V.D. Gordon, X. Chen, J.W. Hutchinson, D.A. Weitz, M. Marquez, Self-assembled Shells Composed of Colloidal Particles: Fabrication and Characterization, Langmuir. 21 (2005) 2963-2970.

[14] O. Cayre, P. Noble, V. Paunov, Fabrication of novel colloidosome microcapsules with gelled aqueous cores, J. Mater. Chem. 14 (2004) 3351-3355.

[15] P.F. Noble, O.J. Cayre, R.G. Alargova, O.D. Velev, V.N. Paunov, Fabrication of "hairy" colloidosomes with shells of polymeric microrods, J. Am. Chem. Soc. 126 (2004) 8092-8093.

[16] A.B. Subramaniam, M. Abkarian, H.A. Stone, Controlled assembly of jammed colloidal shells on fluid droplets, Nature materials. 4 (2005) 553-556.

[17] Z. Niu, J. He, T.P. Russell, Q. Wang, Synthesis of Nano/Microstructures at Fluid Interfaces, Angew. Chem. Int. Ed. 49 (2010) 10052-10066.

[18] H. Ma, M. Luo, S. Sanyal, K. Rege, L. Dai, The One-Step Pickering Emulsion Polymerization Route for Synthesizing Organic-Inorganic Nanocomposite Particles, Materials. 3 (2010) 1186-1202.

[19] S. Sanyal, H. Huang, K. Rege, L.L. Dai, Thermo-Responsive Core-Shell Composite Nanoparticles Synthesized via One-Step Pickering Emulsion Polymerization for Controlled Drug Delivery, Journal of Nanomedicine and Nanotechnology. 2 (2011) 126.

[20] S.A.F. Bon, S.D. Mookhoek, P.J. Colver, H.R. Fischer, S. van der Zwaag, Route to stable non-spherical emulsion droplets, Eur. Poly. 43 (2007) 4839-4842.

[21] A.B. Pawar, M. Caggioni, R. Ergun, R.W. Hartel, P.T. Spicer, Arrested coalescence in Pickering emulsions, Soft Matter. 7 (2011) 7710-7716.

[22] R. Hayes, G.G. Warr, R. Atkin, At the interface: solvation and designing ionic liquids, Phys. Chem. Chem. Phys. 12 (2010) 1709-1723.

[23] T. Welton, Room-Temperature Ionic Liquids. Solvents for Synthesis and Catalysis, Chem. Rev. 99 (1999) 2071-2084.

[24] P. Bonhote, A. Dias, N. Papageorgiou, K. Kalyanasundaram, M. Gratzel, Hydrophobic, Highly Conductive Ambient-Temperature Molten Salts, Inorg. Chem. 35 (1996) 1168-1178.

[25] M.J. Earle, Esperanca, J. M. S. S., M.A. Gilea, J.N.C. Lopes, L.P.N. Rebelo, J.W. Magee, K.R. Seddon, J.A. Widegren, The distillation and volatility of ionic liquids, Nature. 439 (2006) 831-834.

[26] Z. Qiu, J. Texter, Ionic liquids in microemulsions, Curr. Opin. Colloid Interface Sci. 13 (2008) 252.

[27] J. Eastoe, S. Gold, S.E. Rogers, A. Paul, T. Welton, R.K. Heenan, I. Grillo, Ionic liquid-in-oil microemulsions, J. Am. Chem. Soc. 127 (2005) 7302-7303.

[28] Y.N. Gao, S.B. Han, B.X. Han, G.Z. Li, D. Shen, Z.H. Li, J.M. Du, W.G. Hou, G.Y. Zhang, Langmuir. 21 (2005) 5681.

[29] Y. Gao, J. Zhang, H.Y. Xu, X.Y. Zhao, L.Q. Zheng, X.W. Li, L. Yu, Chemphyschem. 7 (2006) 1554.

[30] B.P. Binks, A.K.F. Dyab, P.D.I. Fletcher, Contact angles in relation to emulsions stabilised solely by silica nanoparticles including systems containing room temperature ionic liquids, Phys. Chem. Chem. Phys. 9 (2007) 6391-6397.

[31] B.P. Binks, P.D.I. Fletcher, A.K.F. Dyab, Novel emulsions of ionic liquids stabilised solely by silica nanoparticles, Chem. Commun. (2003) 2540-2541.

[32] H. Ma, L.L. Dai, Particle Self-Assembly in Ionic Liquid-in-Water Pickering Emulsions, Langmuir. 27 (2011) 508-512.

[33] E.M. Walker, D.S. Frost, L.L. Dai, Particle self-assembly in oil-in-ionic liquid Pickering emulsions, J. Colloid Interface Sci. 363 (2011) 307.

[34] P. Kirilov, L. Lukyanova, S. Franceschi-Messant, V. Perier, E. Perez, I. Rico-Lattes, A new type of colloidal dispersions based on nanoparticles of gelled oil, Colloids Surf. , A. 328 (2008) 1-7.

[35] J.J. Richards, K.M. Weigandt, D.C. Pozzo, Aqueous dispersions of colloidal poly(3-hexylthiophene) gel particles with high internal porosity, J. Colloid Interface Sci. 364 (2011) 341-350.

[36] B. Voss, J. Bara, D. Gin, R. Noble, Physically Gelled Ionic Liquids: Solid Membrane Materials with Liquidlike CO2 Gas Transport, Chem. Mater. 21 (2009) 3027-3029.

[37] M. Rogers, A. Wright, A. Marangoni, Engineering the oil binding capacity and crystallinity of self-assembled fibrillar networks of 12-hydroxystearic acid in edible oils, Soft Matter. 4 (2008) 1483-1490.

[38] M.A. Rogers, A.J. Wright, A.G. Marangoni, Nanostructuring fiber morphology and solvent inclusions in 12-hydroxystearic acid / canola oil organogels, Curr. Opin. Colloid Interface Sci. 14 (2009) 33-42.

[39] M.A. Rogers, A.G. Marangoni, Solvent-modulated nucleation and crystallization kinetics of 12-hydroxystearic acid: a nonisothermal approach, Langmuir. 25 (2009) 8556-8566.

[40] J.P. Eloundou, E. Girard-Reydet, J. Gérard, J. Pascault, Calorimetric and rheological studies of 12-hydroxystearic acid / digycidyl ether of bisphenol A blends, Polymer Bulletin. 53 (2005) 367-375.

[41] M.A. Rogers, J.H.J. Kim, Rheological assessment of the sol–gel transition for self-assembling low molecular weight gelators, Food Res. Int. 44 (2011) 1447-1451.

[42] P. Terech, I. Furman, R.G. Weiss, Structures of Organogels Based upon Cholesteryl 4-(2-Anthryloxy)butanoate, a Highly Efficient Luminescing Gelator: Neutron and X-ray Small-Angle Scattering Investigations, J. Phys. Chem. 99 (1995) 9558-9566.

[43] P. Terech, R.G. Weiss, Introduction, in: P. Terech, R.G. Weiss (Eds.), Molecular Gels: Materials with Self-ASsembled Fibrillar Networks, Springer, Dordrecht, 2006, pp. 978.

[44] G. Zhu, J.S. Dordick, Solvent Effect on Organogel Formation by Low Molecular Weight Molecules, Chem. Mater. 18 (2006) 5988-5995.

[45] R. Lam, L. Quaroni, T. Pedersen, M.A. Rogers, A molecular insight into the nature of crystallographic mismatches in self-assembled fibrillar networks under non-isothermal crystallization conditions, Soft Matter. 6 (2010) 404-408.

[46] R. Wang, X. Liu, J. Xiong, J. Li, Real-Time Observation of Fiber Network Formation in Molecular Organogel:â€‰ Supersaturation-Dependent Microstructure and Its Related Rheological Property, J Phys Chem B. 110 (2006) 7275-7280.

[47] W. Kubo, S. Kambe, S. Nakade, T. Kitamura, K. Hanabusa, Y. Wada, S. Yanagida, Photocurrent-determining processes in quasi-solid-state dye-sensitized solar cells using ionic gel electrolytes, J Phys Chem B. 107 (2003) 4374-4381.

[48] N. Mohmeyer, D. Kuang, P. Wang, H. Schmidt, S.M. Zakeeruddin, M. Gratzel, An efficient organogelator for ionic liquids to prepare stable quasi-solid-state dye-sensitized solar cells, J. Mater. Chem. 16 (2006) 2978-2983.

[49] B.G. Trewyn, C.M. Whitman, V.S.-. Lin, Morphological Control of Room-Temperature Ionic Liquid Templated Mesoporous Silica Nanoparticles for Controlled Release of Antibacterial Agents, Nano Lett. 4 (2004) 2139-2143.

[50] J. Le Bideau, L. Viau, A. Vioux, Ionogels, ionic liquid based hybrid materials, Chem. Soc. Rev. 4 (2011) 97-925.

[51] S. Tarimala, L.L. Dai, Structure of Microparticles in Solid-Stabilized Emulsions, Langmuir. 20 (2004) 3492-3494.

[52] L.L. Dai, S. Tarimala, C. Wu, S. Guttula, J. Wu, The Structure and Dynamics of Microparticles at Pickering Emulsion Interfaces, Scanning. 30 (2008) 87.

[53] B.P. Binks, S.O. Lumsdon, Influence of Particle Wettability on the Type and Stability of Surfactant-Free Emulsions, Langmuir. 16 (2000) 8622-8631.

[54] C.G. Hogshead, E. Manias, P. Williams, A. Lupinsky, P. Painter, Studies of Bitumen-Silica and Oil-Silica Interactions in Ionic Liquids, Energy Fuels. 25 (2011) 293-299.

[55] P. Painter, P. Williams, A. Lupinsky, Recovery of Bitumen from Utah Tar Sands Using Ionic Liquids, Energy Fuels. 24 (2010) 5081-5088.

[56] P. Painter, P. Williams, E. Mannebach, Recovery of Bitumen from Oil or Tar Sands Using Ionic Liquids, Energy Fuels. 24 (2010) 1094-1098.

[57] P. Williams, A. Lupinsky, P. Painter, Recovery of Bitumen from Low-Grade Oil Sands Using Ionic Liquids, Energy Fuels. 24 (2010) 2172-2173.

[58] G. Wei, Z. Yang, C. Lee, H. Yang, C.R.C. Wang, Aqueousâ^'Organic Phase Transfer of Gold Nanoparticles and Gold Nanorods Using an Ionic Liquid, J. Am. Chem. Soc. 126 (2004) 5036-5037.

[59] Y. Nusai, H. Koizumi, M. Tachibana, K. Tani, N. Kiba, The rolesof 1-alkyl 1-3 methylimidazolium-based ionic liquids as mobile phase additives in semi-micro high-performace liquid chromatography for separation of aromatic amines, Anal. Chem. : Indian J. 10 (2011) 365-373.

[60] J. Wang, Y. Pei, Y. Zhao, Z. Hu, Recovery of amino acids by imidazolium based ionic liquids from aqueous media, Green Chem. 7 (2005) 196-202.

[61] F. Andre, P. Hapiot, C. Lagrost, Dimerization of ion radicals in ionic liquids. An example of favourable "Coulombic" solvation, Phys. Chem. Chem. Phys. 12 (2010) 7506-7512.

[62] E. Dickinson, C. Ritzoulis, M.J.W. Povey, Stability of Emulsions Containing Both Sodium Caseinate and Tween 20, J. Colloid Interface Sci. 212 (1999) 466-473.

[63] E. Dickinson, F.O. Flint, J.A. Hunt, Bridging flocculation in binary protein stabilized emulsions, Food Hydrocoll. 3 (1989) 389-397.

[64] A. Meller, T. Gisler, D.A. Weitz, J. Stavans, Viscoelasticity of Depletion-Induced Gels in Emulsion-Polymer Systems, Langmuir. 15 (1999) 1918-1922.

[65] C. Xiao, J. Wylie, Depletion forces and packing models, Phys. Lett. A. 357 (2006) 245-248.

[66] C. Bechinger, D. Rudhardt, P. Leiderer, R. Roth, S. Dietrich, Understanding depletion forces beyond entropy, Phys. Rev. Lett. 83 (1999) 3960-3963.

[67] C. Neil R., High internal phase emulsion templating as a route to well-defined porous polymers, Polymer. 46 (2005) 1439-1449.

[68] M.T. Gokmen, W. Van Camp, P.J. Colver, S.A.F. Bon, F.E. Du Prez, Fabrication of Porous Clickable • Polymer Beads and Rods through Generation of High Internal Phase Emulsion (HIPE) Droplets in a Simple Microfluidic Device, Macromolecules. 42 (2009) 9289-9294.

[68] G.J. Lye, D.C. Stuckey, Structure and stability of colloidal liquid aphrons, Colloids Surf. , A. 131 (1998) 119-136.

[70] M. Bokhari, R. Carnachan, S. Przyborski, N. Cameron, Emulsion-templated porous polymers as scaffolds for three dimensional cell culture: effect of synthesis parameters on scaffold formation and homogeneity, J. Mater. Chem. 17 (2007) 4088-4094.

[71] C. Zhao, E. Danish, N. Cameron, R. Kataky, Emulsion-templated porous materials (PolyHIPEs) for selective ion and molecular recognition and transport: applications in electrochemical sensing, J. Mater. Chem. 17 (2007) 2446-2453.

[72] F. Su, C.L. Bray, B. Tan, A.I. Cooper, Rapid and Reversible Hydrogen Storage in Clathrate Hydrates Using Emulsion-Templated Polymers, Adv Mater. 20 (2008) 2663-2666.